Point of Care, Clinical and Forensic Assays via DNA-Bead Aggregation

Qian Liu

Lanzhou, Gansu, China

B.S., Nankai University, 2009

A Dissertation presented to the Graduate Faculty of the

University of Virginia in Candidacy for the Degree of

Doctor of Philosophy

Department of Chemistry

University of Virginia

August, 2015

Abstract

The work presented here focuses on the development of point of care medical device for CD4+ T-cells enumeration, and a filter paper based DNA quantitation assay, both assays are based on the DNA-silica beads aggregation, the "*pinwheel effect*"

Chapter 1 introduces the concept of microfluidics, and the materials used to fabricate microfluidics devices, devices for blood analysis, the status quo of the Point of Care Testing (POCT), and a brief overview of nanoparticles synthesis and their properties. Chapter 2 explores the pinwheel assay and its application on CD4+ T cells enumeration in tube, chapter 3 details the integrated CD4+ T-cell counting chip with 3 domains: extraction, metering and DNA-bead aggregation. Chapter 4 and 5 discuss the filter paper based DNA quantitation system, this simple and cost-effective assay was developed to quickly quantitate DNA and guide forensic tests like Short Tandem Repeat (STR). Silica coated magnetic nanoparticles were synthesized to study the mechanism of pinwheel effect, and the results have shown that the sensitivity of the 'pinwheel assay' depends on the particle size. Finally the chapter 6 outlines future directions.

Acknowledgements

I would first like to thank Dr. James P. Landers for the opportunity to join his lab. I'm truly grateful for his instructions on conducting research, scientific writing, and academic presentation. During my time in the Landers group, I was fortunate to work with many talented scientists on various research projects, I thank everyone in the Landers group, including undergrad researchers, for making the lab a delightful and inspiring place to be. My gratitude extends to the members of my committee, Dr. B Jill, Venton, Dr. David S. Cafiso, Dr. James N. Demas, and Dr. Lindsay A.L. Bazydlo, for their assistance during my graduate career. Additionally, I would like to thank Dr. Robert Burnett and Dr. Richard J. Sundberg for their generous help when I was a teaching assistant.

I would like to dedicate this thesis to those precious to me, for their unflinching encouragement and support during the course of this work. My dearest parents, Lichun Cui and Weidong Liu, have always been extremely supportive to me, despite we being separated by the Pacific Ocean, their unconditional love keeps me move forward. Last but not least, I would like to thank Dr Jiajun Mei, I cannot express how grateful I am for his companionship and support, he has been my family and best friend, it is an honor to share my success with him.

Chapter 1. Introduction

1.1 Overview

This chapter aims to introduce some fundamental concepts and up to date developments that relate to the work presented in the following chapters, that includes the essential of microfluidics, with the focus on polymer microfluidic devices; The concept of Point of Care Testing (POCT); Research topics on blood cells, and a brief overview of nanotechnology, with emphasis on magnetic nanoparticles synthesis.

1.2 Microfluidics

Microfluidics involves the movement of small amounts of fluids. The technology, first developed by the semiconductor industry and later expanded by the micro-electromechanical systems (MEMS) field, is used for miniaturization and integration of different fluidic components, in the same way that a microelectronic circuit is an entire computer on a chip [1].

Microfluidic devices have gain popularity as an analytical tool for conducting biological, chemical and medical analysis. The microfluidics devices are commonly referred to as miniaturized total analysis systems (mTASs), or lab-on-a-chip (LOC) technologies. These devices have *sample-in-answer-out* capability and have the potential to impact a wide variety of applications, including diseases diagnosis [2-5], genetic analysis [6-8] and forensic DNA profiling [9-10]. Traditionally, devices are fabricated out of silicon and glass, however, a recent trend in the field is a shift towards polymeric material such as poly(dimethylsiloxane) (PDMS), polyethylene-terephthalate (PE), poly(methylmethacrylate) (PMMA), as well as paper devices, given the trend towards developing more cost effective, disposable devices that can be used in

resource-limited areas. Furthermore, these materials provide simplified fabrication and the possibility of incorporating densely integrated micro function domains into designs

1.2.1 Polydimethylsiloxane (PDMS) Micro-devices

Polydimethylsiloxane (PDMS) is a mineral-organic polymer of the siloxane family, where the word siloxane is derived from silicon, oxygen and alkane. The molecular formula of PDMS is $CH_3[Si(CH_3)_2O]nSi(CH_3)_3$, n being the number of repetitions of the monomer. Depending on

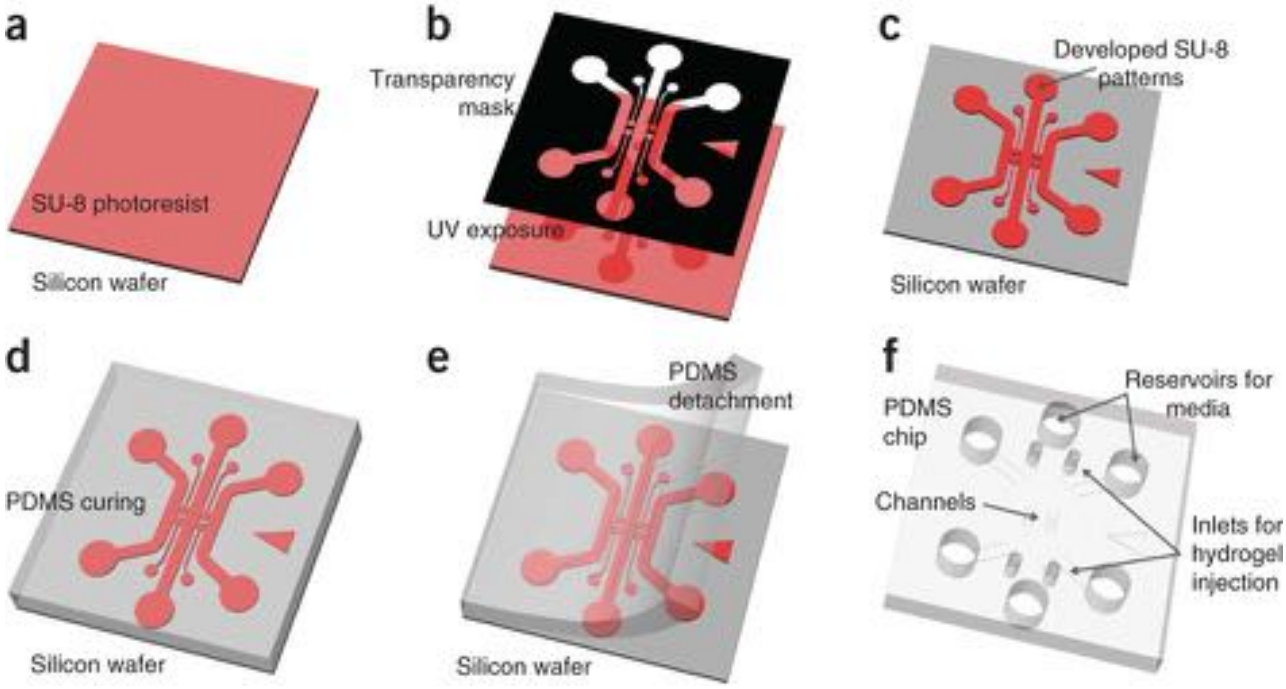

Figure 1-1 *(a–f) Schematics of the photolithography (a–c) and soft lithography (d–f) procedures. (a) SU-8 is spin-coated and prebaked on a bare wafer. (b) With a transparency photomask (black), UV light is exposed on the SU-8. (c) Exposed SU-8 is then baked after exposure and developed to define channel patterns. (d) PDMS mixed solution is poured on the wafer and cured. (e) Cured PDMS is then peeled from the wafer. (f) The device is trimmed, punched and autoclaved ready for assembly. Taken from [15]*

the size of the string of monomer, the non-cross-linked PDMS may be almost liquid (small n) or semi-solid (large n), the smaller value of n, the closer the compound resembles a liquid state.

Several characteristics of PDMS made it popular in fabricating bioanalysis related microfluidic devices. These include transparency in the UV-visible regions, chemical inertness, biocompatibility, easy fabrication (it can easily form and retain microstructures when cured and removed from a mold), low polarity, low electrical conductivity, and elasticity [11-12]. Hundreds of PDMS microfluidics devices have been developed for various applications since its debut in 2002 [13-14].

The procedure for manufacturing a PDMS mold with nm resolution is often achieved by the soft lithography technique using photoresist, such as SU8, the procedure is outlined in **Figure 1-1** [15-16]. Soft lithography has provided a low-expertise route toward micro/nanofabrication and has played an important role in microfluidics, ranging from simple channel fabrication to the creation of micro patterns on a surface or within a microfluidic channel. Other materials such as Shrinky-Dinks has been applied to fabricate the mold [17] for creating rounded channels. This method is cost effective and easier to fabricate, however the mold resolution is not comparable with the SU8 mold, as the shrinking extent can't be accurately controlled. Laser ablation has also been used to pattern PDMS, with a resolution of 1 μm [18], laser ablation does not only save time (~10 minutes compared to hours of soft lithography), but also protects the features from any dimensional changes resulting from curing of PDMS. Depending on the application and resolution requirement, different patterning method should be considered accordingly.

After the mold is fabricated, PDMS monomers are mixed with a cross-linking agent, poured into the microstructured mold, and heated to obtain a replica of the elastomer mold. The curing time and the curing temperature is reversely correlated, i.e., the curing takes less time at

higher temperature, and vice versa. For example, the Sylgard® 184 Silicone elastomer takes 2 hours to cure at 75 ˚C, it only takes 15 minutes to cure at 150 ˚C [19].

Cured PDMS in its natural state displays hydrophobic properties due to the thermodynamically favorable position of its functional groups [20-21]. Utilization of oxygen or

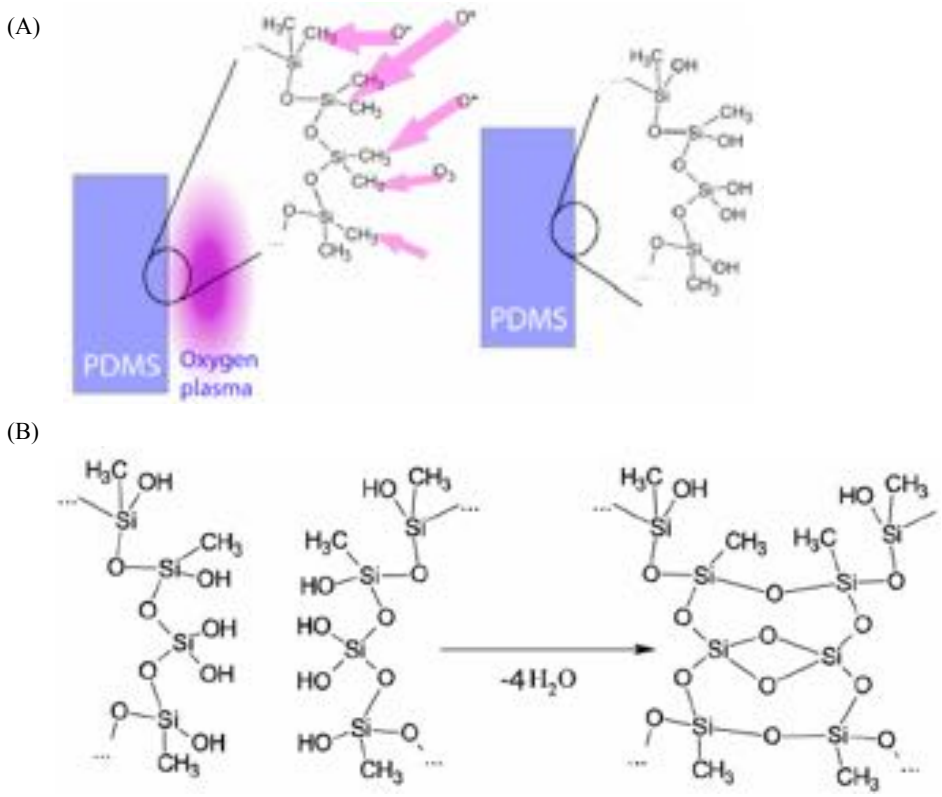

Figure 1-2. *PDMS bonding chemistry (A) Demonstration of how the oxygen plasma treatment change the PDMS surface to hydrophilic (B) Formation of the covalent bond after PDMS is treated by oxygen or air plasma. http://www.elveflow.com/microfluidic-tutorials/soft-lithography-reviews-and-tutorials/how-to-choose-your-soft-lithography-instruments/pdms-soft-lithography-plasma-cleaner/. accessed on July 15, 2015.*

nitrogen plasma changes the surface chemistry of PDMS and oxidizes the functional groups, producing silanol groups on the surface[12]. This process also makes the surface resistant to the adsorption of hydrophobic and negatively-charged molecules [22] (**Figure 1-2A)**. The oxidation is temporary, and over the course of 24 hours the PDMS relaxes back into its thermodynamically

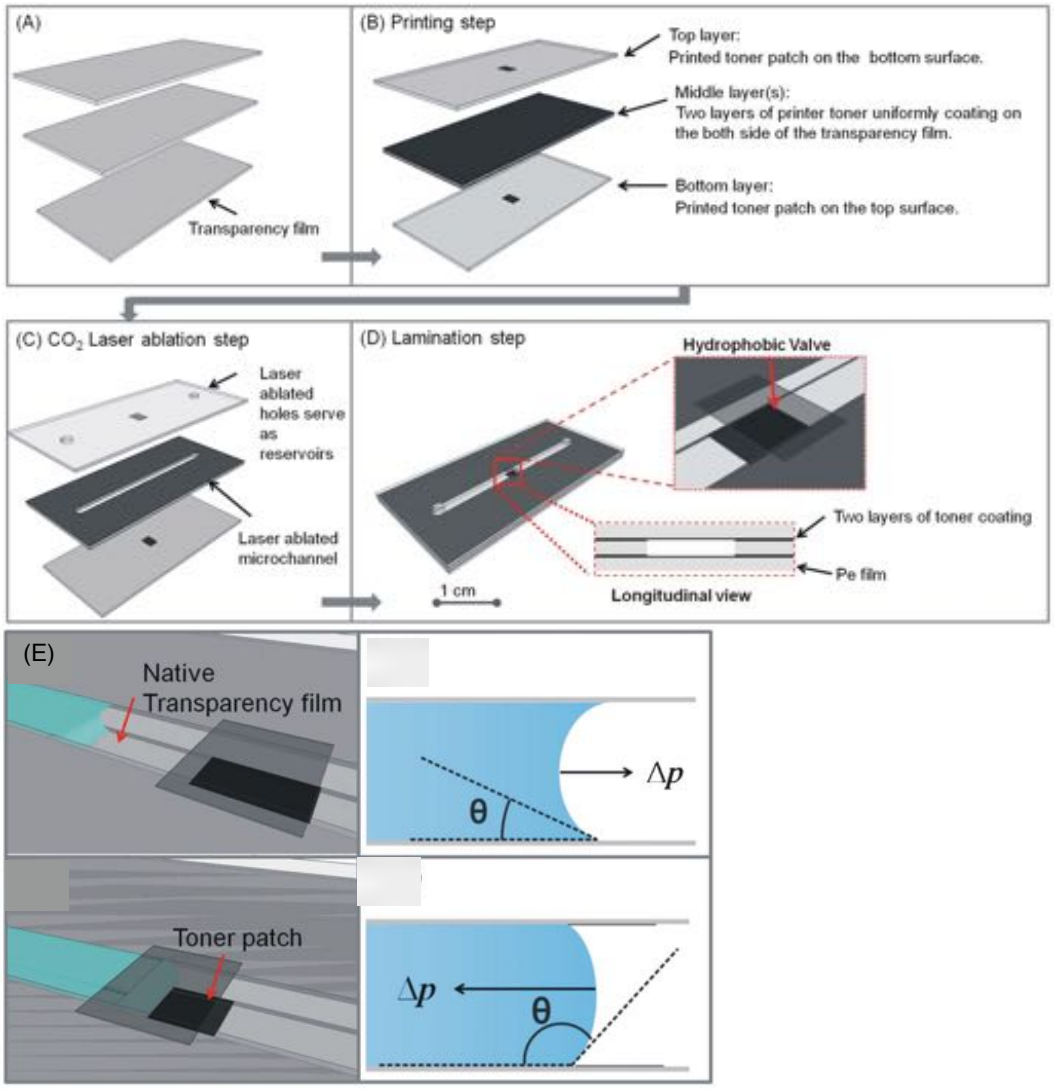

Figure 1-3. *Steps involved in the fabrication of a PeT microdevice with hydrophobic toner-based valves, and the valving mechanism. (A) Three layers of transparency film, (B) patterning toner onto the both sides of the middle layer and hydrophobic patches on the top and bottom layers, (C) microfeatures cut by laser cutter in to middle layers and, (D) alignment of all layers for lamination. (E) liquid priming the channel with either a hydrophilic ceiling surface (top) or hydrophobic ceiling surface (bottom). Taken from [28]*

favored hydrophobic state, with the optimal hydrophilicity lasting only around 20 minutes [14]. The plasma treated PDMS can covalently bond with an oxidized glass or PDMS surface by the

creation of a Si-O-Si bond (**Figure 1-2B)**.

Whether the surface of PDMS is oxidized in plasma or not, it does not allow the water, nitromethane, dimethyl sulfoxide, ethylene glycol, perfluorotributylamine, perfluorodecalin, acetonitrile, and propylene carbonate to infiltrate. Thus, it is possible to use PDMS with these fluids without micro-structure deformation. However, the PDMS deforms and swells in the presence of diisopropylamine, triethylamine, pentane, and xylenes, and also to a lesser extent in the presence of acetone, propanol and pyridine [23]. The highly swelling solvents could be applied to extract contaminant from PDMS, for example, triethylamine and ethyl acetate were used to extract low molecular weight oligomers from cured PDMS, in order to prolong the hydrophilic property of plasma treated PDMS surface [24].

1.2.2. Poly(ethylene terephthalate) (PE) Devices

Poly(ethylene terephthalate) transparency film and printer toner has also been used to fabricated microfluidic devices [25]. The device architecture can be either defined by printed toner or simply by laser ablation followed by lamination, using the toner as the adhesive between layers. PeT devices have been successfully applied on DNA extraction, polymeric chain reaction (PCR), electrophoresis, and generating micro-droplets [26-27]. Recently, our lab developed a hydrophobic valve by depositing a toner patch on the polyester [28]. Since toner is hydrophobic, it creates a surface tension and stops the fluid when it meets the toner along a hydrophilic channel. The burst pressure is defined by dimensions of the valve, the hydrophobicity of the toner, and the fractional area of the toner. This breakthrough fills in the gaps in fluidic control on

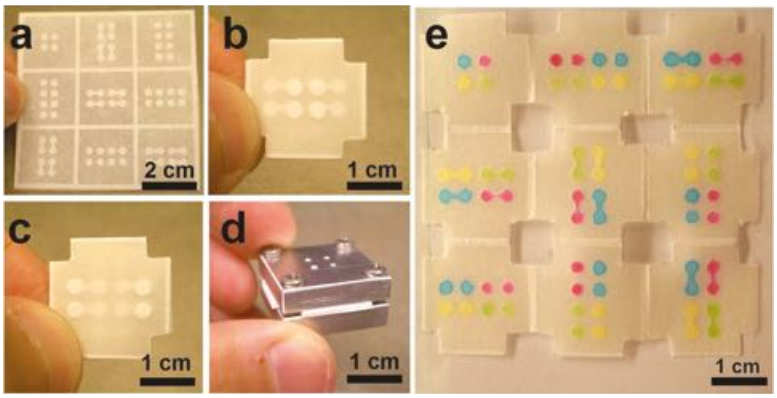

***Figure 1-4**. Design of a 3D origami device for glucose test. (a) Photolithographically patterned chromatography paper (100 µm thick) (b) Top layer of the folded paper revealing four inlet reservoirs in the center of the device. The four flanking circular features are present within the 3-D structure of the device but are visible due to the transparency of the paper. (c) Bottom layer of the folded paper. (d) The aluminum housing used to support the 3-D paper microfluidic system. The four holes in the top of the housing are used for injecting solutions. (e) An unfolded, nine-layer paper microfluidic device after injecting four 1.0 mM, aqueous, colored solutions through the four injection ports in the aluminum clamp. The colored solutions passed through their designated channels and reservoirs without mixing. Taken from [35]*

the PeT device, and empowers multiple step reactions on the PeT device. **Figure 1-3** shows the valve fabrication process and the valving mechanism. PeT centrifugal devices were later developed and applied on DNA quantitation and protein analysis [29-30].

1.2.3 Microfluidic Paper-Based Analytical Devices (µPADs)

Paper devices are very attractive for use in developing countries because they are widely available, easy to fabricate, and cost effective. Moreover, due to capillary action, liquid can move on paper without the need of an active pump or external source [31], making paper devices portable. Channels, reservoirs, and valves can be defined in paper devices by printing wax [32],

inkjet etching and printing of sol−gel [41], and flexographic printing [42]. When high resolution is required, photoresist can be used to pattern paper devices; the photolithographically patterned channels can be as small as 200 μm in width and 30 μm in height (the height of the channel is defined by the thickness of the paper) [33]. 3D paper devices have been fabricated by stacking patterned paper and tapes layer by layer [34], or simply by origami methods [35]. **Figure 1-4** shows an origami 3D device designed for glucose testing.

Many paper devices allow for naked eye detection, and provide a straightforward yes/no answer. Quantitative analysis can be achieved by colorimetric[36], electrochemical[37], chemiluminescent[38], electrochemiluminescent[39], and electrical conductivity[40] measurements.

Lateral flow or dipstick tests such as the pregnancy test kit and glucose meter are well known, and lateral flow immunoassays are widely used for protein detection or DNA-based biomarker detection for disease diagnosis and staging [43-44]. Other applications of existing paper devices include food and beverage contamination detection[45], as well as environmental monitoring [46].

1.3 Blood Cells on Microfluidic Systems

Blood carries rich information about our body, with blood components including red blood cells (RBCs), white blood cells (WBCs), and platelets. Different cells have different functions in the body, for example, platelets help blood clot, and a normal platelet count ranges from 150,000 to 450,000 platelets per microliter of blood. Having more than 450,000 platelets is a condition called thrombocytosis, which is a marker for diseases like leukemia or anemia [47];

having less than 150,000 platelets is defined as thrombocytopenia [48], the patient may suffer from unstoppable bleeding. WBCs maintain the body's immune function, and isolation of WBCs is essential for many hematological analysis and clinical diagnostic tests for monitoring disease progression. Chapter 2 will have more detailed discussion about WBCs. RBCs transport oxygen and carbon dioxide through the body. Hematocrit tests the volume fraction of RBCs in the blood, which is normally 45% for men and 40% for women, a low test result indicates anemia, while a high test result, called polycythemia, could be attributed to chronic smoking, or dehydration [49].

There are also rare cells with significant clinical importance in the blood, such as circulating tumor cells (CTCs). CTCs derive from clones in the primary tumor, and they could be used as a marker for cancer diagnosis, genotyping, and prognosis, as well as provide insights in cancer metastasis [50]. CTCs are very rare in peripheral blood (0.3 – 100 cells mL−1 blood), thus it is challenging to separate them effectively.

The conventional laboratory methods to process blood are time consuming, labor intensive, and are not optimal for processing small volume blood samples. Over the last decade, we have seen many novel integrated and functional microfluidic devices designed for the separation and sorting of blood cells. Various principles could be utilized to separate and sort blood cells, some common methods include physical properties like size and deformability, immunoaffinity, magnetophoresis, acoustophoresis and electrical methods.

Antibody-based microfluidic cell sorting has been proven useful in isolating WBCs[51] and CTCs [52]. Antibody-dependent methods use specific antibodies to identify target cells, in combination with magnetic (magnetophoresis), chemiluminescent, or fluorescence markers, cells can be isolated and analyzed. This method is robust and widely applicable as long as the

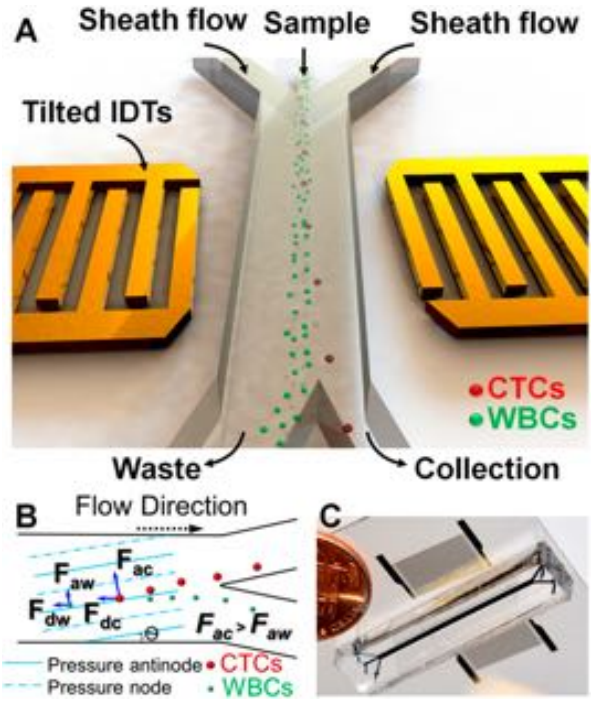

Figure 1-5*. Schematic illustration and image of the taSSAW device for cancer cell separation. (A) Illustration of taSSAW-based cell separation. (B) Schematic of the working mechanism behind taSSAW-based cell separation. The direction of the pressure nodes and pressure antinodes were established at an angle of inclination (θ) to the fluid flow direction inside a microfluidic channel. Larger CTCs experience a larger acoustic radiation force (Fac) than WBCs (Faw). As a result, CTCs have a larger vertical displacement (normal to the flow direction) than WBCs. Fdc and Fdw are the drag force experienced by CTCs. and WBCs, respectively. (C) An actual image of the taSSAW cell separation device. Taken from [54].*

antibody is known. The limitation of this strategy to isolate CTCs is that the CTCs can have highly dynamic antibody expression that depends on the patients.

Acoustophoresis is a contact-free, non-invasive, and label-free method that focuses particles within the microchannels. Under ultrasound fields, particles will be trapped in the acoustic node or the anti-node, the acoustic force experienced by the particles depends on particle size, density and compressibility [53]. Acoustophoresis has been successfully applied to isolate CTCs for cancer diagnostics. As shown in **Figure 1-5**, the authors applied tilted-angle standing surface acoustic waves to successfully separate low concentrations (~100 cells/mL) of a

variety of cancer cells from cell culture lines from WBCs, with a recovery rate better than 83% [54].

Physical filtration is a straightforward method that filters cells by their density, size, shape, or deformability. Many sieving devices are developed to separate RBCs and WBCs due to their size differences [55]. A successful implementation of such devices relies on a precise control of filter geometries. Cell clogging and fouling of filter structures are the major challenge in these devices.

Electrical actuations and sensing are typically sensitive, rapid, convenient and robust. Moreover, electrical methods can be easily integrated with other detection modules. Such compatibility and integrality of electrical methods allow multi-module strategies that can improve throughput, performance and functionality of the micro-device. Electroosmotic flow (EOF) for manipulation of WBCs, isoelectricity (IE) for high throughput B-cell separation and characterization, and dielectrophoresis (DEP) for various cells separation have been achieved on chip [56]. Cells, like all particles, experience electrical polarization when they are subjected to nonuniform electric fields, the induced polarization depends on factors related to cellular physiologic conditions, and DEP separates cells based their different response to the electric fields. For example, malaria-infected erythrocytes have different electrical properties compared to normal RBCs owing to changes in their ionic content and they can be separated by DEP from normal RBCs. Elevated temperature due to Joule heating and the chemicals produced by electrolysis are the major concerns for electrical isolation of blood cells.

1.4 Point of Care Testing (POCT)

Due to the complexity of laboratory tests, the majority of tests were performed in a central lab in the past; however, with the development of microfluidics and information technologies, testing has transitioned from the laboratory to the patient's bedside, the pharmacy, the physician's office, and other non-laboratory sites, referred to as Point of Care Testing, or POCT. Point-of-care testing, as shown in **Figure 1-6**, is defined as "testing at or near the site of patient care whenever the medical care is needed."[57]. The key objective of POCT is to produce a result more quickly, which allows for immediate clinical management decisions to be made. Convenience to patients and care providers mainly derives from the fact that the diagnostic process is completed "in the same clinical encounter" and clients or patients do not have to come back for testing or travel long distances to appropriate facilities.

POCT ranges among three levels of complexity, from simple procedures (i.e. glucose testing and the HCG pregnancy strip test), to moderately complex procedures (i.e. provider performed microscopy procedures), to highly complex procedures (i.e.influenza testing). POCT instruments can be categorized in three ways: handheld, portable, and transportable. Portable indicates a device that can be easily carried, usually with a built-in handle, and transportable indicates that the equipment can be carried on a cart.

An example of a successful POCT device came from the company Theranos™ [58]. Theranos™ has developed novel approaches for laboratory diagnostic tests using a few drops of blood obtained via a finger stick, which is 1/1,000 the size of a typical blood draw. Walgreens retail pharmacy chain has recently enabled Theranos™ to make their services both accessible

and credible for consumers; there are 253 tests available, with the cost ranging from $1.63 per test for hematocrit (HCT) to $117.96 per test for Hepatitis C Virus Genotype [59]. The testing

Figure 1-6. *Illustration of Point of Care Testing (POCT).* **http://edusanjalbiochemist.blogspot.com/2013/09/poct-point-of-care-testing-introduction.html.** *Accessed June 15 2015.*

results are sent wirelessly from the reader to a secure database, where patients and physicians are able to access the results..

The disadvantages of POCT include: concerns about inaccuracy, imprecision, and performance, the operator-dependent nature of the testing, quality management/assurance issues and responsibilities are not defined, a narrower measuring range for some analytes, and difficulty in integrating test results with hospital information systems(HIS) or laboratory information system (LIS), i.e., lack of connectivity. Despite these drawbacks, the main advantage of POCT is convenience for patients and clinicians. By providing the patients with convenient solutions, they can be treated more effectively, for example, a recent study has shown that, after the introduction of a point-of-care device for CD4+ T cells counting in Mozambique, the total loss to follow-up before initiation of the treatment dropped from 64% to 33%, and the enrolled patients for treatment increased from 12% to 22% [60]. Other advantages include the ability to test various types of samples (capillary, saliva, urine), small sample volume for a large array of tests, self-contained and user-friendly instruments, reduced turnaround time of diagnostic testing, and rapid data availability.

1.5 Magnetic Nanoparticles

All the following chapters in this dissertation use silica coated magnetic particles as the matrices for the “Pinwheel Assay”, this section focuses on the magnetic nanoparticles synthesis and its magnetic properties.

Magnetic nanoparticles (MNPs) are well-established nanomaterials that offer controlled size (usually under 100 nm, although there are examples of NPs several hundreds of nanometers

in size), and the ability to be manipulated by an external magnetic field. Magnetic nanoparticles are usually composed of magnetic elements (iron (Fe), nickel (Ni), cobalt (Co), the corresponding oxides such as maghemite (γ-Fe_2O_3), magnetite (Fe_3O_4), chromium dioxide (CrO_2)) and spinel-type ferromagnets ($MgFe_2O_4$,$MnFe_2O_4$, and $CoFe_2O_4$, as well as alloys, like FePt, FePd, CoPt, MnPt, Gd-based nanoparticles) [62-73]. Here we will focus on the the iron and iron oxide magnetic nanoparticles.

1.5.1. Synthesis of Magnetic Nanoparticles

There are various reviews on synthesizing magnetic nanoparticles for a wide range of applications. According to La Mer theory [61], the key to success in the synthesis of uniform crystallization lies in the control over the kinetics of all steps of crystallization, beginning with nucleation and growth, and ending with coarsening and agglomeration, among which the nucleation step is the most critical. In order to control the size distribution, different stages should be separated, i.e., nucleation should be finished before growth begins, and coarsening should be avoided during growth. Other important factors include: temperature, reagent concentration, types of precursors used, and the mechanism of the reaction.

1.5.1.1 Co-precipitation

Co-precipitation is the most common and convenient way to synthesize MNPs from metal salts [62], and a large number of MNPs can be synthesized simultaneously. Usually the Fe(II)/Fe(III) ratio is kept as 0.5 in an alkaline solution, and this yields superparamagnetic iron oxide nanoparticles (SPIONs) below 20 nm. The overall reaction is written in equation (1).

$$Fe^{2+} + 2Fe^{3+} + 8OH^{-} \rightarrow Fe_3O_4 + 4H_2O \qquad (1)$$

Because the precipitation occurs instantly upon mixing with alkaline solution due to a change in the solubility, it is very difficult to control the course of crystallization, co-precipitation method generally have very limited control over the size distribution of the particles, and often requires a size screening process to get relatively uniform sized particles.

Zhao *et al* have shown that the homogeneous pH value in the solution plays a critical role in size distribution, and this could be controlled by the dropping rate of aqueous ammonia. Cubic shaped Fe_3O_4 MNPs with small size distribution (5-20 nm) and an average size of 11.4 nm were synthesized and used as a drug carrier, with the molar ratio of Fe^{3+} and Fe^{2+} set at 3: 2 [63]. Yu *et al* synthesized cellulose@Fe_2O_3 nanoparticles using NaOH–thiourea–urea aqueous solution, using cellulose as a template to promote nanoparticles growth [64]. Xie and coworkers co-precipitated Fe^{2+} and Fe^{3+} in the presence of a polymer, to prevent overgrowth and aggregation [66]. Suh *et al* recently reported a novel MNPs with various shape (disk, sphere, triangular etc). Polymeric spheres were first synthesized using stop-flow lithography, then co-precipitation of Fe^{2+} and Fe^{3+} was carried out in between the carboxy groups from the polymer [67].

1.5.1.2 Thermal Decomposition

Thermal decomposition involves the decomposition of inorganic iron precursors such as $FeCup_3$, ferrictriacetylacetonate ($Fe(acac)_3$), and $Fe(CO)_5$, in the presence of fatty acids or amines as the stabilizing surfactants, mixed in an organic medium at a high temperature

(>200˚C) [68-70]. Thermal decomposition is by far the most reliable method for size- and shape-controllable synthesis of MNPs. The magnetic nanocrystals synthesized by these methods are usually hydrophobic, while there are many ligand-exchange processes capable of rendering them hydrophilic, the resulting MNPs usually have a low magnetization [71-73]. The main control over the synthesis lies in the ratios of the starting reagents, namely the organometallic compounds, surfactants, solvent, as well as the reaction temperature and time of reaction [74-75].

Hyeon *et al* demonstrated that the decomposition of $Fe(CO)_5$ followed by oxidation leads to high quality maghemite nanoparticles [71]. Sun and co-workers succeeded in the synthesis of monodispersed magnetite nanoparticles using $Fe(acac)_3$ as a starting material, in a solution of phenyl ether with alcohol, oleic acid, and oleylamine [72]. Gao and coworkers prepared water soluble MNPs by employing the highly polar organic solvents such as 2-pyrrolidone, which serves as a reaction media and a capping agent that renders the magnetite nanocrystals water-soluble and the colloidal solution stable [75]. Other research groups have followed similar synthetic routes employing solvents such as ethylene glycol (EG), diethylene glycol (DEG), triethlylene glycol (TEG), tetraethylene glycol (TTEG), 2-acetyl pyridine, p-anisaldehyde, ethylene carbonate, and carboxylic acids.

1.5.1.3 Solvothermal Reduction (or Hydrothermal Synthesis)

Recently, a solvothermal reduction method was developed by Li's group to synthesize monodispersed magnetic particles with excellent water solubility [77-83]. Compared to thermal decomposition, solvothermal methods have very good shape control over the resulting particles. It is also worth mentioning that solvothermal reduction often results in MNPs > 100 nm while

other techniques like thermal decomposition, co-precipitation and microemulsion often lead to MNPs<30 nm.

In a typical procedure, the magnetite particles are synthesized at 200 ºC by reduction of $FeCl_3$ with ethylene glycol (EG), sodium acetate as the base source, and trisodium citrate as an

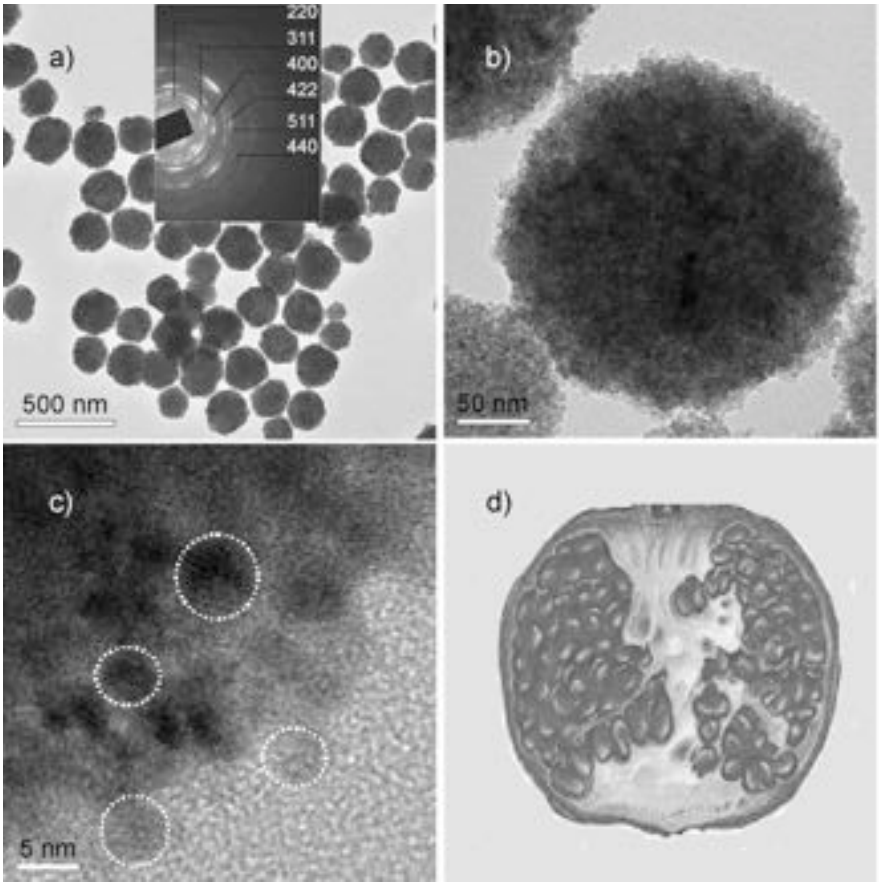

Figure 1-7 . *a) TEM images of the solvothermal reduction method synthesized Fe_3O_4 particles b) TEM image at higher magnification, c) HRTEM image. (d) The nanoparticle structure resemble a pomegranate. Taken from [84]*

electrostatic stabilizer. The mechanism is not fully clear to date. The resulting magnetite particles have an average size of 250 nm, and the size can be adjusted by changing the amount of trisodium citrate and the initial $FeCl_3$ concentrations, resulting particles range in size from 80 nm

to 410 nm [84] (**Figure 1-7**). Varying the n-octylamine (the reductant) to n-octanol (the solvent) volume ratio, Tian *et al* could control the resulting Fe_3O_4 MNPs size distribution within one nanometer [85]

1.5.1.4 Microemulsion

A microemulsion is a thermodynamically stable isotropic dispersion of two immiscible liquids consisting of nanosized domains of one liquid in the other, stabilized by surfactant molecules [86]. A soluble metal salts will lodge into the aqueous microdroplets wrapped by oil, and the co-precipitation of two reactants occur in the water droplets after continuous collision, coalescence, and breaking. The growth in microemulsion was suggested to involve inter-droplet exchange and nuclei aggregation. The resulting nanoparticles can be extracted by filtering or centrifuging after adding an organic solvent to induce precipitate. Reverse micelles are formed if water is added into oil and surfactant solution, and the particle size can be controlled by the concentration of the reactants dissolved in water, the water to surfactant ratio and the atmospheric conditions [87]. This method can produce very uniform particles (<10% variability). Similar to thermal decomposition, MNPs produced using microemulsion are soluble only in non-polar solvents and requires several washing processes and further stabilization treatments. Moreover, the yield of nanoparticles is relatively low compared to thermal decomposition and co-precipitation [88].

Okoli *et al* [89] used two different microemulsion systems to synthesize MNPs rangeing from 6–50 nm (**Figure 1-8**). The synthesized MNPs were applied for protein binding and separation [90]. A core/shell Fe/Fe_3O_4 nanoparticles were produced by reducing ferric chloride

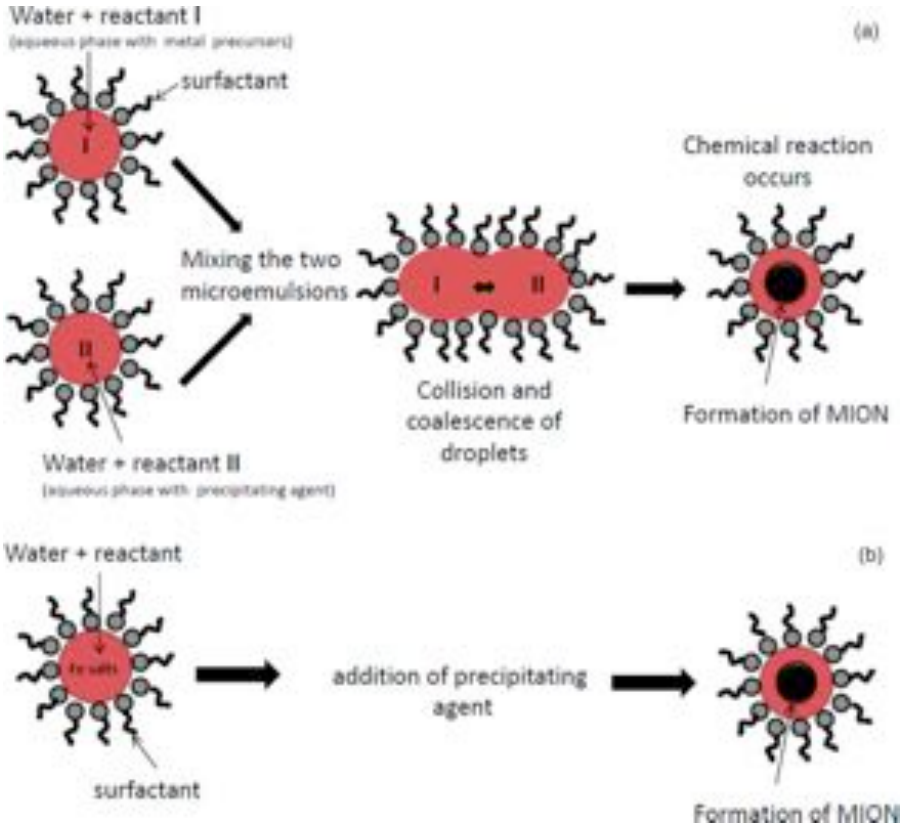

Figure 1-8. *Schematic of two different microemulsion approaches to synthesize MNPs. MION= nanoparticles Taken from [89]*

with sodium borohydride in microemulsions [91]. The average size of the particles was controlled by the oil phase to water phase ratio, higher oil phase ratio resulted in smaller particle diameters. Y. Lee *et al* synthesized mixed metal ferrites including cobalt ferrite, manganese ferrite, nickel ferrite, and zinc ferrite range from 2 nm to 10 nm by varying the relative concentrations of the iron salts, surfactant, and solvent [92]

1.5.2 Surface Modification

After the magnetic core synthesis, a coating is needed to prevent aggregation, render the nanoparticles water-soluble, biocompatible, or/and provide functionality for the conjugation of biomolecules. A variety of approaches have been developed to coat magnetic nanoparticles (chelators, antibodies, enzymes etc.) for applications including data storage, protein and cell separation and sorting, magnetic fluid hyperthermia (MFH), drug delivery, and magnetic resonance imaging (MRI). In this report, we will focus on different techniques to modify NMPs with silica for nucleic acid work up. The silica coating renders the particles stable, biologically inert and biocompatible. More importantly, nucleic acids bind to the silica surface in an entropically driven process induced by high concentrations of a chaotrope, which is the basis for nucleic acid separation and the "Pinwheel Assay". [93]

1.5.2.1 Sol-Gel (Stöber Reaction is the sol-gel process at pH>>7)

The Stöber reaction is regarded as the simplest and most effective route to synthesize mono-dispersed silica particles as well as for silica coating [94-96]. It refers to a process of hydrolysis of tetraethyl orthosilicate (TEOS), followed by condensation of silicic acid in a solution containing low molar mass alcohol and ammonia as a catalyst. The hydrolysis reaction

$$Si(OC_2H_5)_4 + xH_2O \rightarrow Si(OC_2H_5)_{4-x}(OH)x + x\ C_2H_5OH \qquad (2)$$

$$\equiv SiOH + \equiv SiOH \rightarrow \equiv Si\text{-}O\text{-}Si \equiv + H_2O \qquad (3)$$

$$\equiv Si - OC_2H_5 + \equiv SiOH \rightarrow \equiv Si - O - Si \equiv + C_2H_5OH \qquad (4)$$

$$Si(OC_2H_5)_4 + 2\ H_2O \rightarrow SiO_2 + 4\ C_2H_5OH \qquad (5)$$

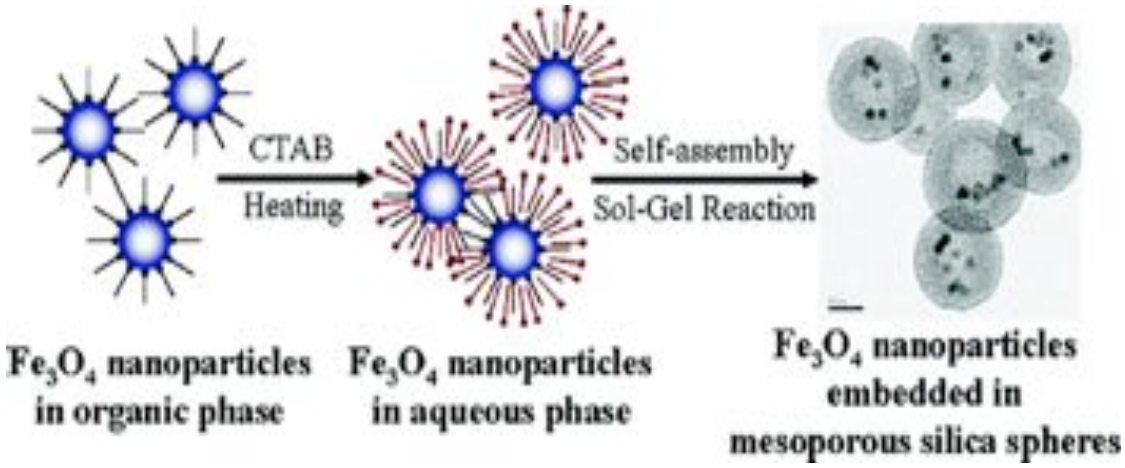

Figure 1-9. *Synthesis procedure of the magnetite embedded silica spheres. CTAB was used to transfer the hydrophobic ligand-capped nanocrystals from organic phase to aqueous phase. Taken from [93]*

is a nucleophilic substitution (SN2) which involves the displacement of the ethoxy group of TEOS by OH^- through a pentacoordinate transition state. As shown in equation (2), it has first-order kinetic dependence on the concentration of both TEOS and OH^-. The condensation process occurs immediately after hydrolysis and the hydroxy group from resulting intermediate $Si(OC_2H_5)_{4-x}(OH)_x$ either react with another intermediate (equation 3) or react with an intact TEOS (equation 4) to form a Si-O-Si bridge. The overall reaction is shown in equation 6 [97]. The coating thickness can be adjusted by the concentration of ammonium and the ratio of tetraethoxysilane (TEOS) to H_2O.

Lu *et al* reported a sol-gel approach to coat the SPIONs with uniform shells of amorphous silica. The resulting silica coating ranges from 2-100 nm, controlled by the concentration of the sol-gel solution [98]. Liu *et al* described a two step silica coating process, sol−gel followed by dense liquid coatings of maghemite [98]. Many researchers have also

applied ultrasonic irradiation to prevent the agglomeration of iron oxide cores during the coating process and accelerate the hydrolysis and condensation of TEOS [99-101]. Different approaches have been taken to prepare multifunctional silica coated MNPs, MNPs combined with quantum dots (QDs) compose a special particle named fluorescent magnetic composite nanoparticles (FMCNPs), which possess the advantages of both MNPs and QDs. J. Kim *et al* synthesized mono dispersed magnetite nanocrystals embedded in mesoporous silica spheres (**Figure 1-9**), and embedded CdSe/ZnS quantum dots in the same particles as a tracking agent [102].

1.5.2.2 Reverse Microemulsion

Compared with the Stöber reaction, reverse microemulsion has better control over the step of silica nucleation, which results in better particle monodispersity and more uniform spheres; microemulsion are also more tolerant with various reaction conditions. There are two types of reverse microemulsion methods: post coat synthesized cores within the droplets, and synthesize of the core and silica shell simultaneously in situ. In both cases, the choice of surfactant determines the micelle size and in turn affects the thickness and homogeneity of the silica coating.

Santra *et al* applied the water-in-oil microemulsion method for the preparation of silica-coated iron oxide nanoparticles. Different nonionic surfactants have been used for the preparation of microemulsions, and their effects on the particle size, crystallinity, and the magnetic properties have been studied. A uniform silica coating as thin as 1 nm was achieved by microemulsion [103]. Liu *et al* used Brij56 micelles as pore templates to prepare magnetic silica nanospheres with large nanopores for DNA adsorption and delivery [104]. Yi *et al* reported

multifunctional particles, dispersed in cyclohexane, where MNPs and quantum dots were embedded in the same silica shell [105].

While silica coating on metal oxides has been proven robust and routine, silica deposition directly on a metal core is still a challenge, due to the lack of OH group on the metal surface, and the easy oxidation of the metal. A primer coating is often required before silica deposition [106]. There are many good reviews on iron oxide@silica particles for extended reading.

1.5.3. Magnetic properties

MNPs have many unique magnetic properties such as super-paramagnetism, low Curie temperature, high coercivity, and high magnetic susceptibility. The magnetic properties of nanoparticles are determined by many factors, including the chemical composition, the type and the degree of defectiveness of the crystal lattice, the particle morphology, size, shape, and the interaction of the particle with the matrix. The magnetic characteristics of the material can be controlled based on these factors [107].

A spinning charged particle creates a magnetic dipole called a magneton. In ferro- and ferrimagnetic materials, magnetons are associated in groups, and they will be either aligned parallel or antiparallel according to the details of the interaction. Once the magnetization is aligned with an easy direction, the magnetization has to overcome an energy barrier, called the anisotropy energy, in order to switch them from one axis to another. At sufficiently high temperatures (>blocking temperature T_b), thermal fluctuation energy surpasses anisotropy energy, therefore magnetization can randomly flip its direction. The mean time between two flips is called the Néel relaxation time (T_N) [108]. If the time required to measure the

magnetization of the nanoparticles (T_M) is much longer than the Néel relaxation time ($T_M >> T_N$), i.e., the magnetization of the nanoparticle flip several times during the measurement, then the measured net magnetization will be zero in the absence of an external field. This characterizes the material as in its superparamagnetic state[109], and that means that they are attracted to a magnetic field but retain no residual magnetism after the field is removed. This property avoids any active behavior of the particles when there is no applied field and prevents aggregation. The blocking temperature T_b is defined as the temperature when $T_M = T_N$.

Another characteristic temperature is known as the Curie temperature, or the temperature at which ferro- or ferrimagnetic substance becomes paramagnetic. The difference between superparamagnetism and paramagnetism is that superparamagnetism describes the state of a single-domained grain, while paramagnetism is multi-domain. Domains are groups of spins that point in the same direction and act cooperatively. As the particle size decreases, the formation of domain walls becomes energetically unfavorable, and when the particle size reaches a critical number, they become single domaine [110]. Magnetic susceptibility (χ), defined by the ratio of the induced magnetization (M) to the applied magnetic field (H), indicates how easily the material can be magnetized, or how responsive the material is to an external magnetic field. The coupling interactions in single magnetic domain superparamagnetic materials result in higher magnetic susceptibilities than paramagnetic materials.

The reaction of magnetic materials on an applied magnetic field is described by a hysteresis loop, which includes two main parameters that represent a memory of a material to an applied magnetic field: remanence and coercivity, and they represent a memory of the material to

applied magnetic field. Ferro-and ferrimagnetic particles usually have large remanence and coercivity, while superparamagnetic particles have zero coercivity and no hysteresis.

1.6 References

1 Sackmann, E. K., Fulton, A. L., & Beebe, D. J. (2014). The present and future role of microfluidics in biomedical research. ***Nature***, 507(7491), 181–9.

2. Chin, C. D., Laksanasopin, T., *et al*. (2011). Microfluidics-based diagnostics of infectious diseases in the developing world. ***Nature Medicine***, 17(8), 1015–1019.

3. Khademhosseini, A. (2011). Nano/microfluidics for diagnosis of infectious diseases in developing countries. ***Adv Drug Delivery Rev***, 62, 449–457.

4. Warren, A. D., Kwong, G. a, *et al* (2014). Point-of-care diagnostics for noncommunicable diseases using synthetic urinary biomarkers and paper microfluidics. ***Proc Natl Acad Sci U S A***, 111(10), 3671–6.

5. Mao, X., & Huang, T. J. (2012). Microfluidic diagnostics for the developing world. ***Lab on a Chip***, 12(8), 1412.

6. Easley, C. J., Karlinsey, J. M., Bienvenue, J. M., Legendre, L. A., Roper, M. G., Feldman, S. H., … Landers, J. P. (2006). A fully integrated microfluidic genetic analysis system with sample-in-answer-out capability. ***Proc Natl Acad Sci U S A***, 103(51), 19272–19277.

7. Breadmore, M. C., Wolfe, K. A., Arcibal, I. G., Leung, W. K., Dickson, D., Giordano, B. C., … Landers, J. P. (2003). Microchip-Based Purification of DNA from Biological Samples. Analytical Chemistry, 75(8), 1880–1886.

8. Giordano, B. C., Ferrance, J., Swedberg, S., Hühmer, a F., & Landers, J. P. (2001). Polymerase chain reaction in polymeric microchips: DNA amplification in less than 240 seconds. Analytical Biochemistry, 291(1), 124–132.

9. Lounsbury, J. a, Karlsson, A., Miranian, D. C., Cronk, S. M., Nelson, D. a, Li, J., … Landers, J. P. (2013). From sample to PCR product in under 45 minutes: a polymeric integrated microdevice for clinical and forensic DNA analysis. Lab on a Chip, 13(7).

10. Bienvenue, J. M., Duncalf, N., Marchiarullo, D., Ferrance, J. P., & Landers, J. P. (2006). Microchip-based cell lysis and DNA extraction from sperm cells for application to forensic analysis. Journal of Forensic Sciences, 51(2), 266–273.

11. McDonald, J. C., & Whitesides, G. M. (2002). Poly(dimethylsiloxane) as a material for fabricating microfluidic devices. ***Accounts of Chemical Research***, 35(7), 491–9.

12. Casquillas, G., 2014. PDMS: A Review. Elveflow.

13. Fujii, T. (2002). PDMS-based microfluidic devices for biomedical applications. ***Microelectronic Engineering***, 61-62, 907–914.

14. Sia, Samuel K., and George M. Whitesides. "Microfluidic devices fabricated in poly (dimethylsiloxane) for biological studies." ***Electrophoresis*** 24.21 (2003): 3563-3576.

15. Yoojin Shin *et al.* Microfluidic assay for simultaneous culture of multiple cell types on surfaces or within hydrogels. ***Nature Protocols*** 7,1247–1259 (2012).

16. Qin, D., Xia, Y., & Whitesides, G. M. (2010). Soft lithography for micro- and nanoscale patterning. ***Nature Protocols***, 5(3), 491–502.

17. Grimes, A., Breslauer, D. N., Long, M., Pegan, J., Lee, L. P., & Khine, M. (2008). Shrinky-Dink microfluidics: rapid generation of deep and rounded patterns. ***Lab on a Chip***, 8(1), 170–172.

18. Wolfe, B. D. B., Ashcom, J. B., Hwang, J. C., Schaffer, C. B., Mazur, E., & Whitesides, G. M. (2003). Customization of Poly(dimethylsiloxane) Stamps by Micromachining Using a Femtosecond-Pulsed Laser. ***Adv Material***, (1), 62–65.

19. Corporation., D. C. (2005). Information about Dow Corning Silicone Encapsulants.

20. Huang, R., et al., Non-linear mechanical behavior of polydimethylsiloxane (PDMS): application to the manufacture of microfluidic devices. IMST. 2004.

21. Bodas, D., and Khan-Malek, C., Hydeophilization and Hydrophobic Recovery of PDMS by Oxygen Plasma and Chemical Treatment – An SEM Investigation. Sensors and ***Actuators B: Chemical.*** 2007.

22. Say Hwa Tan *et al.* Oxygen plasma treatment for reducing hydrophobicity of a sealed polydimethylsiloxane microchannel. ***Biomicrofluidics***. 2010 Sep; 4(3): 032204.

23. Lee,J.N., Park,C. Whitesides,G.M.(2003).Solvent Compatibility of Poly(dimethylsiloxane) Based Microfluidic Devices. ***Analytical Chemistry.*** 75(23), 6544–6554.

24. Vickers, J. a, Caulum, M. M., & Henry, C. S. (2006). Generation of hydrophilic poly(dimethylsiloxane) for high-performance microchip electrophoresis. ***Analytical Chemistry***, 78(21), 7446–52.

25. C. L. do Lago, H. D. T. da Silva, C. A. Neves, J. G. A. Brito-Neto and J. A. F. da Silva, A Dry Process for Production of Microfluidic Devices Based on the Lamination of Laser-Printed Polyester Films. ***Anal. Chem***., 2003, 75, 3853–8.

26. G. R. M. Duarte, C. W. Price, B. H. Augustine, E. Carrilho and J. P. Landers, Dynamic Solid Phase DNA Extraction and PCR Amplification in Polyester-Toner Based Microchip. ***Anal. Chem***, 2011, 83, 5182–5189.

27. Piccin, E., Ferraro, D., Sartori, P., Chiarello, E., Pierno, M., & Mistura, G. (2014). Generation of water-in-oil and oil-in-water microdroplets in polyester-toner microfluidic devices. ***Sensors and Actuators, B: Chemical***, 196, 525–531.

28. Ouyang, Y., Wang, S., Li, J., & Riehl, P. (2013). Rapid patterning of "tunable"hydrophobic valves on disposable microchips by laser printer lithography. ***Lab on a Chip***, 13(9), 1762–71.

29. Thompson, B. L., Ouyang, Y., Duarte, G. R. M., Carrilho, E., Krauss, S. T., Landers, J. P. (2015). Inexpensive, rapid prototyping of microfluidic devices using overhead transparencies and a laser print, cut and laminate fabrication method. ***Nature Protocols***, 10(6), 875–886.

30. Ouyang, Y., Li, J., & Landers, J. P. (2013). Integration of Pinwheel Assay on a Cd-Like Microchip for Dna Quantitation, (October), 1613–1615.

31. Martinez, A.W.; Phillips, S.T.;Whitesides,G.M.;Carrilho,E.Diagnostics for the developing world: Microfluidic paper-based analytical devices. ***Anal. Chem***. 2010, 82, 3–10.

32. Lu et al. ***Anal. Chem***. 2010, 82, 329–335.

33. Martinez, A. W., Phillips, S. T., Whitesides, G. M. and Carrilho, E., Diagnostics for the developing world: microfluidic paper-based analytical devices, ***Anal. Chem.,*** 2010, 82, 3-10.

34. Martinez, A. W., Phillips, S. T. and Whitesides, G. M., Three-dimensional microfluidic devices fabricated in layered paper and tape, ***Proc. Natl. Acad. Sci.*** USA, 2008, 105, 19606-19611.

35. Liu, H., & Crooks, R. M. (2011). Three-dimensional paper microfluidic devices assembled using the principles of origami. ***JACS***, 133(44), 17564–17566.

36. Abe, K.; Suzuki, K.; Citterio, D. Inkjet-printed microfluidic multianalyte chemical sensing paper. ***Anal. Chem.*** 2008, 80, 6928–6934.

37. Dungchai, W.; Chailapakul, O.; Henry, C.S. Electrochemical detection for paper-based microfluidics. ***Anal. Chem.*** 2009, 81, 5821–5826.

38. Ge, L.; Wang, S.; Song, X.; Ge, S.; Yu, J. 3D origami-based multifunction-integrated immunodevice: Low-cost and multiplexed sandwich chemiluminescence immunoassay on microfluidic paper-based analytical device. ***Lab Chip*** 2012, 12, 3150–3158.

. Delaney, J.L.; Hogan, C.F.; Tian, J.F.; Shen, W. Electrogenerated chemiluminescence detection in paper-based microfluidic sensors. ***Anal. Chem.*** 2011, 83, 1300–1306.

40. Steffens, C.; Manzoli, A.; Francheschi, E.; Corazza, M.; Corazza, F.; Oliveira, J.V.; Herrmann, P. Low-cost sensors developed on paper by line patterning with graphite and polyaniline coating with supercritical CO_2. ***Synth. Met.*** 2009, 159, 2329–2332.

41. Wang, J.; Monton, M. R. N.; Zhang, X.; Filipe, C. D. M.; Pelton, R.; Brennan, J. D. ***Lab Chip*** 2014, 14, 691−695.

42. Olkkonen, J.; Lehtinen, K.; Erho, T. ***Anal. Chem***. 2010, 82, 10246−10250.

43. Demirel, G.; Babur, E. ***Analyst*** 2014, 1, 2326−2331

44. Bagherbaigi, S.; Córcoles, E. P.; Wicaksono, D. H. B. ***Anal. Methods*** 2014, 6, 7175

45. Park, T. S.; Li, W.; McCracken, K. E.; Yoon, J. Y. ***Lab Chip*** 2013, 13, 4832−4840.

46. Jayawardane, B. M.; Coo, d. L.; Cattrall, W. R.; Kolev, D. S. ***Anal. Chim. Acta*** 2013, 803, 106−112.

47. Kumar & Clark (2005). 8. Clinical Medicine (Sixth ed.). Elsevier Saunders. p. 469.

48. Abrams CS. Thrombocytopenia. In: Goldman L, Schafer AI, eds.Cecil Medicine

49. Purves, William K.; Sadava, David; Orians, Gordon H.; Heller, H. Craig (2004). Life: The Science of Biology (7th ed.). Sunderland, Mass: Sinauer Associates. p. 954.

50. Williams, S. C. (2013). Circulating tumor cells. ***Proc Natl Acad Sci U S A***, 110(13), 4861.

51. K. T. Kotz, ***et al***. Clinical microfluidics for neutrophil genomics and proteomics.***Nat. Med.*** 2010 , 16 (9), 1042 – 7 .

52. S. Nagrath, L. V. *et al.* Isolation of rare circulating tumour cells in cancer patients by microchip technology. ***Nature*** 2007, 450 (7173), 1235 – 9 .

53. Petersson,F.,Åberg,L.,Swärd-Nilsson,A.M.,&Laurell,T.(2007).Free flow acoustophoresis: Microfluidic-based mode of particle and cell separation. ***Anal Chem***, 79(14)

54. Li, P., Mao, Z., Peng, Z., Zhou, L., Chen, Y., Huang, P., & Truica, C. I. (2015). Acoustic separation of circulating tumor cells, ***PNAS***. 112(16), 4970–4975.

55. (a) P. Wilding , J. Pfahler , H. H. Bau , J. N. Zemel , L. J. Kricka , ***Clin. Chem.*** 1994 , 40 (1), 43 – 7 (b) D. Lee , P. Sukumar , A. Mahyuddin , M. Choolani , G. Xu , ***J.***

Chromatogr. A 2010 , 1217 (11), 1862 – 6. (c) P. Sethu , A. Sin , M. Toner , ***Lab Chip*** 2006 , 6 (1), 83 – 9 . (d) H. Mohamed , L. D. McCurdy , D. H. Szarowski , S. Duva ,J. N. Turner , M. Caggana , ***IEEE Trans. NanoBiosci.*** 2004 , 3 (4).251 – 6 .

56. (a). (c)Fiedler S, Shirley SG, Schnelle T, Fuhr G. Dielectrophoretic sorting of particles and cells in a microsystem. ***Anal. Chem***. 1998; 70(9):1909–1915 (d) Holmes D, Green NG, Morgan H. Microdevices for dielectrophoretic flow-through cell separation. ***IEEE Eng. Med. Biol. Mag***. 2003; 22(6):85–90.
57. Kost GJ. Guidelines for point-of-care testing: improving patient outcomes. ***Am J Clin Pathol***. 1995;104(suppl 1):S111-S127.
58. Theranos (Sep 11, 2012). "Methods and systems for assessing clinical outcomes". US Patent Office. Retrieved 14 April 2015.
59. Walgreens, Inc.., 2015, "Theranos Lab Testing: Test menu," at Walgreens:Pharmacy & Health. https://www.theranos.com/test-menu?ref=for_providers.
60. Wynberg, E., Cooke, G., Shroufi, A., Reid, S. D., & Ford, N. (2014). Impact of point-of-care CD4 testing on linkage to HIV care: A systematic review. ***Journal of the International AIDS Society***
61. LaMer, V., & Dinegar, R. Theory, production and mechanism of formation of monodispersed hydrosols. ***Journal of the American Chemical Society,*** 1950 72(8), 4847–4854.
62. Chourpa, I., *et al*. Molecular composition of iron oxide nanoparticles, precursors for magnetic drug targeting, as characterized by confocal Raman microspectroscopy. ***Analyst***, 2006, 130(10), 15–1403.

63. Yu, X., *et al*. One-step synthesis of magnetic composites of cellulose@iron oxide nanoparticles for arsenic removal. ***Journal of Materials Chemistry A***, 2013, 1(3), 959–965.

64. Xie, J *et al,* Iron oxide nanoparticle platform for biomedical applications. ***Curr. Med. Chem***. 2009, 16, 1278–1294.

65. Suh, S. K.,*et al.* Synthesis of Nonspherical Superparamagnetic Particles: In Situ Coprecipitation of Magnetic Nanoparticles in Microgels Prepared by Stop-Flow Lithography. ***Journal of the American Chemical Society***, 2012, 134(17), 7337–7343.

66. Barick, K. C. *et al*. Novel and efficient MR active aqueous colloidal Fe3O4 nanoassemblies. ***Journal of Materials Chemistry***, 2009, 19(38), 7023–7029.

67. Rockenberger, J. *et al*. A New Nonhydrolytic Single-Precursor Approach to Surfactant-Capped Nanocrystals of Transition Metal Oxides. ***Journal of the American Chemical Society***, 1999, 121(49), 11595–11596.

68. Hyeon, T. *et al*. Synthesis of Highly Crystalline and Monodisperse Maghemite Nanocrystallites without a Size-Selection Process. ***Journal of the American Chemical Society***, 2001, 123(51), 12798–12801.

69. Sun, S., & Zeng, H. Size-Controlled Synthesis of Magnetite Nanoparticles. ***Journal of the American Chemical Society***, 2002, 124(28), 8204–8205.

70. Sun, S.*et al*. Monodisperse MFe2O4 (M = Fe, Co, Mn) Nanoparticles. ***Journal of the American Chemical Society***, 2003, 126(1), 273–279.

71. Tirosh, E., Shemer, G., & Markovich, G.. Optimizing Cobalt Ferrite Nanocrystal Synthesis Using a Magneto-optical Probe. ***Chemistry of Materials***, 2005,18(2), 465–470.

72. Chaubey, G.*et al*. Synthesis and Stabilization of FeCo Nanoparticles. ***Journal of the American Chemical Society,*** 2007, 129(23), 7214–7215.

73. Miguel-Sancho,*et al*. Synthesis of Magnetic Nanocrystals by Thermal Decomposition in Glycol Media: Effect of Process Variables and Mechanistic Study. ***Industrial & Engineering Chemistry Research***, 2012, 51(25), 8348–8357.

74. Deng, H. *et al*, Monodisperse Magnetic Single-Crystal Ferrite Microspheres. ***Angew. Chem. Int. Ed.***, 2005, 44: 2782–2785.

75. Cheng, C. *et al*. Tunable synthesis of carboxyl-functionalized magnetite nanocrystal clusters with uniform size. ***Journal of Materials Chemistry***, 2009, 19(46), 8782–8788.

76. Ge, J. *et al*, Superparamagnetic Magnetite Colloidal Nanocrystal Clusters. ***Angew. Chem. Int. Ed.,*** 2007, 46: 4342–4345.

77. Si, S. *et al*. Magnetic Monodisperse Fe_3O_4 Nanoparticles. ***Crystal Growth & Design***, 2005, 5(2), 1–3.

78. X. Wang, *et al*. A general strategy for nanocrystal synthesis. ***Nature***, 2005, 437, 121-124.

79. Jia, X. *et al*. Environmentally-friendly preparation of water-dispersible magnetite nanoparticles. ***Chemical Communications,*** 2009, 0(8), 968–970.

80. Wang, J. *et al*. Synthesis of monodisperse nanocrystals of high crystallinity magnetite through solvothermal process. ***Materials Chemistry and Physics***, 2009,113(1), 6–9.

81. Liu, J. *et al*. Highly water-dispersible biocompatible magnetite particles with low cytotoxicity stabilized by citrate groups. ***Angewandte Chemie***, 2009, 48(32), 5875–9.

82. Tian, Y. *et al* Facile solvothermal synthesis of monodisperse Fe3O4 nanocrystals with precise size control of one nanometre as potential MRI contrast agents. ***Journal of Materials Chemistry***, 2011,21(8), 2476–2481.

83. A. Drmota, *et al* Microemulsion Method for Synthesis of Magnetic Oxide Nanoparticles. ISBN 978-953-51-0247-2, Published: March 16, 2012.

84. Nguyen Thai Ha *et al* Effects of the conditions of the microemulsion preparation on the properties of Fe3O4 nanoparticles . ***VNU Journal of Science Natural Sciences and Technology.*** 2008, 24, 9-15.

85. Lu, A.-H. *et al.* Magnetic Nanoparticles: Synthesis, Protection, Functionalization, and Application. ***Angew. Chem. Int. Ed.***, 2007, 46: 1222–1244.

86. Okoli, C *et al*. Application of magnetic iron oxide nanoparticles prepared from microemulsions for protein purification. ***J. Chem. Technol. Biotechnol.***, 2011, 86: 1386–13.

87. Okoli, C. *et al*. Comparison and Functionalization Study of Microemulsion-Prepared Magnetic Iron Oxide Nanoparticles. ***Langmuir***, 2012, 28(22), 8479–8485.

88. Zhang, G *et al*. Surface engineering of core/shell iron/iron oxide nanoparticles from microemulsions for hyperthermia. ***Materials Science and Engineering C,*** 2010, 30(1), 92–97.

89. Lee, Y. *et al*, Large-Scale Synthesis of Uniform and Crystalline Magnetite Nanoparticles Using Reverse Micelles as Nanoreactors under Reflux Conditions. ***Adv. Funct. Mater.,*** 2005, 15: 503–509.

90. Melzak, K. A. *et al*. Driving forces for DNA adsorption to silica in perchlorate solutions. ***J Colloid Interface Sci***, 1996, 181(2), 635–644.

91. Werner Stöber, Arthur Fink, Ernst Bohn. Controlled growth of monodisperse silica spheres in the micron size range. ***Journal of Colloid and Interface Science,*** 1968, 26(1) 62-69.

92. Kolbe, G., Ph.D. thesis, Jena, Germany, 1956.

93. H.C. Wang, *et al*, Analysis of Parameters and Interaction between Parameters in Preparation of Uniform Silicon Dioxide Nanoparticles Using Response Surface Methodology. ***Ind. Eng. Chem. Res***. 2006, 45 8043–8048.

94. Chou, K.S. and Chen, C.C, Preparation of Monodispersed Silica Colloids Using Sol Gel Method: Cosolvent Effect. From book innovative Processing and Synthesis of Ceramics, ***Glasses and Composites VIII***, Volume 166, 2006.

95. Lu, Y. *et al*. Modifying the Surface Properties of Superparamagnetic Iron Oxide Nanoparticles through A Sol−Gel Approach. ***Nano Letters***, 2002, 2(3), 183–186.

96. Liu, Q. *et al*. A Novel Two-Step Silica-Coating Process for Engineering Magnetic Nanocomposites. ***Chemistry of Materials***, 1998, 10(12), 36–40.

97. N. Enomoto, S. Maruyama, Z. Nakagawa. ***J. Mater. Res.***, 1997, 12, 1410–1415.

98. N. Enomoto, A. Funakoshi, M. Uehara, J. Hojo, in: ***Proc. 11th Annual Mtg. Jpn. Soc. Sonochem,*** 2002, 18–20.

99. Dang, F. *et al*. Sonochemical coating of magnetite nanoparticles with silica. ***Ultrasonics Sonochemistry***, 2010, 17(1), 193–199.

100. Kim, J. *et al*. Magnetic Fluorescent Delivery Vehicle Using Uniform Mesoporous Silica Spheres Embedded with Monodisperse Magnetic and Semiconductor Nanocrystals. ***Journal of the American Chemical Society***, 2005, 128(3), 688–689.

101. Santra, S. *et al*. Synthesis and Characterization of Silica-Coated Iron Oxide Nanoparticles in Microemulsion: The Effect of Nonionic Surfactants. ***Langmuir,*** 2001, 17(10), 2900–2906.

102. Liu, J. *et al.* Magnetic silica spheres with large nanopores for nucleic acid adsorption and cellular uptake. ***Biomaterials***, 2012, 33(3), 970–978.

103. Yi, D. K. *et al*. Silica-Coated Nanocomposites of Magnetic Nanoparticles and Quantum Dots. ***Journal of the American Chemical Society***, 2005, 127(14), 4990–4991.

104. Liz-Marzan, L. M., Giersig, M., & Mulvaney, P. Homogeneous silica coating of vitreophobic colloids. ***Chemical Communications***, 1996, 0(6), 731–732.

105. Guerrero-Martínez, A *et al*. Recent Progress on Silica Coating of Nanoparticles and Related Nanomaterials. ***Adv. Mater.*** 2010, 22: 1182–1195.

106. Preparation and biomedical applications of core-shell silica/magnetic nanoparticle composites. ***J Nanosci Nanotechnol***. 2012 Apr;12(4):2964-72.

107. Seo, W. S. *et al*, Size-Dependent Magnetic Properties of Colloidal Mn3O4 and MnO Nanoparticles. ***Angew. Chem. Int. Ed.***, 2004, 43: 1115–1117.

108. Neel, L. Ann. Geophys. (C. N. R. S.) 1949, 5, 99.

109. C. P. Bean and J. D. Livingston. Superparamagnetism. ***J. Appl. Phys***. 1959, 30, S120;

110. Leslie-Pelecky, D. L., & Rieke, R. D. Magnetic Properties of Nanostructured Materials. ***Chemistry of Materials***, 1996, 8(8), 1770–178

Chapter 2. DNA-Bead Aggregation for CD4+ T-cells Counting

2.1 Overview

A CD4+ T-cells count indicates the progress of HIV infection in patients and the effectiveness of antiretroviral therapy (ART) [1-3]. State-of-the-art CD4 counting methods based on flow cytometry are too taxing for resource-limited regions, due to their high technical requirement and cost [7-10]. Here we present a cost-effective and label-free method, integrating immunomagnetic separation and the pinwheel assay [12-14], to enumerate CD4+ T-cells. The accuracy of this prototype system was validated through testing in the United States and showed close agreement with standard flow cytometry (R^2=0.997) over a CD4 range from 2 cells/mm^3 to 1200 cells/mm^3, and was able to discriminate clinically relevant CD4 count thresholds with high sensitivity and specificity.

2.2 Introduction

CD4+ T-cells, or helper T-cells, are a type of white blood cells (WBCs) that express the surface glycoprotein cluster of differentiation 4 (**Figure 2-1**). Other WBCs including monocytes, marcrophage, and dendritic cells also express CD4 protein on the surface, however, macrophage and dentritic cells are very rare in the blood. Therefore, monocytes are the primary "contaminant" when trying to isolate CD4+ T-cells using antibodies. CD4+ T-cells orchestrate the immune system by sending signals to other T-cell subsets, B-cells and initiating innate immune responses [1]. CD4+ T-cells are the main targets of Human Immunodeficiency Virus (HIV), because the gp120 antigen for HIV is a mirror image of the surface CD4 protein, and

(A)

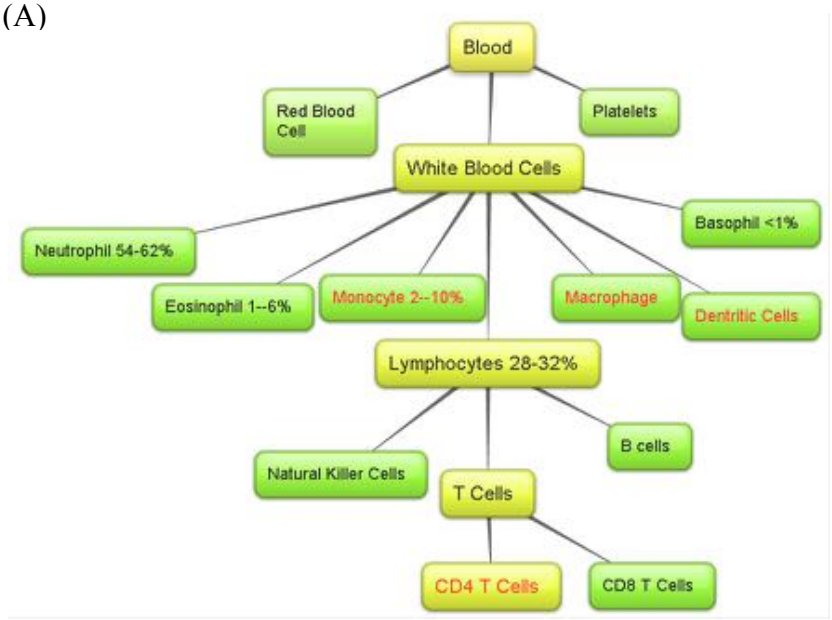

(B)

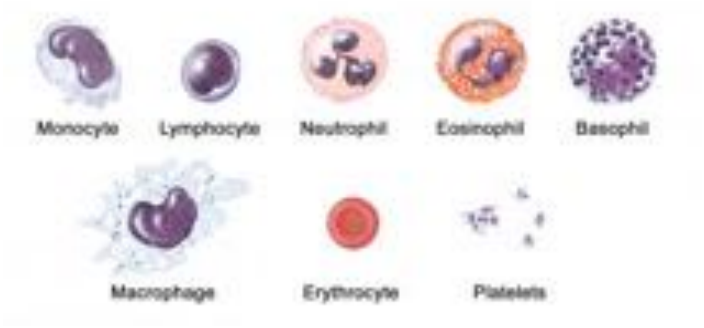

Figure 2-1. *Types of blood cells and their morphology. (A) Red letters indicate those express CD4 glycoprotein. (B) morphology of different types of blood cells.*

CD4+ T-cells are he host that HIV replicates. During the process of replication, the virus destroys an increasing numbers of T cells, therefore the number of CD4+ T-cells decrease as the infection progresses, leaving the patient susceptible to opportunistic infections. The most commonly utilized laboratory measurement for the clinical prognosis and therapy monitoring of

HIV infections is counting the CD4+ T-cells [2]. CD4 counting does not evaluate the virus load directly, and instead monitors the patient's immune system.

In a healthy adult, a normal CD4 count is 600 to 1200 cells per cubic millimeter of blood, with the median of 828 cells/mm^3 [3]. CD4+ T-cells need to be enumerated every three to six months after the patient is diagnosed with HIV infection to determine eligibility for antiretroviral therapy (ART). ART is a cocktail of HIV medicines, a HIV regimen, although ART can't cure HIV, it can help maintain the immune system in an effective state and reduce the risk of HIV transmission [4]. According to the new HIV treatment guidelines provided by the World Health Organization (WHO) in June 2013, it is recommended that HIV patients start ART when their CD4 count falls below 500 cells/μL. In some special cases, such as pregnant women, HIV-positive partners in serodiscordant couples, children under the age of five, and those with HIV-associated Hepatitis B and tuberculosis, immediate treatment is recommended [4]. CD4 count is also referred to by medical professionals to determine efficacy of treatment. Once the patient is taking stable HIV treatment, at first the CD4 count will be checked every three months or so during routine clinic visits. If the treatment has been working effectively, then there may be longer intervals between the CD4 tests. Some doctors think once a year could be sufficient. According to the US Center for Disease Control (CDC), patients progress to stage 3 infection, i.e., Acquired Immune Deficiency Syndrome (AIDS) when they have a CD4 count below 200 cells/μL [5].

Although portable lateral immunoassay kits are now available for HIV diagnosis and the cost for ART has dropped considerably during last several years ($188 per person annually for first-line ART drugs) [6], the diagnostic tests involved in monitoring the progression of HIV via

CD4+ T-cells counts remain a hurdle due to the lack of lab capacity for CD4 counting, which is a major obstacle in accelerated HIV treatment scale-up [4]. The most prevalent method for CD4 counting is flow cytometry [7], in which cells are labeled by fluorochrome conjugated monoclonal antibodies, hydro-dynamically focused into the center of a sheath fluid passage, and enumerated based on fluorescence emission. Many factors, including the cost of a flow cytometer (ranging from $30,000 to $225,000), technical and operational complexity, the need for reliable electricity, and the high cost of fluorescent reagents, have made flow cytometers impractical and difficult to sustain in resource limited settings, where more than 85% of HIV patients live[2]. The urgent need for affordable and technically simple CD4 diagnostics is widely recognized.

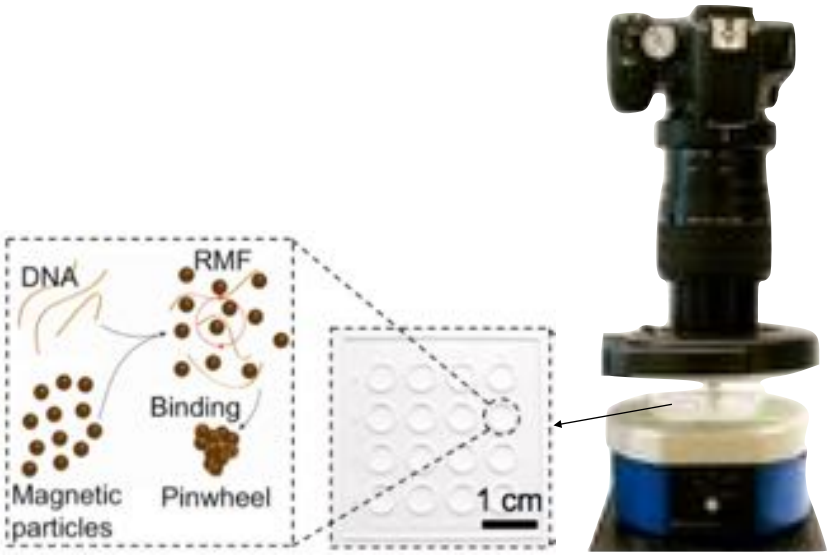

Figure 2-2. *Pinwheel assay experimental setup [94]. A 4x4 array of microwells created on a PMMA plate with a laser cutter. Samples and silica-coated magnetic particles are mixed in the microwells, and the plate is placed in a rotating magnetic field. Images of the particles are acquired using a microscope (2.5 X magnification) and a digital camera.*

It is well-established that DNA binds to silica beads in an entropically driven process induced by high concentrations of a chaotrope (e.g., guanidine hydrochloride (GdnHCl)) [11]. Under these or similar conditions, commercial magnetic silica beads interact with DNA, providing the basis for commercial DNA solid-phase extraction systems and the manipulation of beads in microfluidic environments through static magnetic fields. The "pinwheel assay" is a new approach that does not only extract, but also quantify the amount of DNA in biological samples, based on the visually detectable interaction of DNA with silica coated super-paramagnetic beads [12]. This assay quantitates DNA according to the formed aggregation of silica-coated magnetic particles and DNA, in the presence of a high concentration of chaotrope

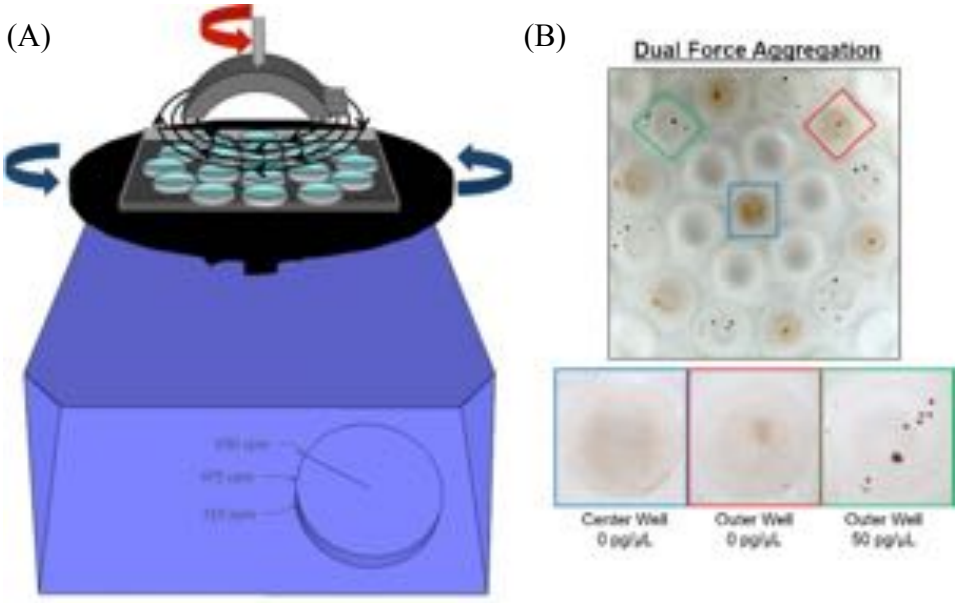

Figure 2-3. *Schematic representation of dual force aggregation set-up. A. The microdevice is placed in a foam frame atop an agitator while the MF rotates from above the device. B. A photograph of the 12-well microdevice with alternating concentrations of 0 pg µL^{-1} (red) and 12.5 pg µL^{-1} (green).*

under a rotating magnetic field (RMF). We have demonstrated that this assay is capable of quantitating DNA as low as 5 pg/μL, directly from raw samples.

Figure 2-2 shows the original "pinwheel assay" experimental setup, in a 4x4 array of microwells fabricated with Poly(methyl methacrylate) (PMMA), the DNA from various matrices is mixed with silica coated superparamagnetic particles and exposed to an appropriate RMF. The dark area represents the degree to which the particles have aggregated, and the calculated dark area is then normalized against a negative control to get the % Dark Area (%DA). Images of the aggregate reveal a correlation between the size of the aggregate and DNA mass, a higher %DA signifies a lower concentration of DNA present in the well.

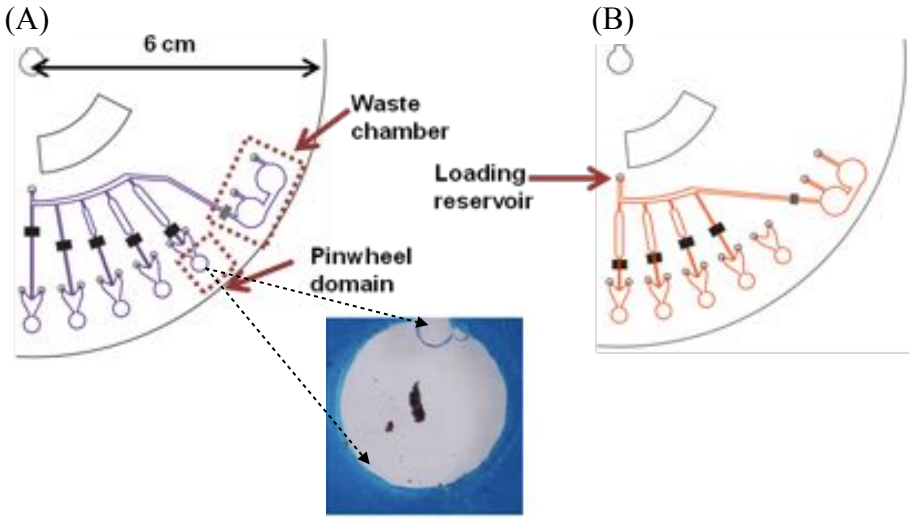

Figure 2-4. *Schematic design of microfluidic network for aliquoting sample (A) and buffer (B). Dark gray bar represents the hydrophobic toner patches serving as burst valve. The inset demonstrates the DNA-bead aggregation.*

In the original array set up, given the magnet that provide the RMF is of an arch bridge shape (Shown in **Figure 2-3 A**, the grey magnet on top), aggregation was found to only be effective at the center of the field (i.e., only the central well yields reproducible result). **Figure 2-3** shows a multiplexing dual-force aggregation (DFA) device that can analyze 12 samples simultaneously. A circular array of microwells was used and vortexer 'agitation' was incorporated as a second force that worked in concert with the RMF to generate effective aggregation. This approach allows for 1 sample to be interrogated for DNA content in 12 s [20].

Another multiplexing approach was later developed, and **Figure 2-4** shows a CD like centrifugal microchip that integrates parallel sample dilution and the pinwheel assay in a closed-chamber system. This device consists of 5 layers, with a sample loading zone on one side and the buffer loading zone on the flip side (**Figure 2-4 A and B**). This device can not only process multiple samples, but can also mix and generate calibration curves on board, minimizing manual steps for sample preparation and decreasing the operational time [21].

In this chapter, the original "pinwheel assay" is coupled with immunomagnetic assay to quantitate CD4+ T-cells.

2.3 Materials and Experimental Methods

2.3.1 Reagents Preparation

MagneSil paramagnetic particles were purchased from Promega (Madison, WI). GdnHCl was bought from MP Biomedicals (Solon, OH). MES was bought from Acros Organics. Tris base was bought from Fisher Scientific. Whole blood samples were donated by consenting donors. CD4 isolation kit was bought from Life Technologies. All solutions were prepared in Nanopure

water (Barnstead/Thermolyne, Dubuque, IA). Thirty microliters of stock MagneSil beads were washed once with deionized, distilled water (Nanopure) followed by one wash with GdnHCl solution (8 M, 1xTE, adjusted to pH 6.1 with 100 mM MES) and resuspended in 1 mL of GdnHCl solution to make the suspension.

2.3.2 Microwell Fabrication

A VersaLASER system 3.50 from Universal Laser Systems (Scottsdale, AZ) was used to fabricate microwells in 1.5-mm-thick PMMA purchased from McMaster-Carr (Santa Fe Springs, CA). Each microwell device was prepared with 5-mm-diameter circular wells on a 1x1-cm square device. The device was designed using CorelDRAW, and wells were created in the solid 1.5-mm-thick PMMA by laser cutting. The layer with holes was thermally bonded to a blank PMMA piece of the same dimensions using established methods. Microwells were sterilized with 10% bleach for 5−10 min and then rinsed with Nanopure water.

2.3.3 Rotating Magnetic Field (RMF) Application

Three microliters of stock MagneSil suspension was added to each microfluidic well, followed by 7 μL of 8M GdnHCl solution, 5 μL of TE buffer, and 5 μL of sample. The mixture was exposed to a RMF generated by a magnetic stirrer rotating at 2000 rpm with a U- shaped bipolar magnet of 2800 G for 5 min. The RMF was turned off to image and restarted for 5 s before imaging again.

2.3.4 Image Analysis

A gray level threshold was set in the images of magnetic beads and aggregates by an ISODATA algorithm written in Mathematica software, Iterative Self-Organizing Data Analysis Technique (ISODATA) is a method of unsupervised classification, where user defines threshold values for parameters, and computer runs algorithm through many iterations until threshold is reached. Many of the steps used in the algorithm are based on the experience obtained through experimentation, which identifies the pixels representing the beads and aggregates. The total number of these pixels in the photograph without DNA is defined as 100%, and as more DNA molecules are released from cells, tighter aggregation evolves, corresponding to a smaller percentage. The change of the percentage is defined as the degree of aggregation (DA). More DNA molecules result in tighter bead aggregation and lower DA values.

2.3.5 Calibration Curves

Samples were first incubated with GdnHCl solution in 1:100 volume ratio at room temperature for 30 min. The samples were then serially diluted in GdnHCl solution to appropriate concentrations. Five microliters of diluted sample, 3 μL of bead suspension, and 12 μL of GdnHCl were mixed and exposed to the RMF for 5 min, after which three photographs of the beads and aggregates were acquired for image analysis. The calibration curve was generated by correlating the mean DA value of three images for each diluted sample with the corresponding final cell concentration in the pinwheel assay.

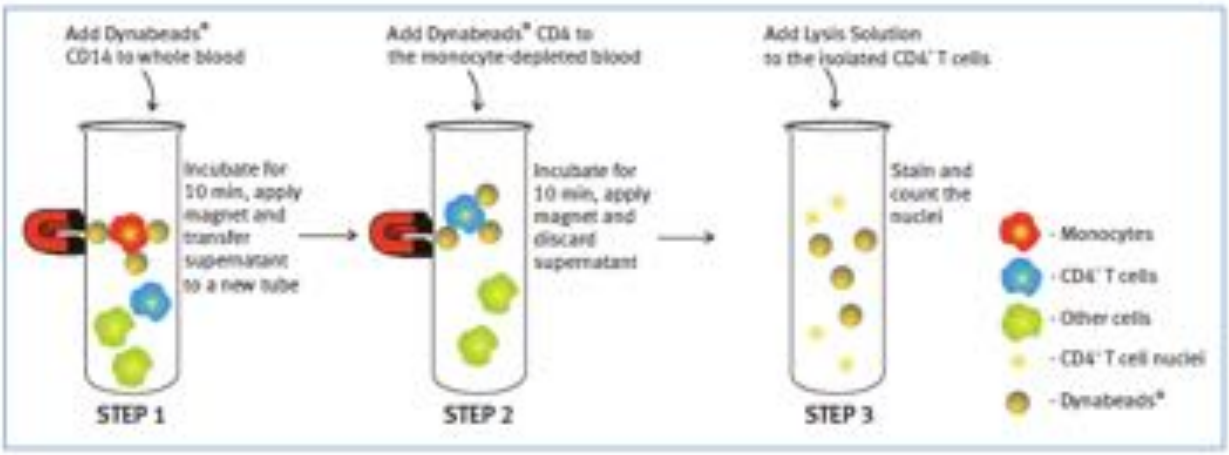

Figure 2-5. *Illustration of the Dyna® T4 Quant kit procedure. Positive isolation of CD4+ T-cells with pre-depletion of monocytes for reliable CD4+ T-cell nuclei counting. Step 1. Depletion of monocytes with Dynabeads® CD14. Step 2. Positive isolation of CD4+ T-cells with Dynabeads® CD4. Step 3. The lysis solution releases the nuclei for staining or automatic counting.*

2.3.6 Immunomagnetic Separation of CD4+ T-Cells from Unprocessed Whole Blood

CD4+ T-cells were isolated by a Dynal® T4 Quant kit following the given protocols. Briefly, 125 µL whole blood was incubated and rotated with 25 µL CD14-coated beads and 350 µL PBS pH 7.4 buffer for 10 min. After 10 minutes, the tube containing the solution was placed in the magnet for 2 minutes to hold the magnetic beads. Without disturbing the magnetic beads, 200 µL monocytes depleted blood (supernatant) was pipetted out and added to a tube with 25 µL of CD4-coated beads and 200 µL PBS pH 7.4 buffer, followed by another 10 min incubation and rotation. The tube was placed in the magnet again to hold the beads, all supernatant was discarded without disturbing the beads, the remaining beads were then washed three times with PBS pH 7.4 buffer.

2.3.7 Enumeration of CD4+ T-Cells with Hemocytometer

Isolated CD4+ T-cells were lysed by the lysis solution provided in the Dynal® T4 Quant kit. The lysed cells were stained with Sternheimer−Malbin solution for the conventional bright field microscope, or Acridine Orange for the fluorescence microscope. The solution was loaded on a hemocytometer, and the nuclei were counted.

2.3.8 Enumeration of CD4+ T-Cells with The "Pinwheel Assay"

After immunomagnetic separation, the isolated CD4+ T cells were incubated in 100 µL of 8 M GdnHCl solutions for 30 min, and the solution was further diluted 20, 40, 80, and 160-fold with 8 M GdnHCl. These four aliquots were then loaded into the pinwheel microwell following the same procedure as the calibration curve generation.

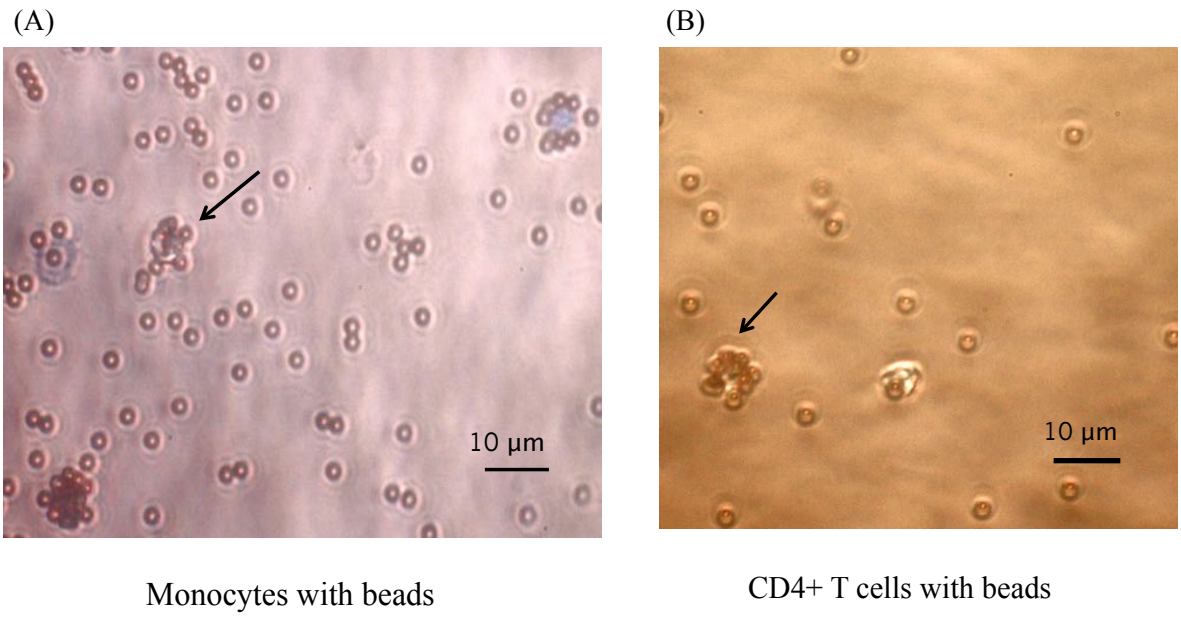

Figure 2-6. *Captured cells under microscope with 40x objective. (A) Monocytes targeted by anti-hCD14 coated magnetic beads (B) CD4+ T-cells targeted by anti-hCD4 coated magnetic beads.*

2.4 Results and Discussion

2.4.1 Dynal® T4 Quant Assay

The pinwheel effect is generic because the adsorption of DNA on silica is not specific to genomic sequence; hence, sub-typing of cells in a complex mixture is not possible without invoking the use of a "selective" step. Dynal® T4 Quant kit (Invitrogen) is a commercialized lymphocyte counting assay for the monitoring of immunodeficiency. It is designed for the determination of CD4+ lymphocyte counts directly from whole blood samples. This test exploits antiCD4+ coated magnetic beads for isolating CD4+ T-cells from blood. As mentioned in the introduction, some monocytes express the CD4 antigen, and therefore are the primary contaminant. Given that monocytes also express CD14 on their surface [15], antiCD14-coated magnetic beads are applied to deplete the sample of monocytes, prior to the capture of CD4+ T cells (**Figure 2-5**). This process can be visually detected under a light microscope with 40x objective, as indicated in **Figure 2-6**. In the protocol described by the manufacturer, the captured CD4+ T-cells are partially lysed so that their nuclei can be released and enumerated under a microscope after staining, this result is shown in **Figure 2-7**. To enumerate CD4+ T-cells, we need a light microscope

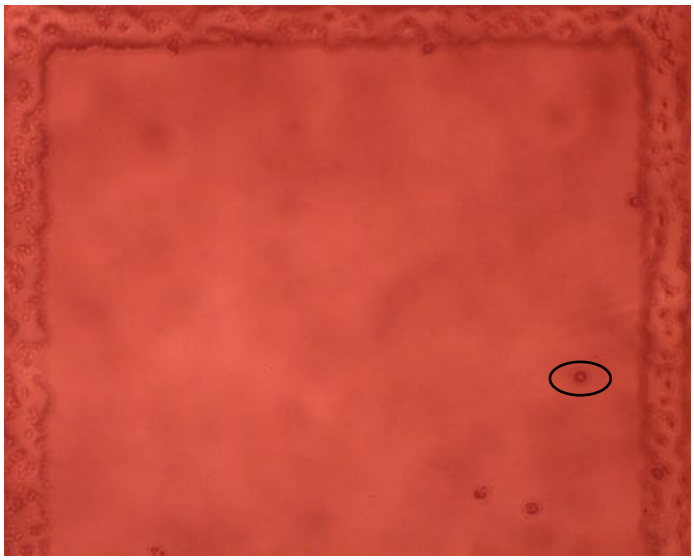

Figure 2-7*. Captured CD4+ T-cells lysed and the nuclei were stained by Sternheimer-Malbin. Circled is one of the stained nuclei. There are 7 nuclei n the field of vision.*

with at least 40x objectives, a hemocytometer and calibrated pipets. To manually count cells with hemocytometer is subjective, labor-intensive and the throughput is low. For example, it takes more than one hour when the CD4 count is more than 500 cells/mm^3 blood. On the other hand, if this assay is coupled with fluorescent microscopy, costly and unstable fluorescent reagents are involved. In either situation, the microscopy reading step is difficult to automate, making this method impractical for Point of Care (POC). To circumvent the microscopic counting of cells, we substituted this step with the pinwheel assay. We propose to develop an

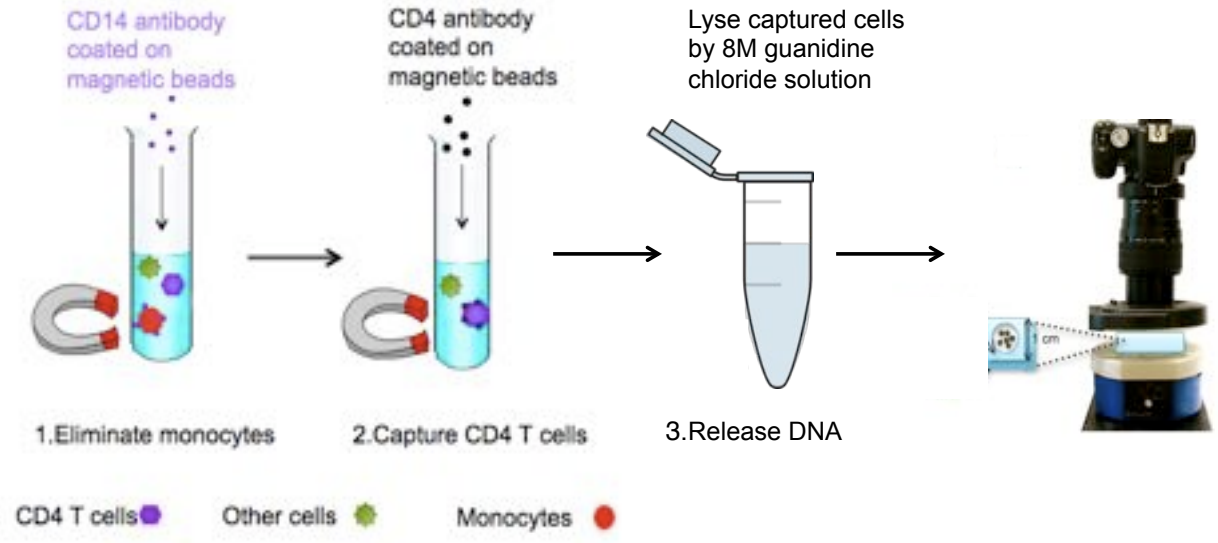

Figure 2-8. *Isolation and pinwheel procedure. Anti-hCD4 isolated CD4+ T-cells were lysed by 8M guanidinium chloride solution, and silica coated magnetic beads were introduced to induce DNA-bead aggregation. The formed aggregation were captured by a high resolution camera and analyzed by a simple algorithm.*

affordable, label-free method, integrating immunomagnetic separation by Dynal® T4 kit and the pinwheel assay, to enumerate CD4+ T-cells. With the pinwheel process, the isolated cells are completely lysed, and pinwheel aggregation is induced by the released DNA, allowing for quantification of cells. The stepwise procedure is illustrated in **Figure 2-8**.

Since the enumeration of CD4+ T-cells involves pre-assay isolation of the cells, the effectiveness of this process relies on efficient and consistent CD4+ T-cell isolation. The mean isolation yield was calculated by dividing the microscopic cell count by the flow cytometry count of the original sample, the yield was found to be 91.5 ± 4.3% based on four blood samples when the blood samples were drawn within 24 h (results shown in **Figure 2-9**). The product insert claims a 97% isolation efficiency [16], however the difference could be attributed to the

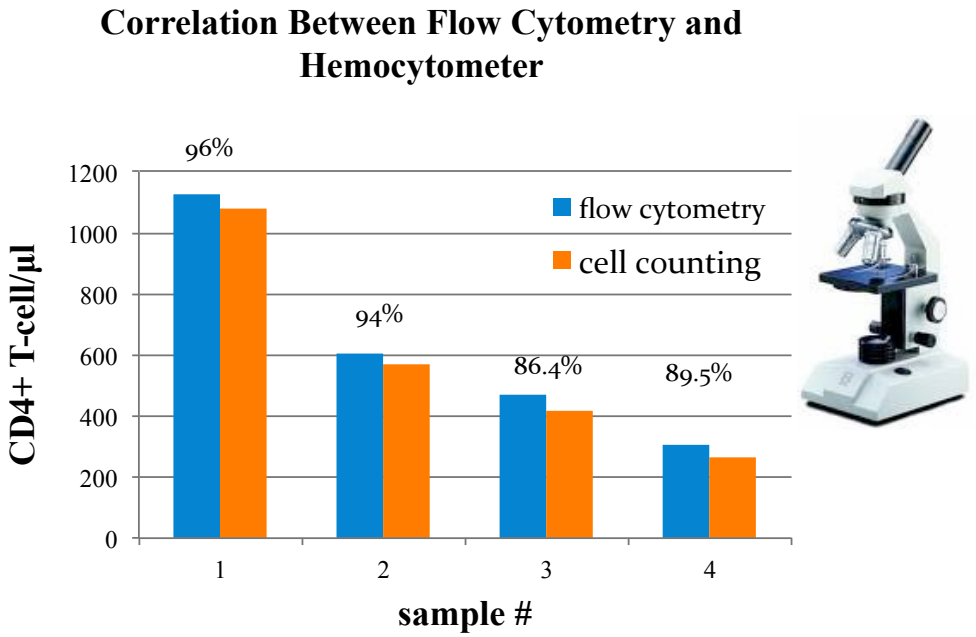

Figure 2-9. *CD4+ T-cells enumerated via hemocytometer under bright field microscope, the result was compared with flow cytometry to calculate the isolation efficiency.*

subjective nature of the microscopic counting.

The flow cytometry facility used BD FacsCaliber system (two color laser) to enumerate lymphocytes and specifically CD4+ T-cells. When whole blood is added to the reagent, the fluorochrome-labeled antibodies in the reagent bind specifically to leucocyte surface antigens.

During acquisition, the cells travel past the laser beam and scatter the laser light while the stained cells fluoresce. These scatter and fluorescence signals, detected by the instrument, provide information about the cell's size, internal complexity, and relative fluorescence intensity. The patient sample is incubated with a monoclonal antibody for the CD4 antigen on T-cells along with a monoclonal antibody for the CD3 antigen. This method is used to make sure the reaction is T-cell specific and not due to monocytes (which can give a positive CD4 response). To examine the purity of the Dynal® T4 quant kit isolated CD4+ T-cells, i.e., no monocytes contamination, we applied the same principle, using the BD CD3 Fitc,CD8 PE, CD45 PerCP, CD4 APC 4 color cocktail kit, to sandwich the cells with both CD3 and CD4 antibodies, and those CD3+/CD4+ cells are identified as CD4+ T-cells. Some of the kit's information is listed in Table 1, only CD3 and CD4 were used to evaluate the purity.

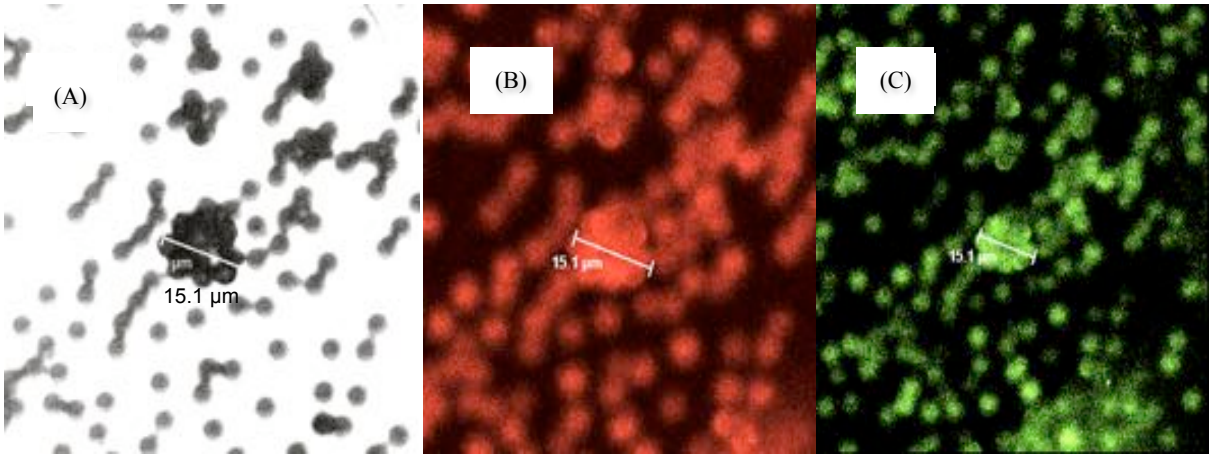

Figure 2-10. *Magnetic beads captured cells observed under confocal microscope. (A) Bright field (B) Alexa Fluor® 488 anti-hCD3 stained (C) PE-Alexa Fluor® 488 anti-hCD4 stained.*

Figure 2-10 shows one cell captured by magnetic beads, observed under a bright field microscope, fluorescence microscope at 488 nm excitation and 633 nm excitation, respectively. The central lump with a size measurement represents the cell while the other objects are the

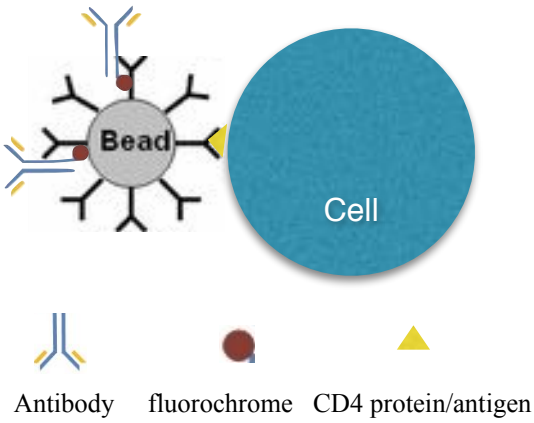

Figure 2-11. *Proposed cell - magnetic beads - fluorochrome conjugated antibody structure. The cell was first isolated by the anti-hCD4 coated magnetic beads, and then incubated with fluorochrome conjugated anti-hCD4. Since the antigen is already occupied by the magnetic beads, the fluorochrome-antibody conjugation bind to the antibody on magnetic beads instead, and resulted in the illumination of beads.*

excessive magnetic beads. First of all, a high laser power was necessary in order to observe any emission, and the magnetic beads fluoresce at the same intensity as the cell. Given this result, it is speculated that the fluorochrome-labeled monoclonal antibodies failed to bind to the specific cell surface. Instead they bind to the antibody coated magnetic beads surface. This is possible because 1) The CD4 antigens are already occupied by the anti-hCD4 coated magnetic beads. 2) The fluorochrome has high affinity to the antibody. The cocktail kit was intended to work with whole blood, not a magnetic-bead processed blood sample, and the interaction between the

antibody coated magnetic beads and the fluorochrome-labeled antibodies is unclear. **Figure 2-11** demonstrates the proposed cell - magnetic beads - fluorochrome conjugated antibody structure.

2.4.2 CD4+ T-Cells Calibration Curve

As mentioned in the introduction, the "pinwheel assay" is a novel approach that

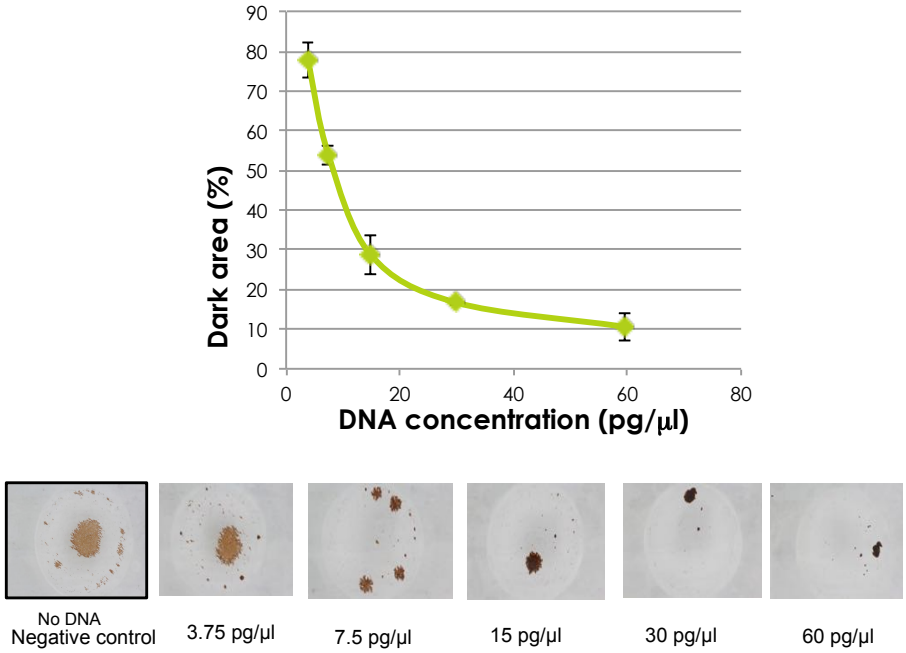

Figure 2-12. *CD4+ T cells calibration curve, Dark Area (DA) represents the pixels make up the brown area. Dark Area% is normalized over the negative control (no DNA).*

quantifies the amount of DNA in biological samples, based on the visually detectable interaction of DNA with silica-coated super-paramagnetic beads. This assay quantifies DNA according to the formed aggregation of silica-coated magnetic particles and DNA in the presence of a high

concentration of chaotrope under a rotating magnetic field (RMF). The dark area represents the degree to which the particles have aggregated, i.e., the pixels that make up the brown area, and the calculated dark area is then normalized against a negative control to get the % Dark Area (%DA). Images of the aggregate reveal a correlation between the size of the aggregate and DNA mass, a higher %DA signifies a lower concentration of DNA present in the well.

To generate the calibration curve for CD4+ T-cell counting, blood samples were drawn from HIV+ patients on the day of the analysis, and the CD4 counts were determined by flow cytometry. The blood samples were processed by the Dynal® T4 Quant kit to isolate CD4+ T-cells and the captured cells were then lysed with 8M GdnHCl and serially-diluted to appropriate concentrations. The diluted DNA was then mixed with ~16x10^4 (15.9±0.6x10^4) silica coated

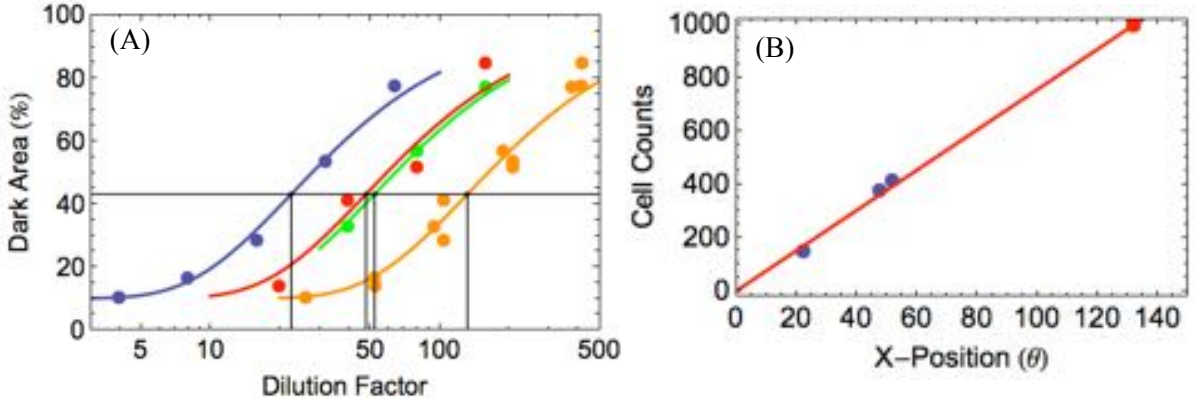

Figure 2-13. *Algorithm to convert dilution factor to CD4 counts. (A) At the same dark area %, samples with different CD4 count correlate to different dilution factor. (B) A standard curve was established correlating the flow cytometry cell counts versus dilution factor at certain dark area %.*

magnetic beads and exposed to the RMF for 5 min, and images were captured for analysis where a simple algorithm was used to first correlate the %DA with the DNA concentration. The cell

count was determined based on the hemocytometer result (isolated CD4+ T-cells stained and counted under microscope), then the DNA concentration was calculated given the fact that each somatic cell contains 6.25 pg of DNA [18] and the dilution factor. The correlation between %DA and CD4+ T-cell DNA is illustrated in **Figure 2-12**, which provides the calibration curve to determine the CD4+ T-cell count in blood samples.

To evaluate the ability of the pinwheel process to enumerate the CD4+ T-cells in unknown samples, dilution is necessary so that the dark area falls in the effective calibration range. By comparing the flow cytometry value with the calibration curve, the CD4 count can be estimated following dilution, which is then converted to the initial CD4 count by multiplying by the dilution factor. **Figure 2-13** shows the second algorithm that correlates the dilution %Dark Area to the cell count. When a line is drawn at the same % Dark Area, different blood samples with different CD4 counts correlate to distinct concentrations, which is inversely correlated to

Table 2-1. The BD Multitest™ CD3 FITC/ CD8 PE/CD45 PerCP/CD4 APC [17]

Content	50 tests, 1 ml			
Usage	20 µl per test			
Specificity	CD3	CD8	CD45	CD4
Clone	MEM-57	MEM-31	MEM-28	MEM-241
Isotype (mouse)	IgG2a	IgG2a	IgG1	IgG1
Fluorochrome	FITC	PE	PerCP	APC
λ. excitation	488 nm	488 nm	488 nm	633 nm
Emission maximum	525 nm	575 nm	670 nm	660 nm

dilution factor. The dilution factor at a certain % Dark Area is plotted versus flow cytometer CD4 count and this linear standard curve was used to enumerate CD4 T-cells.

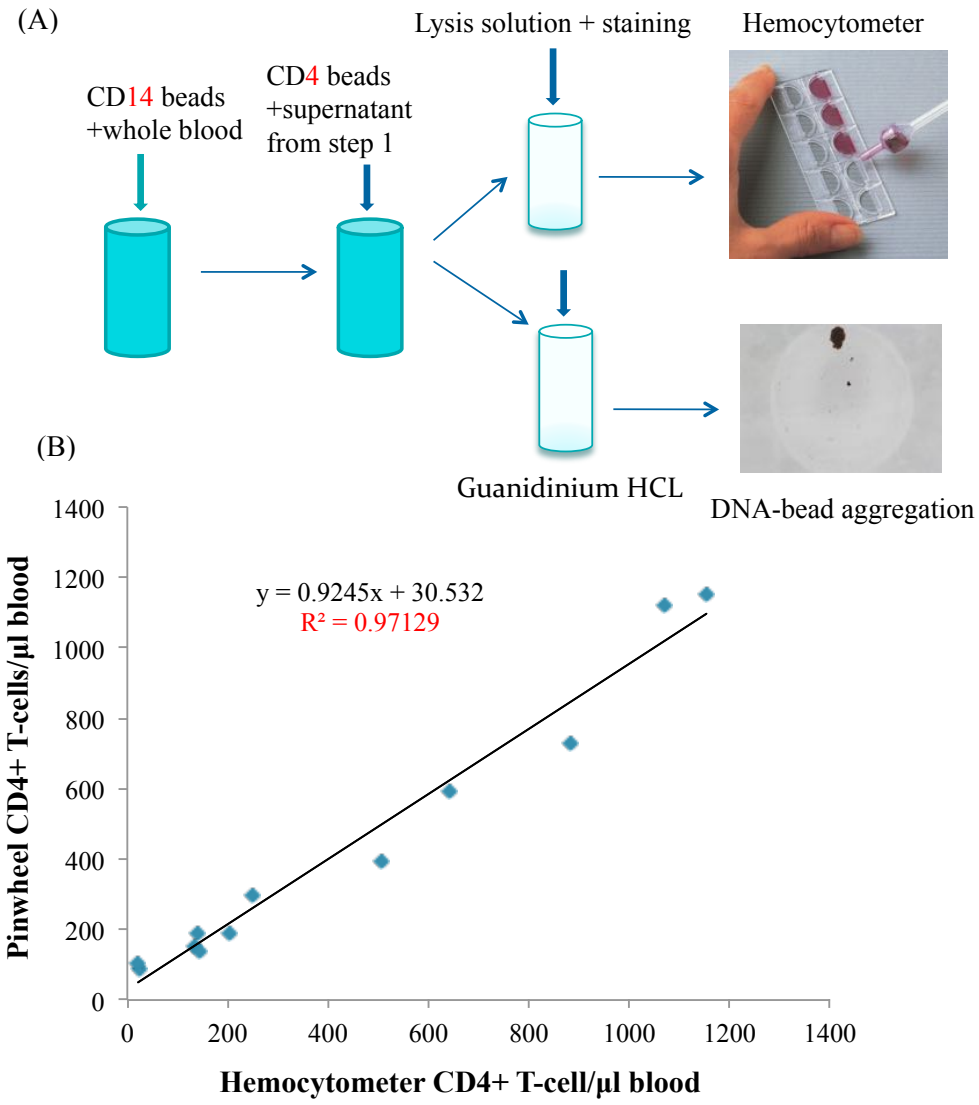

Figure 2-14. *Correlation between the pinwheel results and hemocytometer. (A). The isolated CD4+ T-cells from the same sample was divided into 2 aliquot and quantitated by 2 methods. (B) Data analysis shows strong correlation between these two methods (R^2=0.97). Sample CD4 count ranging from 2 to 1200 CD4 T cell/µl blood*

2.4.3 Counting CD4+ T-Cells with The 'Pinwheel Assay'

To evaluate the accuracy of the pinwheel assay, two aliquots of purified cells were acquired from each unknown sample, with one partially lysed for microscopy quantification and the other completely lysed for the pinwheel assay (**Figure 2-14A**). Comparison shows a good correlation between the two methods with 13 patient blood samples (R^2=0.97 as shown in **Figure 2-14B**), which suggests that the pinwheel assay can, indeed, enumerate the isolated cells accurately. Our method reduces per sample analysis time 6 fold (from more than an hour to 10 minutes). Moreover, it is feasible to integrate pinwheel quantitation into a portable and automated microdevice as enumeration requires only a camera to capture an image and a mathematica algorithm to convert this into a cell count.

In the clinical setting, CD4+ T-cell count can be indicative of the immune status of a patient. When the CD4+ T-cell count is lower, along with other factors, it can represent the progress of HIV infection; when the count is higher, it can indicate recovery from immunodeficiency through decreased viral load. The pinwheel CD4+ levels in 21 blood samples following immunomagnetic separation were compared with the results from flow cytometry (**Figure 2-15** A,C). The collective data is from two sample groups from two sources (8 samples analyzed same day as blood draw; 13 samples analyzed >24 h after blood draw). A good correlation was observed between the immunocapture−pinwheel assay and flow cytometry, when the samples were analyzed within 24 h of the blood draw (**Figure 2-15** A,B). Dramatically poorer correlation between the pinwheel and flow cytometry methods was observed with samples analyzed more than 24 h postdraw (**Figure 2-15** C). This observation is consistent with the observation by Diagbouga et al. that 31%−69% of blood samples exhibit more than a 20%

decrease of CD4 count after a 24 h delay [19], which directly affects the accuracy of the pinwheel assay.

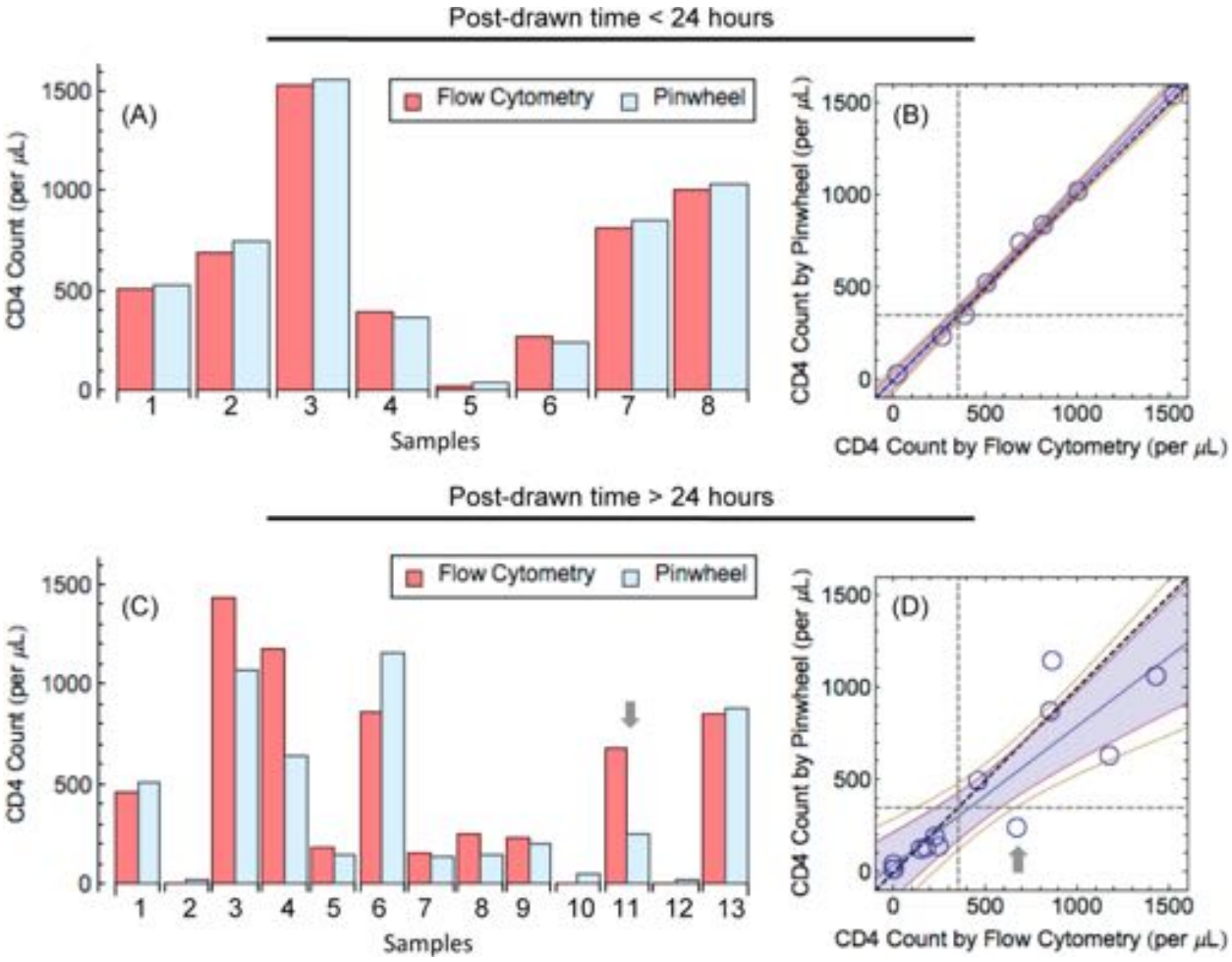

Figure 2-15. *Quantification of CD4+ T cells. The pinwheel result correlates well with flow cytometry when the post-drawn time of blood is less than 24 h, as shown in (A) and (B). For the samples with post-drawn time over 24 h, the accuracy of the pinwheel assay is compromised due to the deterioration of sample quality, as shown in (C) and (D). The solid blue lines in (B) and (D) represent linear calibration functions, and the black dashed lines show y = x. The gray dashed lines represent the threshold (350 cells per μL) that defines the starting time of ARV for HIV patients (for (B), $R^2 = 0.997$; for (D), $R^2 = 0.775$). The arrows in (C) and (D) point to the only sample that generated a false result in the pinwheel assay.*

assessing

For HIV-infected patients, initiation of ART is determined by a CD4+ T-cell count that

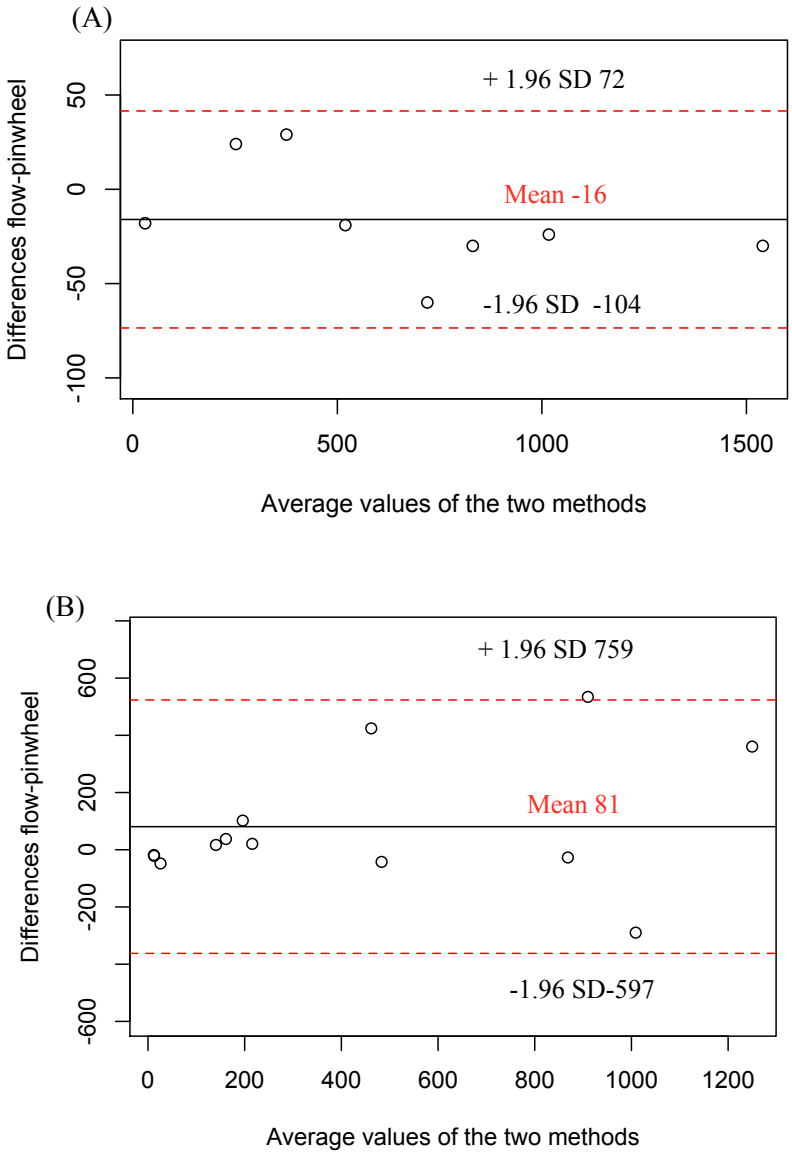

Figure 2-16. *Bland-Altman plots. (A) Blood samples <24 hours (B) Blood samples >24 hours. With fresh blood samples, the flow cytometry results are slightly lower than the pinwheel results (-16), with aged samples, the flow cytometry results are higher than the pinwheel results(+81).*

drops below 500 cells/μL. What we have demonstrated here is that, with the 21 whole blood

samples evaluated from HIV patients, the pinwheel assay correctly categorized those determined by flow cytometry to be above or below the 500 cells/μL cut off. Only one sample (one from the >24 h storage time group) was categorized as false positive, and this point is labeled with a gray arrow in **Figure 2-15D**. Despite the asynchrony in the storage history of these samples, this still represents a >95% correlation between the immunocapture−pinwheel assay and flow cytometry. This is remarkable and points to the obvious merit of a method that does not require fluorescent reagents, microscopy, or cytometry counting.

One of the main advantages of the pinwheel assay is that it does not require fluorescent labels and complex optics or expensive instrumentation to enumerate cells. Fluorescence provides accurate and sensitive quantification of analytes in various applications, but the labels are often subject to photobleaching, resulting in unstable optical properties, which increases the cost for reagent storage and induces the need for repetitive calibration. By avoiding fluorescent labels, the pinwheel assay offers enhanced simplicity and cost-effectiveness compared to conventional techniques, which are always desired when applying a new technique in resource-limited regions. One of the major drawbacks of the pinwheel assay is that the cells are lysed after counting, and thus will not be available to other cell analyses, which may be problematic if sample availability is limited. Day-to-day variability with the pinwheel method was low, a likely result of the simplicity of the method. User-to-user variability is more likely to be significant, but this can be overcome by building a larger database for calibration of the assay independent of the user.

Evaluation of the data by the Bland-Altman method is given in **Figures 2-16,** The pinwheel assay showed a positive bias of 16 cells/μL over flow cytometry results (flow-

pinwheel=-16, i.e., on average, the pinwheel results are 16 cells more compared to the flow cytometry result), and 95% limits of agreement of 72 cells/μL and -104 cells/μL with samples analyzed in <24 hours post-draw. Samples >24 hours post-draw analyzed by the "pinwheel assay" showed a negative bias of 81 cells/μL (flow-pinwheel=81), and 95% limits of agreement of 759 cells/μL and -597 cells/μL. This result is consistent with the theory that the aged samples are poor target of immuno-capture, and aged samples usually lead to lower cell count. With the new ART initiation threshold of 500 cells/μL, the pinwheel assay correctly categorized all those (samples <24 hours) determined by flow cytometry to be eligible for the ART.

2.5 Concluding Remarks

In conclusion, we have extended the application of the pinwheel assay from nucleic acid quantification to cell counting, and demonstrated isolation and enumeration of a specific subtype of cells from a mixture (CD4+ T cells). While we have a simple methodology for generic cell counting, specificity was brought to the method by coupling with immunocapture. This example shows the versatility of the pinwheel assay (i.e., that the assay has the potential to be applied in various fields). As the aggregation of magnetic particles only requires microliter volume of samples and a digital camera as the detection modality, the pinwheel assay could serve as a portable and cost-effective alternative to conventional technologies for point-of-care applications.

We are working on integrating all of these processes on a single microfluidic device to minimize hands-on operation and user-to-user variability. This is essential for progressing toward a cell counting device with sample-in-answer-out capability (detailed in Chapter 3).

Successful employment of the pinwheel assay in an integrated microfluidic system will not only benefit basic biomedical research but also offer capability to a wide range of clinical applications.

2.6 References

1. Christine Bourgeois *et al*. Review CD4 T cells are required for CD8 T cell memory generation. ***European Journal of Immunology***. 2003, 12,3225-3231.
2. WHO CD4+ T Cell Enumeration Technologies; Technical Information. GENEVA: World Health Organization , 2008.
3. Aina, o. *et al* Reference values of CD4 T lymphocytes in human immunodeficiency virus-negative adult Nigerians. ***Clin. Diagn. Lab Immunol***. 2005, 12,525-530.
4. UNAIDS, Global report: UNAIDS report on the global AIDS epidemic 2013, UNAIDS/ JC2502/1/E, WHO, Geneva, 2013.
5. WHO Technical Brief on CD4 Technologies, WHO, 2010.
6. "In 2008, the overall median price of commonly used drug regimens for all countries with Global Fund programs was US$ 188 (IQR: US$ 171 – $US 209). The median price increased with national income level." Global Fund, "Innovation and Impact (2010)".
7. Glencross D, Scott LE, Jani IV, Barnett D, Janossy G. CD45-assisted PanLeucogating for accurate, cost-effective dual-platform CD4+ T-cells enumeration. ***Cytometry*** 2002, 50: 69–77.

8. Glencross D, Scott LE, Jani IV, Barnett D, Janossy G. CD45-assisted PanLeucogating for accurate, cost-effective dual-platform CD4+ T-cells enumeration. ***Cytometry*** 2002, 50: 69–77.

9. Jani, I. *et al*. Effect of point-of-care CD4 cell count tests on retention of patients and rates of antiretroviral therapy initiation in primary health clinics: an observational cohort study. ***Lancet***, 2011, 378(9802), 1572–9.

10. Janossy G, Jani IV, Bradley NJ, Bikoue A, Pitfield T Affordable CD4+ -T-cell counting by flow cytometry: CD45 gating for volumetric analysis. ***Clin Diagn Lab Immunol*** 2002, 9, 1085–1094.

11. Melzak, K. A., Sherwood, C. S., Turner, R. F. B., & Haynes, C. A. Driving forces for DNA adsorption to silica in perchlorate solutions. ***J Colloid Interface Sci,*** 1996, 181(2), 635–644.

12. Leslie, D. C., Li, J *et al*. New detection modality for label-free quantification of DNA in biological samples via superparamagnetic bead aggregation. ***J Am Chem Soc, 2012***, 134(12), 5689–5696.

13. Li, J., Leslie, D. C., Haverstick, D. M., Kelly, K. a, Barker, N. S., & Landers, J. P. Pinwheel Assay : a Visual and Label-Free Method for Dna. Analysis, 2010, (October), 61–63.

14. Li, J., Liu, Q. *et al*. Label-free method for cell counting in crude biological samples via paramagnetic bead aggregation. ***Analytical Chemistry***, 2013, 85(23), 11233–9.

15. Kazazi, F., Mathijs, J.-M., Foley, P., & Cunningham, a. L. Variations in CD4 Expression by Human Monocytes and Macrophages and Their Relationship to Infection with the

Human Immunodeficiency Virus. ***Journal of General Virology***, 1989, 70(10), 2661–2672.

16. Dynal, T., & Kit, Q. (n.d.). Product Information, 3–4.
17. Jose, S. (n.d.). BD Multitest TM PerCP / CD4 APC Reagent, (340499).
18. Butler, J. M. Forensic DNA typing: Biology, Technology, and Genetics of STR Markers, 2nd ed.; ***Elsevier Academic Press***: Burlington, MA, 2005.
19. Diagbouga, S. Chazallon, C. Kazatchkine, M. D. Van de Perre, P. Inwoley, A. M'Boup, S. David, M. P. Tenin, A. T. Soudre, R. Aboulker, J. Weiss, L. ***AIDS*** 2003, 17 (15), 2201−2208.
20. Nelson, D. a., Strachan, B. C., Sloane, H. S., Li, J., & Landers, J. P. Dual-force aggregation of magnetic particles enhances label-free quantification of DNA at the sub-single cell level. ***Analytica Chimica Acta***, 2014, 819, 34–41.
21. Ouyang, Y., Li, J., & Landers, J. P. Integration of Pinwheel Assay on a Cd-Like Microchip for Dna Quantitation, (October), 2013,1613–1615.

Chapter 3. The ARTμS: An Integrated Microfluidic CD4+ T-cells Enumeration System for Monitoring Antiretroviral Therapy in HIV Patients

3.1 Overview

We report on a novel, cost-effective, and label-free microfluidic platform that integrates immunomagnetic separation and cell enumeration via DNA-induced bead aggregation. Using a two-stage immunocapture microdevice, a total of 10 μL of whole blood was processed on chip. The first stage involves the immuno-subtraction of monocytes by anti-CD14 magnetic beads, followed by CD4+ T-cells capture with anti-CD4 magnetic beads. The super hydrophilic surface generated during PDMS plasma treatment allowed for accurate metering of the CD4+ T-cells lysate, which then interacted with silica-coated magnetic beads under chaotropic conditions to form aggregates. Images of the resulting aggregates were captured and processed to reveal the mass of DNA, which was used to back-calculate the CD4+ T-cells number. Studies with clinical samples revealed that the analysis of blood within 24 hours of phlebotomy yielded the best results. Under these conditions, an accurate cell count was achieved (R^2=0.98) when compared to cell enumeration via flow cytometry, and over a functional dynamic range from 106-2337 cells/μL.

3.2 Introduction

In 2012, 9.7 million people in low and middle-income countries received antiretroviral therapy, representing 61% of those eligible under the 2010 WHO HIV treatment guidelines. The Joint United Nations Program on HIV/ Acquired Immune Deficiency Syndrome (UNAIDS) aimed to treat 15 million people currently living with HIV with antiretroviral treatment by 2015 [1]. It was proven that point-of-care (POC) CD4 devices can increase the number of people receiving treatment, as well as the effectiveness of the treatment due to earlier diagnosis and t ability to seek to follow up care. A recent study has shown that after the introduction of a point-of-care CD4 device in Mozambique, the total loss to follow-up before initiation of ART dropped from 64% to 33%, and the enrolled patients for ART increased from 12% to 22% [2].

Effort has been exerted to define an affordable, less complicated alternative to standard flow cytometry. Some single-purpose flow cytometers have been specially designed for CD4 counting, such as the Becton Dickinson FACSCount™ and Guava Easy CD4™. While the instruments themselves are available at a reduced cost, the reagent cost remains high, the fluorescent reagent involved is still difficult to store and transport, and the technical skill requirement is still high [3]. Non-flow cytometer alternatives have also been developed and recently reviewed [4]. Here we will focus on the microfluidic devices developed specifically for CD4 enumeration.

In 2007, Cheng *et al* introduced a CD4+ T-cells counting device, based on cell affinity chromatography, operated under controlled shear stress. The CD4+ T-cells were captured by anti-hCD4 antibodies anchored on the microdevice, and labeled by a fluorescence tag, the captured cells were counted by fluorescence microscope, after monocytes were partially

eliminated by applying optimized sheer stress to the cells. Although effective, this method only

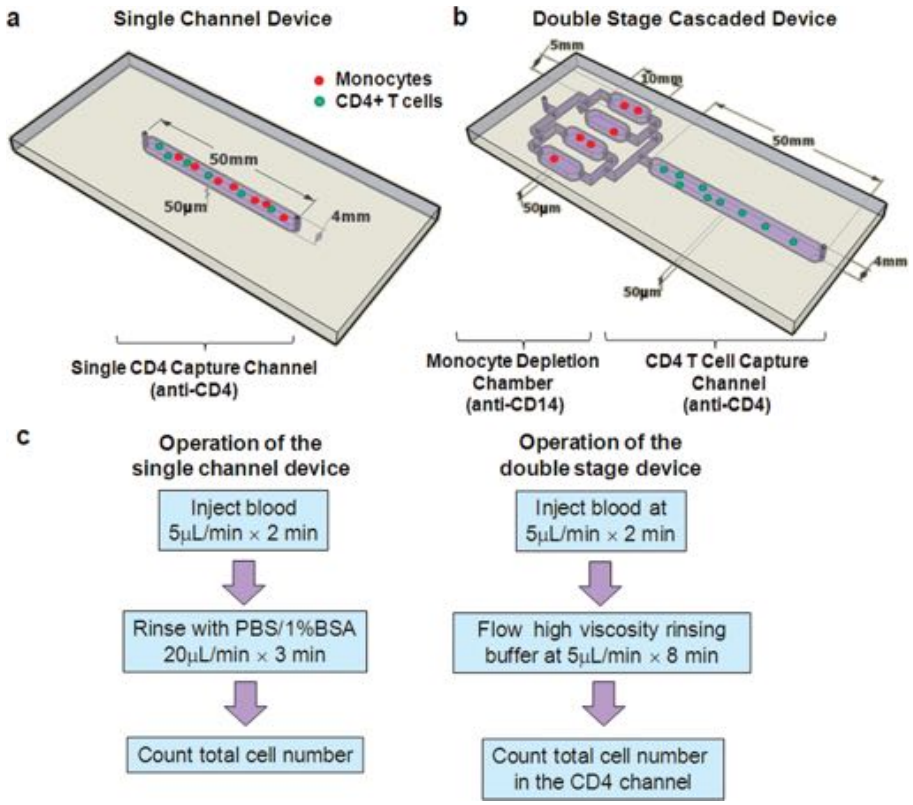

Figure 3-1. *Single and double-stage microfluidic devices [5,6]. Schematics showing the geometry of the single channel (a) and two stage (b) devices. The CD4+ T cell capture channels of both devices were functionalized with an anti-hCD4 antibody for target cell isolation. The two stage device also contains 4 parallel chambers upstream to the CD4 channel for monocyte depletion. (c) The operation procedures of the two counting devices. For the double-stage devices, two considerations were taken into account for the rinsing buffers: one is to quickly displace monocyte depleted blood to the CD4 capture channel and the second is to avoid shearing off specifically captured cells. Taken from [6]*

achieved a correlation of R^2=0.93 when comparing to flow cytometry [5]. Cheng *et al* later

demonstrated increased device performance (R^2=0.98), by introducing an additional domain that,

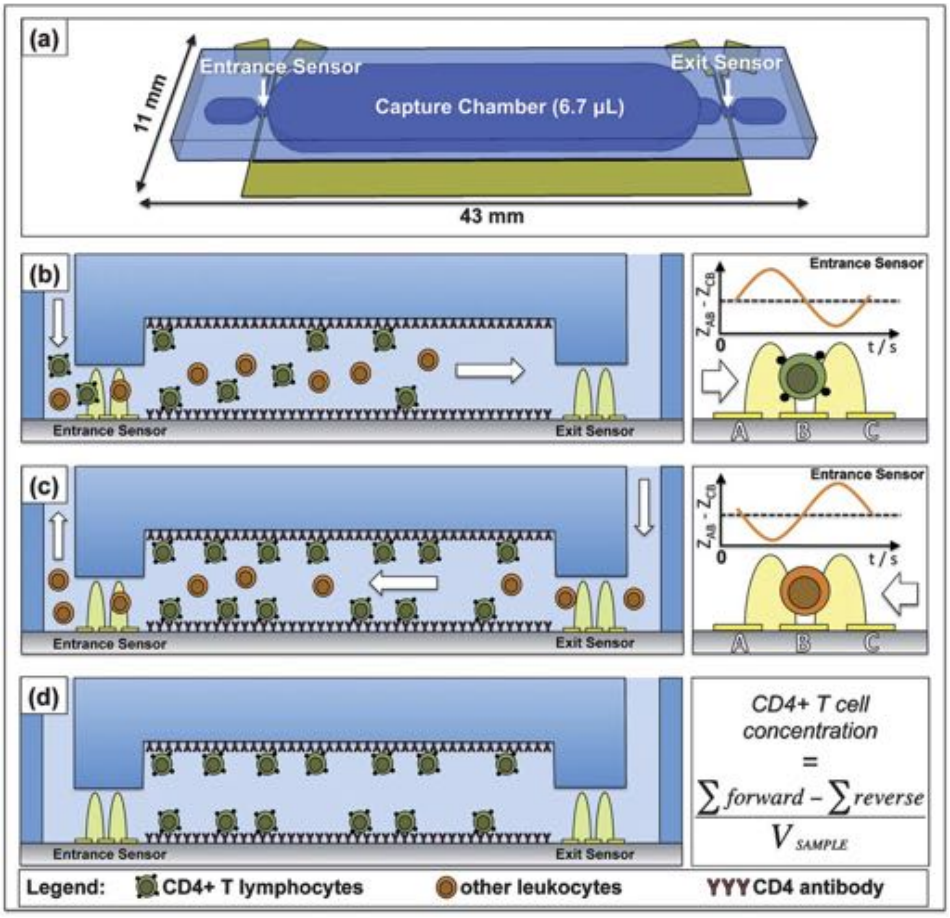

Figure 3-2. *Principle of electrical differential counting of CD4+ T cells [12]. (a) chip's geometry, specifically its two electrical counters and capture chamber. (b) forward flow direction to obtain total leukocyte count at the entrance counter, (c) reverse flow direction and enumeration of uncaptured cells after leukocytes reach the exit sensor, and (d) finished experiment after all unbound leukocytes are washed from the capture chamber. The concentration of CD4+ cells can be obtained simply by normalizing the differential count by the known sample volume ((d), right panel). The right panels of (b) and (c) illustrate how cell flow direction at the entrance counter can be determined by the change in pulse signature polarity, with the pulse signature changing from up-down (b) to down-up (c) in time. Taken from [13].*

eliminated monocytes using CD14+ antibodies (device shown in **Figure 3-1 B** [6]).

CD4+ T-cells imaging using fluorescence and quantum dots have been elegantly demonstrated in many studies[7-10]. Wang *et al* developed a device using chemiluminescence as the detection mode[11], and this method avoided using high cost and sensitive fluorescence reagents. With this approach, cells are first captured by a CD4 antibody, then sandwiched by a second CD3 antibody, which is attached to an enzyme that induces chemiluminescence, only cells attached to both CD3 and CD4 will stay in the microdevice and be illuminated. The generated luminescence is detected by a silicon photo detector and converted to a photocurrent, the current detected is proportional to the number of captured CD4+ T-cells. Nicholas et al. developed an impedance CD4 microchip [12], based on the same principle as the Coulter counter. A Coulter counters detect cell sizes via measurement of current resistance change; an impedance pulse is generated every time a cell passes through the aperture [13]. In the microdevice, the impedance pulses at the entrance count all particles, while pulses at the outlet (entrance once reversing the flow direction) count only those not captured (non-CD4 cells), the subsequent difference represents the CD4 count (**Figure 3-2**). Mechanical sensors have been developed by functionalizing a quartz crystal sensor with anti-CD4 and, as CD4 T cells bind, the mass of the quartz crystal is increased, thereby changing its resonance frequency, and the change can be correlated to a CD4 count [14]. Other proposed cell counting techniques include the bead sedimentation system, commercialized under Zyomyx Inc. CD4 cells are first isolated by anti-

CD4 coated magnetic beads prior to bead focusing in a capillary tube; the height of the beads is

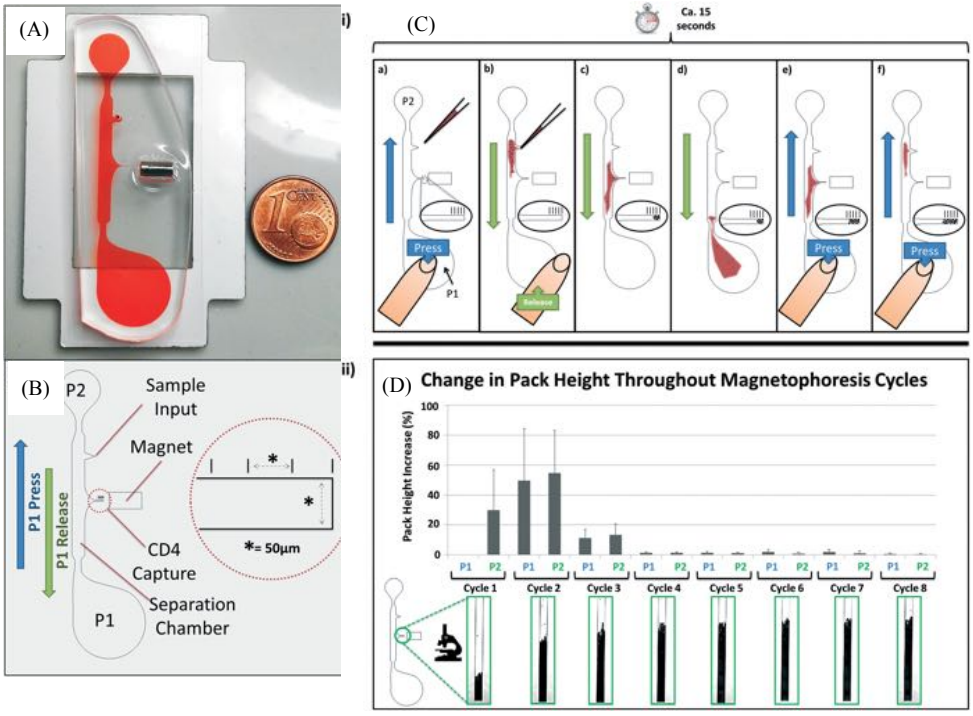

Figure 3-3. *Finger-press actuated magnetophoretic CD4+ isolation chip [16]. (A) Image of the chip. The microfluidic structures are highlighted with red dye. (B) Schematic showing main constituents. Direction of flow when P1 is depressed or released is indicated with blue and green arrows, respectively. A zoom of the capture chamber is shown in the circular red insert. Operation of one cycle to isolate CD4+ cells (shown as black circles) from whole blood. Direction of flow pressure is shown with blue (towards P2) and green (towards P1) arrows. Elliptical insert represents a zoomed view of the capture chamber. ii) Analysis of the heights of the cell/bead pack in the capture chamber from 1–8 cycles. "P1" (blue) and "P2" (Green) indicate the direction of the fluidic force. Images bordered in green represent zoomed micrographs of the capture chamber at the completion of a cycle. Taken from [16]*

correlated to the cell count [15]. Macdara et al. have recently developed a portable, finger driven device with a similar concept of bead sedimentation [16], as shown in **Figure 3-3**, however, the

draw back is that the beads height is read under a microscope. **Figure 3-4** shows a schematic of the Burnet assay, a semi-quantitative immuno-chromatographic strip. In this lateral flow device, the CD4 T-cells are captured by biotin-labeled anti-hCD4, which is then detected by a colloidal gold-labeled anti-biotin. The reference strip was coated with a biotinylated surrogate protein

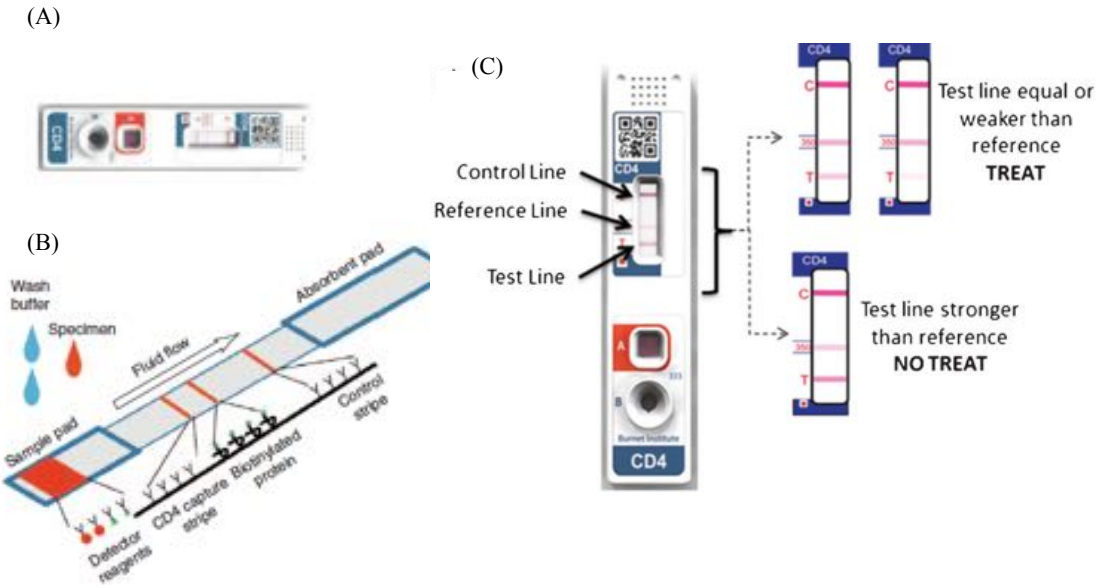

Figure 3-4. *Analyzer-independent CD4 counting devices. (A) The Burnet Institute CD4 test immunochromatographic strip (ICS); actual device (B) schematic (bottom). The ICS consists of three major component parts: a sample pad (containing labeled detector analytes, red blood cell and monocyte capture reagents, and cell lysis reagents), a nitrocellulose chromatographic strip with an anti-hCD4 capture strip, a comparator strip (a precise deposition of biotinylated protein relating to a given number of CD4 cells) and a control strip that captures excess detector reagent to indicate fluidic flow and binding of the detector reagent. The flow rate is optimized by an absorbent pad at the terminal end of the ICS. The flow of detector analyte is initiated by the addition of a wash buffer after the addition of the blood specimen. (C) The semi-quantitative test result is obtained by comparing the band intensity developed on the capture strip (T) to the adjacent reference strip located to the right. Taken from [34]*

marker for comparison of the sample to a reference, two visible bands appear on the strip, and the eligibility for ART was determined by naked eye to be either stronger or lighter than the reference strip. Given that this device is semi-quantitative, it is not useful to determine the efficacy of ART [34]. Other commercialized CD4 counting systems includes the MBio CD4 system [17], and the Daktari CD4 Counter [18-19], the later system is unique because it lyses the isolated CD4 T-cells while all other methods enumerate intact CD4 T-cell. This device is based on 1) microfluidic cell chromatography and 2) lysate impedance spectroscopy. Together, these technologies enable the instrument to deliver a CD4+ cell count without the requirement for fluorescence labelling of the cells.

In summary, the main difference among various CD4+ T-cells counting microdevices is the detection mode, including fluorescence, quantum dot, chemiluminescence, impedance, mechanical sensor, etc. The upstream isolation steps are mostly achieved by immunocapture via anti-hCD4. In order to get pure CD4+ T-cells, one can either eliminate monocytes first by using CD14 antibodies, then capture CD4 T-cells by anti-hCD4, or, given that only CD4 T-cells express both CD4 and CD3 proteins, one can sandwich the cell with CD4 and CD3 antibodies. Sheer stress was used to differentiate monocytes from CD4 T-cell in some cases, however, at low cell count ranges, contaminating CD4+ monocytes often offset the total cell counts, limiting the accuracy of the microchip.

Over the last few years, we have been reporting on the ‘pinwheel effect’, a phenomenon that involves the quantitative chaotropic-driven adsorption of DNA onto paramagnetic silica in a rotating magnetic field, and its application to DNA quantitation and cell enumeration [20-23]. Simple image analysis of the induced bead−DNA aggregation allows for direct quantification of

DNA in crude biological samples. Here, we report on the **A**utomated **R**esult for **T**-cell counting **μ**fluidic **S**ystem (ARTμS), a microfluidic device that quantitates CD4+ T-cells based solely on DNA content, through integration of a two-step immunomagnetic separation, on-board metering, and the pinwheel assay. The analysis of blood from HIV- or non-infected patients shows a strong correlation (R^2=0.98) in a wide dynamic range with the values generated by the flow cytometer.

3.3 Materials and Experimental Methods

3.3.1 Materials and Instruments

Sylgard® 184 silicone elastomer base. Sylgard® 184 silicone elastomer curing agent. HydroPhil™ from Lotus Leaf Coatings, SU8-2150, KOVA® GLASSTIC® SLIDE 10 with grids . 6M guanidinium chloride pH 6.1. Dynabeads® CD14 2x concentrated. Dynal® Dynabeads® CD4 5x diluted. Isotonic PBS buffer ph 7.4 with 1% BSA and .02% sodium azide. MagneSil® Paramagnetic particles. Corning glass slides 75x50 mm thickness of .96 to 1.06 mm. Light mineral oil. Harrick Plasma cleaner/sterilizer PDC-32G. Cannon Rebel T1i high resolution camera. Versa CO2 laser cutter. Dynabeads® CD4 and Dynabeads® CD14 are uniform, superparamagnetic beads (4.5 μm diameter) coated with a primary monoclonal antibody specific for the CD14 and CD4 membrane antigen mainly expressed mainly on human monocytes.

3.3.2 Chip Fabrication

Both layers were created from a 10:1 ratio of PDMS monomer to curing agent and cured for 10 minutes at 115°C. The first layer is designed with a 20μL well for monocytes trapping, connected with a 120μL well designed for CD4 T-cell isolation and lysis. The second layer was

laser ablated with a Versa CO_2 laser cutter from a sheet of cured PDMS. The second layer consists of 5 separate wells and 4 channels of varying lengths, the ablated channels face the glass layer. The layers were bonded by treatment of air plasma oxidizer.

3.3.3 CD4+ T-cells Isolation and Lysing

The microdevice was prepared by introducing 120 μL of 5x diluted Dynabeads® CD4 to the CD4 chamber. The beads were maintained in the chamber via a manifold embedded with magnets, while the buffer solution was removed. 10 μL of unprocessed whole blood and 6 μL of Dynabeads® CD14 2x concentrated were introduced to the small 20 μL chamber. The chip was mixed via rotation at 6 RPM for 10 minutes before the fluid was pushed into the large 120μL chamber together with 80 μL of PBS buffer, while maintaining the captured monocytes in the small chamber via applied magnets. The fluid was then mixed with the CD4+ coated beads for 10 minutes before all fluid was removed from the chamber while maintaining the beads with CD4+ T cells in the chamber. 3-5 aliquots of 120 μL PBS buffer were used to rinse the chamber in order to remove any red blood cells or unwanted white blood cells. The CD14 beads with captured monocytes were removed from the chamber. The cells were then lysed by adding 120 μL guanidinium HCL to the large chamber and mixing for 10 minutes. The lysate was then metered through the micro channels.

3.3.4 Pinwheel Assay and Data Analysis

Paramagnetic silica beads were added into each well to make up to a total volume of 20 μL each well, including a negative control containing only beads. The chip was placed in an

oscillating magnetic field at 210 RPM for 3 minutes, 20 seconds in each direction (Figure 4). An algorithm was developed to correlate the %DA in each well to generate a calibration curve, and from the calibration curve to the CD4+ cell count, please refer to previous publications for the algorithm details [20-23].

3.3.5 Flow Cytometry Analysis

To evaluate the accuracy of the cell counts obtained from the microfluidic chip, a portion of the samples were also analyzed by standard flow cytometry to quantify the CD4+ T-cells. The CD4+ T-cells counts obtained from the developed algorithm were compared to the results obtained from the flow cytometry and accuracy was evaluated based on a 1:1 ratio.

3.3.6 Super-hydrophilic Coating on PDMS

The selected super hydrophilic coating was HydroPhil™ obtained from Lotus Leaf Coatings. The PDMS was pre-treated with 5% 3-Aminopropyltrimethoxysilane (APTMS) in ethanol by submersion for 5 seconds, followed by a rinse with diH_2O and allowed to dry completely. Following the pretreatment, the PDMS was treated with the HydroPhil™ by three different methods: application with a swab, pouring the HydroPhil™ over the surface and allowing it to run off, and completely submerging the PDMS into the HydroPhil™ for 5 seconds. After each treatment method, the PDMS was allowed to completely dry exposed to air. 5 μL of deionized water was used to test the contact angle.

3.4 Results and Discussion

3.4.1 On Chip CD4+ T-Cells Isolation

The device design is shown in **Figure 3-5**, and it consists of two domains - one for immunocapture and one for detection/cell counting. The immunocapture domain has two stages,

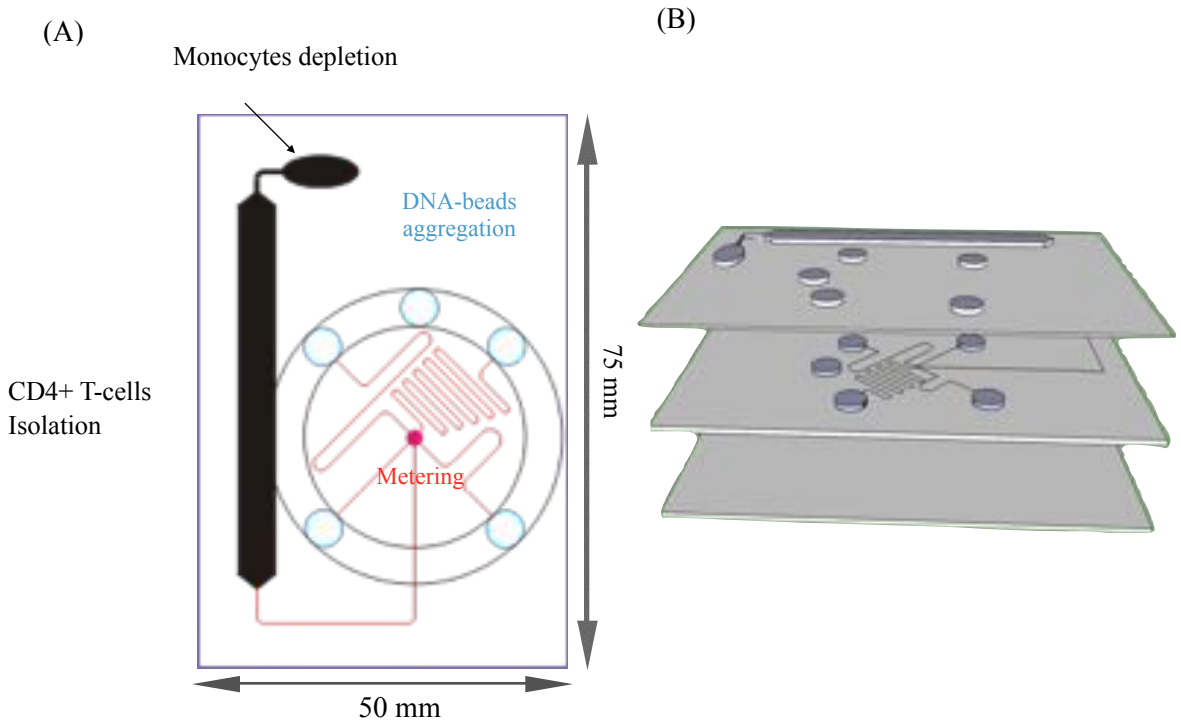

Figure 3-5. *CD4+ T-cells counting chip design. (A) The microchip contains two domains: an immunocapture domain (black) and a DNA quantitation-cell counting domain (blue), connected by the metering region (red). The immunocapture domain consists of 2 chambers, for monocytes depletion and CD4+ T-cells isolation respectively. The isolated CD4+ T-cells were lysed in the same chamber, and the lysate were pumped into the metering region. The DNA quantitation-cell counting domain include 4 wells for metered cell lysate, and 1 for negative control (solely magnetic beads). (B) Side view. The device is fabricated using two layers of Polydimethylsiloxane (PDMS) and one layer of glass.*

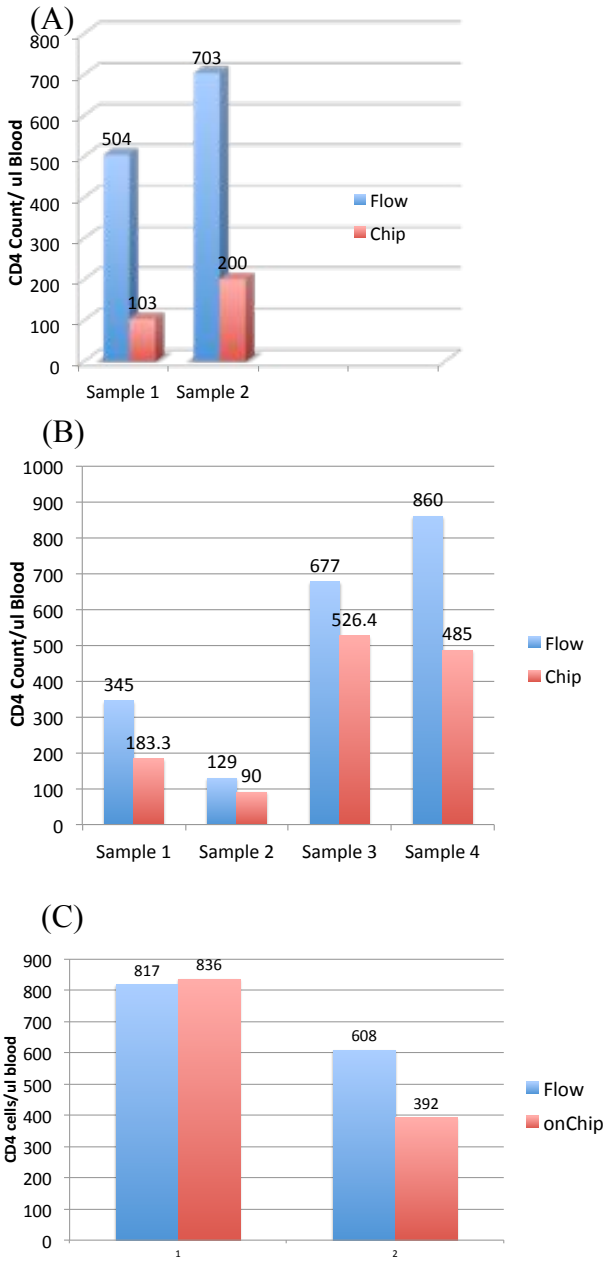

Figure 3-6. *Optimization of the on chip isolation process. The two chambers are coated by anti-hCD14 and anti-hCD4. (A) Use syringe pump to pump PBS buffer and capture CD4+ T-cells. Flow rate= 30 µl/min, it takes at least 50min to clean the chamber, and the isolation efficiency is low. Lower flow rate may enhance the efficiency but the it will be too time consuming (B) Pipette in buffers stead of Syringe pump, Mixing was achieved by manually manipulating magnet to capture cells. 5 min CD14, 10 min CD4. The optimal results were achieved by loading the chip on a lab tube rotator to enhance mixing,10 minutes each chamber. (C) Load the chip on the lab tube rotator for 5 minutes each chamber, the results are not reproducible, indicating 10 minutes are the minimum required to have reproducible isolation efficiency.*

one for immuno-subtraction of monocytes, and a second chamber for selective immunocapture of CD4+ T-cells. The Dynabeads® T4 quant kit was used to isolate CD4+ T-cells from 10 µL of unprocessed whole blood, and the isolation procedure was optimized based on the kit instructions and previous experiments [23]. The Dynabeads® are uniform, super-paramagnetic

polystyrene beads with a diameter of 4.5 μm, coated with mouse monoclonal antibodies against CD14 or CD4 antigens, allowing for specific capture of monocytes and CD4+ T-cells, respectively. A small fraction of monocytes may express the CD4 antigen in addition to CD14, therefore a high efficiency monocyte depletion step is critical to ensuring accurate CD4+ T-cells counts, especially when counts are on the low end of the range. The CD4 immunocapture chamber size was designed to a volume of 120 μl, instead of around 10 microliter reported in many literature, this is done to accommodate the dynamic range of the DNA-bead aggregation methodology. The DNA beads aggregation assay is most sensitive when examining DNA concentrations below 100 pg/μL [20], given an average mass of DNA per white blood cell of 6.25 pg [26], and that the CD4 count could range from below 10 cells/ μL to greater than 2000 cells/ μL in HIV positive patients, a small volume chamber could result in a very high concentration of DNA and, therefore, fall outside of the functional range with certain samples.

As shown in **Figure 3-6**, different isolation techniques, including syringe pumping, manual manipulation of the magnets, and active mixing by a lab rotator, were examined to achieve a reproducible isolation efficiency. The CD4+ T-cells were isolated on chip, then stained and enumerated by hemocytometer, and the result was compared with flow cytometer to calculate the efficiency.

The best CD4+ T-cells isolation results were achieved by actively mixing the blood with the Dynabeads® through rotation (details shown in **Figure 3-7** and in the experimental section). In the first step, the whole blood and CD14 beads solution remained in the CD14 chamber during rotation, and no leakage was observed due to the hydrophobic nature of the PDMS surface. During the second step, a back-flow problem from the CD4 chamber to the CD14 chamber was

encountered as a result of inherent wetting of the channel. This was overcome by reducing the volume of PBS buffer in the 120 µL CD4 chamber to 80 µL, thus leaving an air plug, which

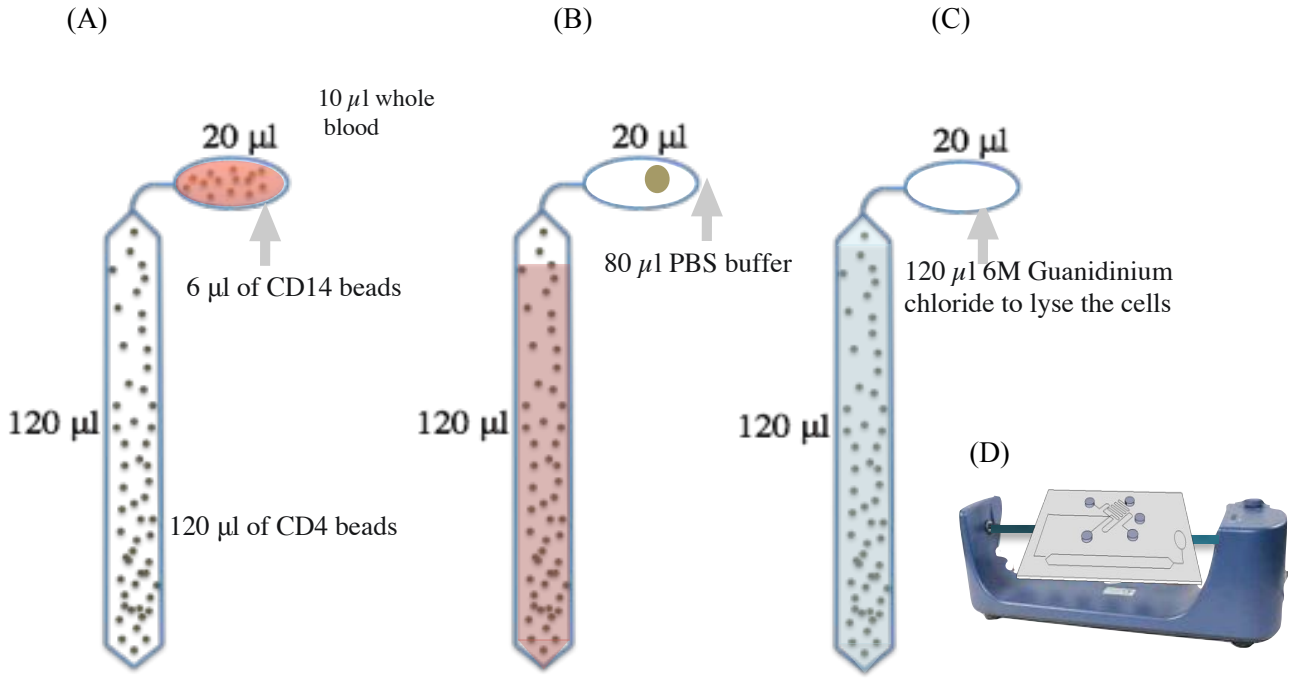

Figure 3-7*. CD4+ T-cells isolation using antibody-coated magnetic beads. The Dynabeads® T4 Quant Kit was optimized for on chip cell isolation. (A) The two chambers were coated with CD14 beads and CD4 beads respectively, by loading the bead solution and then removing the liquid while holding the beads with a magnetic manifold. A total of 10 µl whole blood was required in the assay. The T-cell isolation was achieved by loading the chip on a lab tube rotator to enhance the interaction between the beads and cells. 6 µl of CD14 beads and 10 µl of whole blood was mixed for 10 minutes. (B) 80 µl PBS buffer was added to the chip while holding the monocytes saturated beads by a magnet, and the solution was mixed for 10 minutes. After the CD4+ T-cells were isolated, 3 to 5 aliquots of 200 µl PBS buffer was loaded to wash away RBCs and unwanted WBCs, and the beads from the CD14 chamber were removed. (C) 120 µl of 6M guanidinium-HCl solution was introduced into the CD4 chamber to lyse the captured CD4+ T-cells, the cell lysing and mixing was achieved by loading the chip on the same lab tube rotator for another 10 minutes. (D) Illustration of the chip mounted on a lab tube rotator for mixing. The released cell lysate was then metered and quantitated by the DNA-beads aggregation assay.*

served to minimize back flow. The solution was mixed via rotation at 6 RPM for 10 minutes for each chamber, although this mixing time may be reduced with a higher RPM lab sample rotator. After removing the unwanted cells from the chamber loading PBS buffer, the captured CD4+ T-cells were lysed by 6M guanidinium HCl solution, which serves as both the lysing solution and the chaotropic agent to induce DNA bead aggregation. It is worth mentioning that the Dynabeads® used here can be shipped without refrigeration and stored at 4 - 8°C for 2 years, and all the experiments were carried out at room temperature, making it desirable for usage in resource-limited regions.

3.4.2 Capillary Burst Valve and Resistance Metering

The metering step utilized the capillary burst valve, specifically the geometric variation valve [25], the cell lysate solution meniscus stops at the junction where the micro channel meets the open chamber (**Figure 3-8**B inset). The driving force (syringe pump) ultimately overcomes the resisting capillary force, and then the chip meters based on the resistance of the channels, converted to the channel length here . The fluidic resistance R of a channel with rectangular cross section can be calculated by equation (1) [28].

$$R=\frac{12\mu L}{d^3 w} f\left(\frac{d}{w}\right) \qquad (1)$$

μ is the fluid viscosity, and L, w, and d are the length, width, and depth of the channel, respectively. f is a dimensionless shape factor function that approaches unity in the limit that d<<w. Given the rest parameters are the same, the channel length defines its resistance, the

metering channels were deigned with lengths of 120 mm, 60 mm, 30 mm, and 15 mm, therefore the resistance ratio is 8:4:2:1, and the metered solution will be 1:2:4:8 in volume. The circle at the center where it meets all channels, is a laser raster, it functions as a buffer zone, to ensure an equal liquid distribution into each channel.

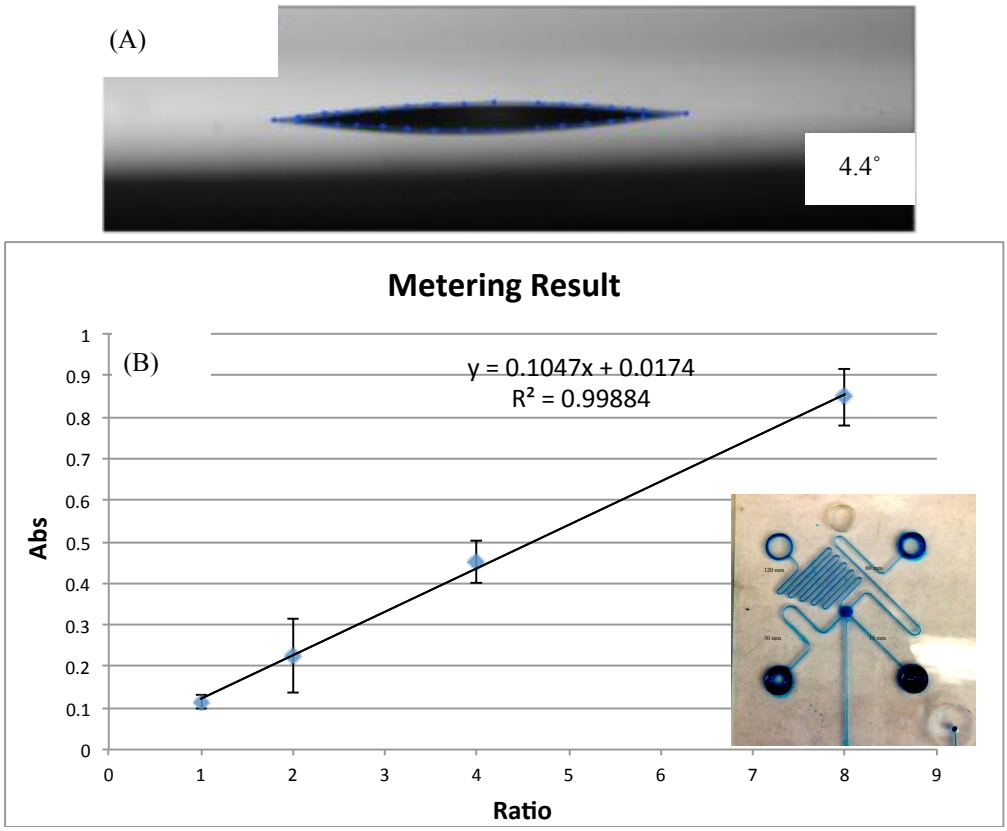

Figure 3-8. *Resistance based metering. (A) The PDMS surface was treated by plasma oxidizer to create a super-hydrophilic surface (contact angle<5°), so that the fluid only stops when the channel meets the pinwheel well (capillary valving), to ensure the metering. (B) Erioglaucine dye was metered on chip, pipetted out, and examined by UV-Vis spectrometer, n=3 on 3 different chips, the inset shows one of the on chip metering result, the channel lengths are 120mm, 60mm, 30mm and 15mm respectively.*

To be precise, the laser ablated channel is actually wedge shaped (**Figure 3-9A**), however, we can reasonably apply equation (2) as the liquid interface in a rectangular channel, PA and Po are the pressure inside and outside the channel, $\boldsymbol{\sigma}$ is the surface tension, θs and θv are

$$P_A - P_O = -2\sigma\left(\frac{\cos\theta s}{w} + \frac{\cos\theta v}{h}\right) \quad (2)$$

the contact angle with the sidewall and with the top and bottom ceilings, respectively, w and h are the width and the depth of the channel, (the channel width is 218±4.5 μm (n=3), and the channel depth is 791.25±15.95 μm (n=3), measured under microscope)(**Figure 3-9B)**. From equation (2), when the contact angle θs and θv are small, the difference between the outside and inside of the channel becomes larger, indicating the capillary valve can hold the solution without bursting, experiments have shown that when the surface is super hydrophilic (contact angle <5° as shown in Figure 3A), the metering works as designed.

Studies have shown that there is a positive correlation between the hydrophilicity and bonding strength when treating PDMS and glass with oxygen plasma [27], when the surface is super hydrophilic, the bond is the strongest. The plasma power and exposure time was optimized to achieve the super hydrophilic surface, and the metering was performed before the PDMS surface reverted to its initial hydrophobic state. Proper metering of 1 μL, 2 μL, 4 μL, and 8 μL into each well was verified by incorporation of the erioglaucine dye into the metered guanidinium HCl, analysis by UV-Vis spectrophotometry, and comparison to a calibration curve.

Light mineral oil was pumped in the CD4 chamber to prevent mixing. The metering parameters were optimized, by pumping light mineral oil into the dyed GnHCl filled chip. When

metering was finished, the dye doped GnHCl solution was extracted from the wells, diluted to 1 mL, and then analyzed with a UV-Vis spectrophotometer. The absorbance values from the 4 wells were then compared to a standard curve of 1 µL, 2 µL, 4 µL, and 8 µL aliquots of the same dyed GnHCl solution. The optimized flow rate and total flow volume were 100 µL/min and a total dispensed volume of 140 µL, in order to dispense 1 µL, 2 µL, 4 µL and 8 µL in each well (Figure 3B), the absorption and the dye concentration is linearly related, the inset shows the on chip metering result.

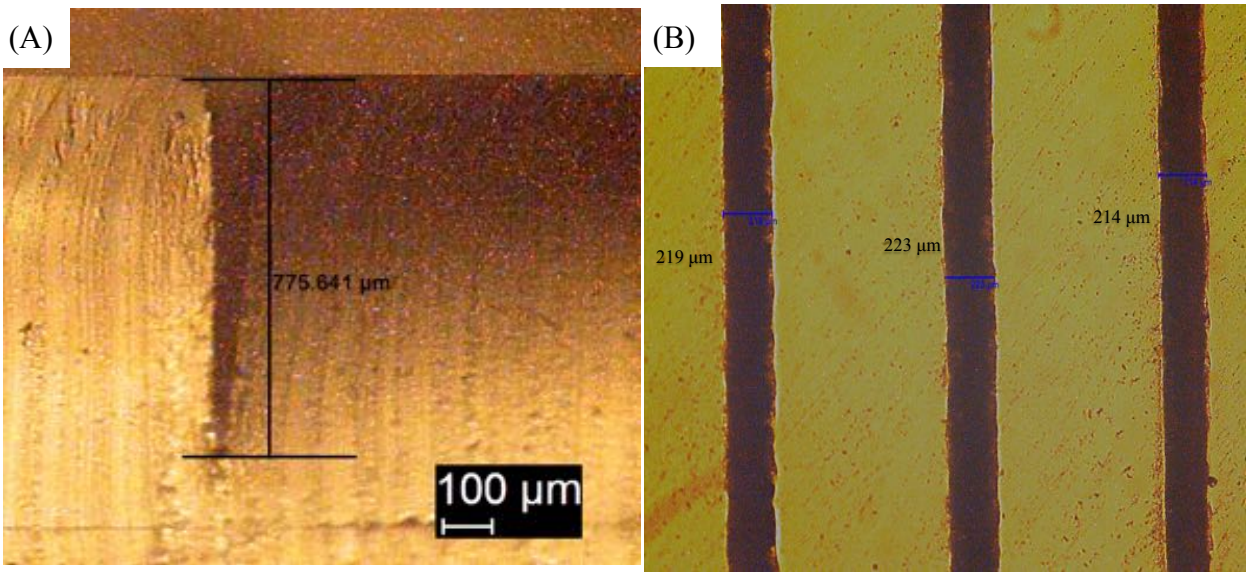

Figure 3-9. *Morphology of laser ablated PDMS channels. (A) The channel is wedge shaped, with an average depth of 791.25 µm, the picture shows one of the 3 measurements. (B) The channel average width is 218 µm.*

3.4.3 DNA-Bead Aggregation

To this point in a microfluidic system, we have demonstrated the removal of monocytes and the specific isolation of CD4+ T-cells from whole blood, lysed those cells, and metered

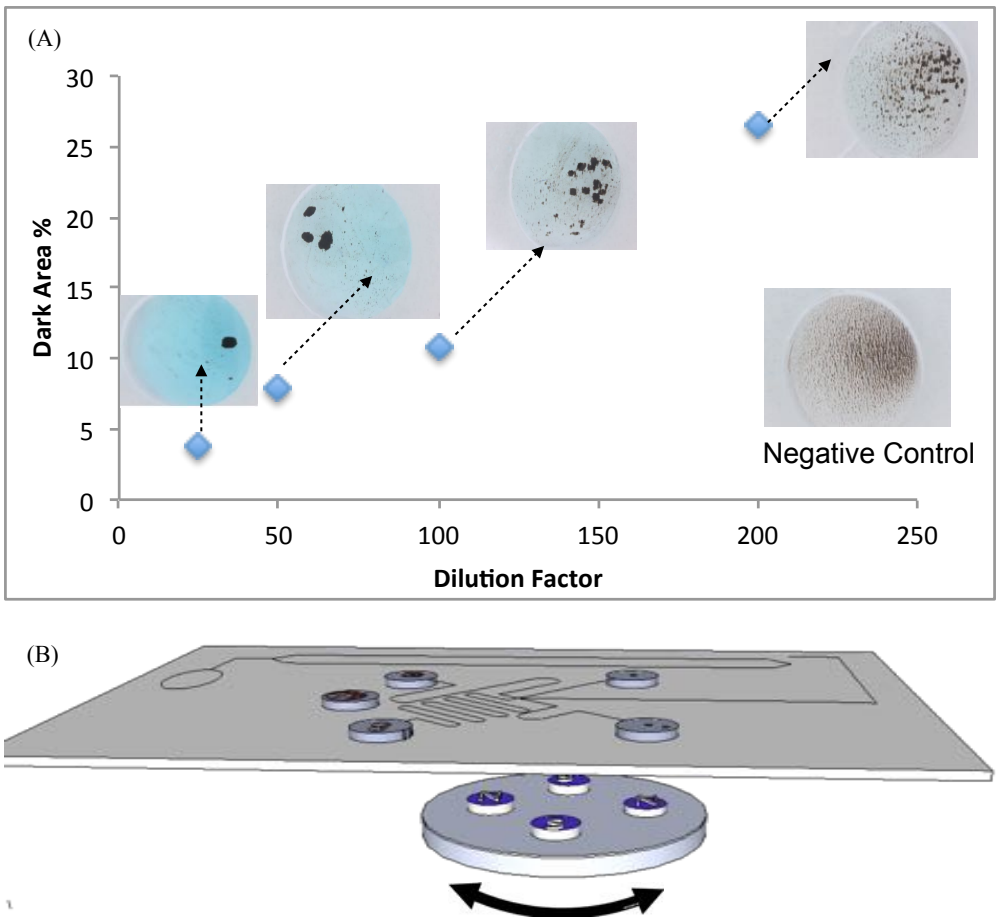

Figure 3-10. *Illustration of the on chip DNA beads aggregation assay. (A) An example of CD4+ T-cells quantified by DNA-beads aggregation on chip. To ensure an accurate count, each sample was lysed and serially diluted to generate a calibration curve. Dark area is defined as the pixels that make up the brown area. Dark area% is normalized by negative control (No DNA). The dilution factor indicates the cell concentration is 25, 50, 100 and 200 times diluted from the whole blood. (B) The rotating magnetic field set up for DNA-beads aggregation, the rotating magnetic field switch direction every 20 seconds, for a total of 3 min. The guanidinium-HCL was doped with Erioglaucine dye for illustration.*

select volumes of the DNA-containing lysate. Following the metering step, different masses of

silica-coated magnetic beads were added so that each well would have a total volume of 20 μL. Under chaotropic conditions, the silica coated magnetic beads aggregate with the DNA from the lysed CD4+ T-cells. Aggregation is quantitative and correlates with the mass of DNA present in each well [20], and therefore, the CD4+ T-cells count. After only 3 minutes, the wells were photographed with a high-resolution camera and the percentage dark area (%DA) was calculated; a higher %DA signifies a lower concentration of DNA present in the well. For each sample, an on-chip calibration curve was generated using 4 different dilutions. **Figure 3-10 A** provides the DNA-bead aggregation result for a exemplary sample, while **Figure 3-10 B** provides a schematic of the chip-based ARTμS set up

3.4.4 Clinical Studies

To test the effectiveness of the CD4+ microfluidic enumeration system, we determined CD4+ T-cells count in 43 clinical samples that had been evaluated by flow cytometry in the Clinical Chemistry laboratory. To test the efficiency for chip -based isolation of CD4+ T-cells, cells captured within the CD4 chamber were stained with Sternheimer-Malbin stain, a supravital crystal-violet/safranin solution well-established for staining WBC's, epithelial cells, and urinary casts [29]. Early efforts to define the chip-based isolation efficiency showed poor correlation between the counts obtained by flow cytometry and those by hemocytometry. It became clear that there was a significant dependence on the age of sample (time elapsed since blood draw), 24 hr was the critical cut-off point. This was supported by previous studies describing that blood samples stored at 2°C to 8°C or room temperature for >24 hours perform poorly when analyzed by immunoassay[23,24]. Given that, the Clinical Chemistry lab provided us with HIV patient

Sample <24 hours, extraction on chip, cell count by hemocytometer

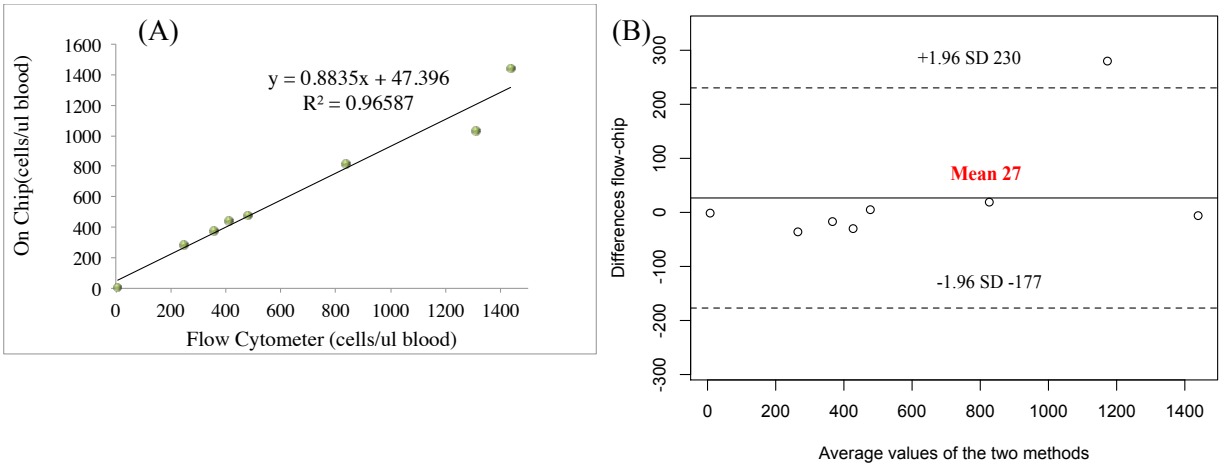

Sample >24 hours, extraction on chip, cell count by hemocytometer

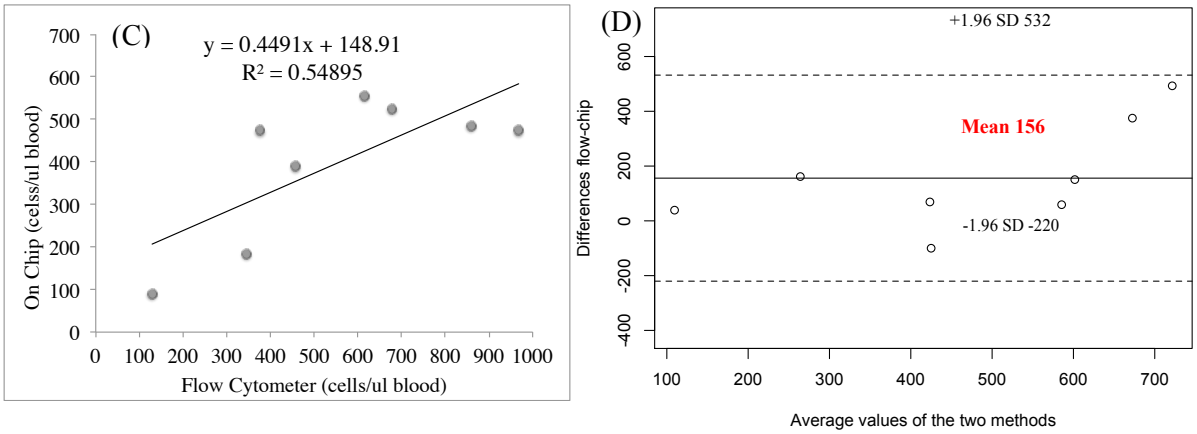

Figure 3-11. *Clinical study results compared with flow cytometry. (A) On chip isolation and hemocytometer enumeration result correlate well with flow cytometry (R^2=0.966) when samples are processed within 24 hours after blood drawn (C) Aged samples (>24 hours) are poor target of immunomagnetic separation, therefore will affect the enumeration result. (B.D.) Bland–Altman methods comparing the cell count in the chip to absolute CD4 cell counts obtained by standard four-color flow cytometry.*

blood samples that, when analyzed, would fall into two groups - within or outside of 24 hrs since

blood was drawn. **Figure 3-11 A** shows the result with samples analyzed within 24 hrs of blood draw, and the results show excellent correlation of the hemocytometry results with those from flow cytometry. The same number of blood samples (8) that had been stored for more than 24 hrs were analyzed by hemocytometry and flow cytometry and the results given in **Figure 3-11 C** confirmed our hypothesis that post-draw analysis time of <24 hrs was critical. The statistical gold standard for comparing two clinical methods is the Bland-Altman plot [30]. Evaluation of the data by this method is given in **Figures 3-11 B&D** and showed a positive bias of 27 cells/μL, and 95% limits of agreement of 230 cells/μL and -177 cells/μL with samples analyzed in <24 hours post-draw. For samples analyzed after >24 hours post-draw showed a bias of 156 cells/μL and 95% limits of agreement of 532 cells/μL and -220 cells/μL.

At this point we have proved the efficacy of the on chip isolation, metering and the 'pinwheel assay' for cell counting. To evaluate the algorithm accuracy, 17 samples were studied, where the CD4+ T-cells were isolated and lysed on chip, pipet metered, and enumerated by DNA beads aggregation. This method eliminates error from the metering step, this step usually causes the most uncertainty because of the bonding step. The results are shown in **Figure 3-12**, for 17 blood samples, a strong correlation with flow cytometer was obtained (R^2=0.95), **Figure 3-12 B** exhibits a positive bias of cells/μL, and 95% limits of agreement of 311 cells/μL and -233 cells/ μL.

With these encouraging results, we tested the efficiency of the microfluidic system for complete processing of <24 hours post-draw blood samples (specific CD4+ isolation, lysis and metering, DNA-bead aggregation) on the integrated chip-based ARTμS, i.e., blood in-cell count out. The results in **Figure 3-13 A** indicate that, for 10 blood samples, an excellent correlation

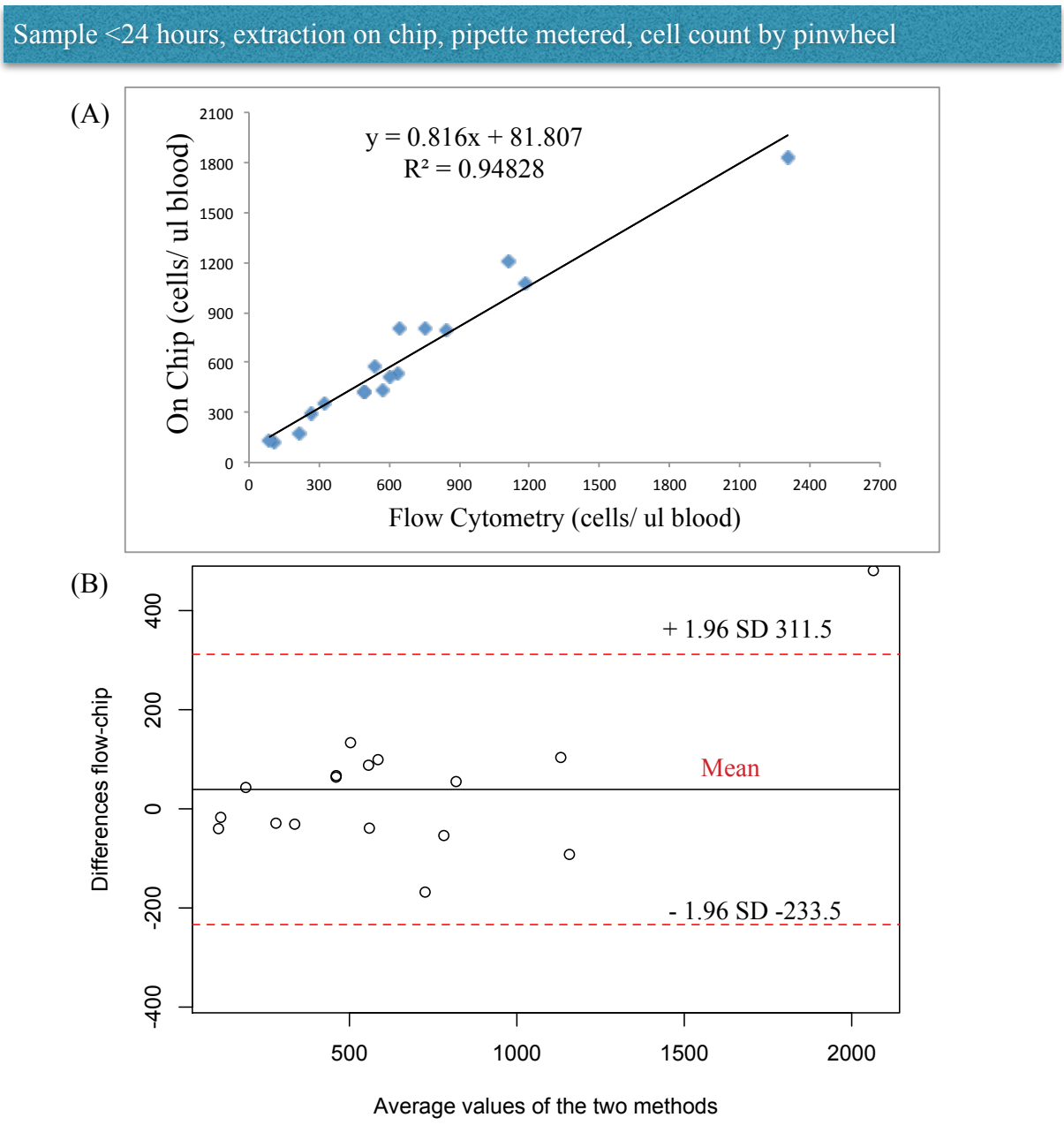

Figure 3-12. *On chip extraction and lysing, pipette metering, and pinwheel quantitation results. This is used to prove the reliability of the algorithm. (A) 17 fresh blood samples (<24 hours) were analyzed and the correlation with flow cytometry was strong (R^2=0.95) (B), Bland Altman plot indicating the mean difference between 2 methods, as well as the high and low limit.*

was obtained with the flow cytometry results. The Bland–Altman plot results are given in

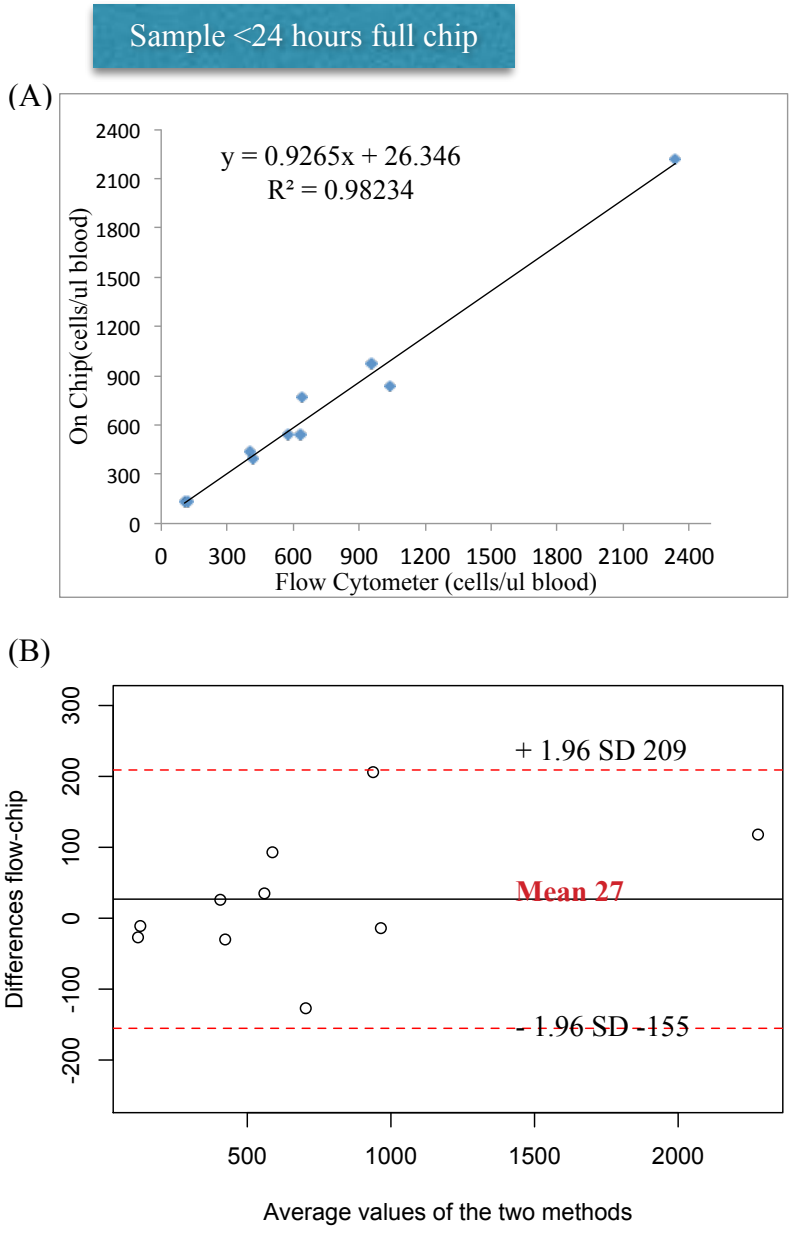

Figure 3-13. *Integrated chip blood in, cell count out result. Fresh blood samples (<24 hours) were fully processed on chip i.e., CD4+ T cell were extracted and lysed on chip, metered on chip, and quantitated by the pinwheel assay on chip. (A) 10 samples were analyzed and the correlation with flow cytometry was good (R^2=0.98) (B), Bland Altman plot indicating the mean difference between 2 methods, as well as the high and low limit.*

Figure 3-13 B and indicate that these samples exhibit a positive bias of 27 cells/µL, and 95%

limits of agreement of 209 cells/μL and -155 cells/μL. Given the new ART initiation threshold of 500 cells/μL, the ARTμS developed assay correctly categorized all those (samples <24 hours after extraction) determined by flow cytometry to be eligible for the ART. Hence, while still is the breadboard stage, the ARTμS has the potential to provide a rapid, label-free and cost-effective alternative to flow cytometry.

3.4.5 Super Hydrophilic Coating of PDMS

The ARTμS is fast, cost effective and label free, however, it's still in breadboard stage, because successful operation of a technically complex assay requires the ability to perform all the steps at once, in a seamless and automated fashion. To make it really applicable in the field, and to introduce it into the market one day, we need to first address the metering issue, this step prevents the creation of a pre-packaged microfluidic chip that maintains the hydrophilicity of the embedded channels. In order to circumvent this process, treatment of the PDMS surface with a super hydrophilic coating was tested.

The selected super hydrophilic coating was HydroPhil™ obtained from Lotus Leaf Coatings. Industrially, this coating was intended for use on metal surfaces, with demonstrations of treated copper surfaces showing water to surface contact angles approaching 0°. Trials with HydroPhil™ on aluminum metal demonstrate consistent and reliable hydrophilicity with a measurable difference between untreated aluminum (**Figure 3-14A**) and treated aluminum (**Figure 3-14 B**). Hydrophilicity was observed to be consistent over the entire treated surface.

Application of HydroPhil™ directly to PDMS surface was unsuccessful regardless of the method of application. These results could be due to the high hydrophobicity of the PDMS

surface (**Figure 3-14 C**) resulting in the inability of an aqueous solution to achieve enough surface contact to enact a change in the surface chemistry of the PDMS.

A pretreatment for PDMS consisting of 5% 3-Aminopropyltrimethoxysilane (APTMS) in ethanol was used to resolve the coating difficulty. The APTMS attaches to the hydroxyl functional groups protruding from the surface of the PDMS, rendering the amine functionality of the APTMS available for reaction with the compounds present in the HydroPhil™ [31]. The interaction mechanism between the coating and the APTMS cannot be determined as the composition of the coating is unknown (industrial secret). If the hydrophilic properties of the coating are due to the presence of polysaccharides, it is possible that the coating directly interacts with the APTMS present on the PDMS surface [32]. If the hydrophilic properties are due to the presence of metal compounds, then it is possible that the hydrophilic properties stem from the formation of thin films of interacting metal compounds [33]. Other types of coating-surface interactions are possible, however without knowing the chemical composition it is difficult to determine which mechanism most accurately describes the HydroPhil™ - PDMS interaction.

The swab (**Figure 3-14 D**) and pour (**Figure 3-14 E**) methods of HydroPhil™ application both yielded large contact angles, and therefore poor hydrophilicity. The submersion method (**Figure 3-14 F**) however yielded smaller contact angles, and therefore much greater hydrophilicity than other treatment methods. Although the surface does demonstrate hydrophilicity with this method, the surface properties are not consistent throughout the entire surface area. This could be due to the hydrophobic properties of the natural PDMS prohibiting the pretreatment from thoroughly bonding to the functional groups.

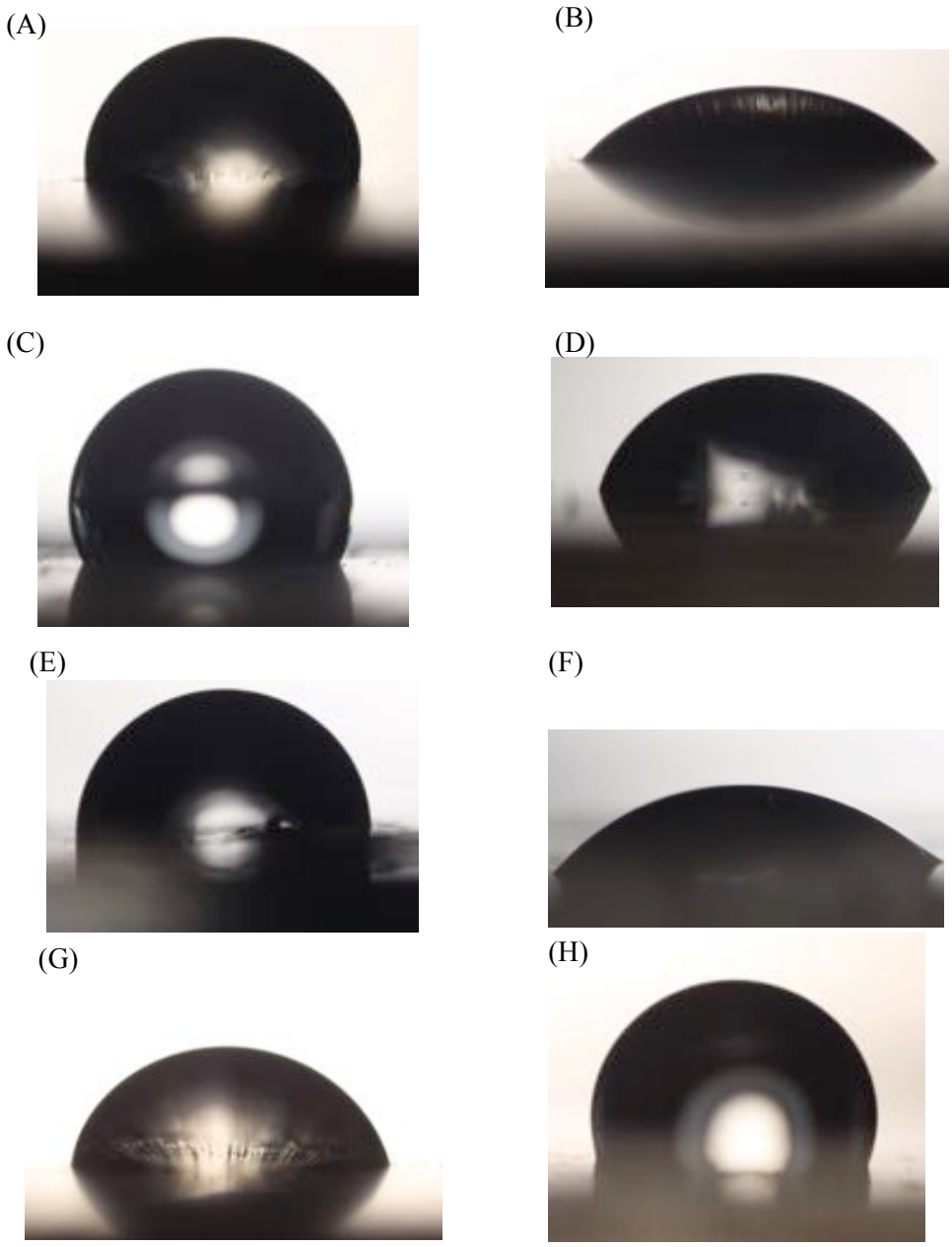

Fig 3-14 *HydroPhil™ super-hydrophilic coating test results. (A) Untreated aluminum with water. (B) HydroPhil™ treated aluminum. (C)Untreated PDMS (D)HydroPhil™ treated PDMS with the swab method. (E)HydroPhil™ treated PDMS with the pour method. (F)HydroPhil™ treated PDMS with the submersion method. (G)Aluminum treated with HydroPhil™ after 48 hours (H)PDMS treated with HydroPhil™ after a period of 48 hours exposing to air. A total of 5 µl DI water placed on the surface.*

In order to combat this, the PDMS was then treated with air plasma for 45 seconds before application of the pretreatment and HydroPhil™. The binding of the APTMS to the PDMS has been observed to make stronger and more frequent bonds when the PDMS has silanol groups present on its surface [31]. The PDMS treated with plasma demonstrated much more consistent hydrophilicity over its entire surface area.

To observe the stability of the coating, both treated PDMS and aluminum were allowed to rest, exposed to air, for a period of 48 hours. The aluminum retained some of its hydrophilic properties, however it appeared to relax back into a state of relative hydrophobicity (**Figure 3-14 G**). Similarly, the treated PDMS retained no hydrophilic properties, relaxing back into its natural hydrophobic state (**Figure 3-14 H**). Even with surface consistency and stability over an extended period of time, it is unlikely that the HydroPhil™ coating will be significantly useful in this application. The smallest contact angle obtained from treatment of PDMS with HydroPhil™ is significantly larger than the desired contact angle obtained from treatment with air plasma (**Figure 3-8 A**). The implication for Lotus Leaf Coating's HydroPhil™ super-hydrophilic coating is that it is not of use in this particular application, however if other coatings can be found that consistently increase the hydrophilicity to levels nearing that of plasma treatment, further trials may be worthwhile.

3.5 Concluding Remarks

In summary, we have developed a microfluidic system integrating the DNA bead aggregation assay to accurately quantitate CD4+ T lymphocytes in a fast, label-free, and low cost manner. The correlation with the flow cytometry was excellent (R^2=0.98). This chip holds

potential as an alternative for CD4+ T-cells counting in resource-limited regions. In order to make the process more automatic and less time sensitive, a permanent super-hydrophilic coating is required, the commercial product HydroPhil™ that we examined was not adequate, more coating methods need to be evaluated, or other metering resources should be explored.

3.6 Reference

1. UNAIDS, Global report: UNAIDS report on the global AIDS epidemic 2013, UNAIDS/ JC2502/1/E, WHO, Geneva, 2013.
2. Jani, I. et al. Effect of point-of-care CD4 cell count tests on retention of patients and rates of antiretroviral therapy initiation in primary health clinics: an observational cohort study. ***Lancet***, 2011, 378(9802), 1572–9.
3. Janossy G, Jani IV, Bradley NJ, Bikoue A, Pitfield T Affordable CD4+ -T-cell counting by flow cytometry: CD45 gating for volumetric analysis. ***Clin Diagn Lab Immunol*** 2002, 9, 1085–1094.
4. Glynn, M. T., Kinahan, D. J., & Ducrée, J. CD4 counting technologies for HIV therapy monitoring in resource-poor settings--state-of-the-art and emerging microtechnologies. ***Lab on a Chip***, 2013,14, 2731–48.
5. Cheng, X. A microfluidic device for practical label-free CD4+ T cell counting of HIV-infected subjects. ***Lab on a Chip***, 2007, 7(2), 170–178.
6. Cheng, X.,Enhancing the performance of a point-of-care CD4+ T-cells counting microchip through monocyte depletion for HIV/AIDS diagnostics. ***Lab on a Chip***, 2009, 9(10), 1357–1364.

7. Rodriguez, W. R. *et al*. A microchip CD4 counting method for HIV monitoring in resource-poor settings. ***PLoS Medicine***, 2005, 2(7), 0663–0672.
8. Li, X *et al*. Clinical evaluation of a simple image cytometer for CD4 enumeration on HIV-infected patients. ***Cytometry B Clin. Cytom***. 2010, 78, 31-36.
9. Jesse V. Jokerst *et al.* Integration of semiconductor quantum dots into nano-bio-chip systems for enumeration of CD4+ T cell counts at the point-of-need. ***Lab Chip.*** 2008, 8, 2079-2090.
10. Ymeti, A *et al*. A single platform image cytometer for resource-poor settings to monitor desease progression in HIV infection***. Cytometry A*** 2007, 71,132-142.
11. Wang, Z *et al*. Microfluidic CD4+ T cell counting device using chemiluminescence based detection. ***Anal. Chem.*** 2010, 82, 36-40.
12. Watkins, N, N, *et al*. A microfabricated electrical differential counter for the selective enumeration of CD4+ T lymphocytes. ***Lab Chip*** 2011, 11,1437-1447.
13. Coulter, W. ***Proc. Natl. Electron. Conf.*** 1956, 12, 1034.
14. Bachelder, E.M. *et al.*. Utilizing a quartz crystal microbalance for quantifying CD4+ T cell counts***. Sensor Lett***. 2005, 3, 211-215.
15. Zachariah, R.et al. Viewpoint: why do we need a point of care CD4 test for low-income countries? ***Trop. Med. Int. Health*** 2011,16, 37-41.
16. Glynn, M. T., Kinahan, D. J., & Ducrée, J. Rapid, low-cost and instrument-free CD4+ cell counting for HIV diagnostics in resource-poor settings. ***Lab on a Chip,*** 2014, 14(15), 2844–51.

17. C. Logan, M. Givens, J. T. Ives, M. Delaney, M. J. Lochhead, R. T. Schooley and C. A. Benson, ***J. Immunol. Methods,*** 2012, 387, 107–113.

18. M. Murtagh, 2012 HIV/AIDS Diagnostic Technology Landscape: 2nd Edition, World Health Organisation, Geneva, 2012.

19. Cheng, X., Liu, Y., Irimia, D., Demirci, U., Yang, L., Zamir, L., Bashir, R. Cell detection and counting through cell lysate impedance spectroscopy in microfluidic devices. ***Lab Chip***, 2007,6, 746–55;

20. Leslie, D. C., Li, J., Strachan, B. C., Begley, M. R., Finkler, D., Bazydlo, L. A., Landers, J. P. New detection modality for label-free quantification of DNA in biological samples via superparamagnetic bead aggregation. ***J Am Chem Soc***, 2012,134, 5689–5696;

21. Li, J., Liu, Q., Alsamarri, H., Lounsbury, J. a, Haversitick, D. M., & Landers, J. P. Label-free DNA quantification via a "pipette, aggregate and blot" (PAB) approach with magnetic silica particles on filter paper. ***Lab Chip***, 2013,5,955–61;

22. Liu, Q., Li, J., Liu, H., Tora, I., Ide, M. S., Lu, J., … Landers, J. P. Rapid, cost-effective DNA quantification via a visually-detectable aggregation of superparamagnetic silica-magnetite nanoparticles. ***Nano Research***, 2014,5,755–764;

23. Li, J., Liu, Q., Xiao, L., Haverstick, D. M., Dewald, A., Columbus, L., … Landers, J. P. Label-free method for cell counting in crude biological samples via paramagnetic bead aggregation. ***Analytical Chemistry***, 2013, 85, 11233–9.

24. Diagbouga, S. et al. Successful implementation for a low-cost method for enumerating CD4+ T lymphocytes in resource-limited settings: the ANRS 12-26 study. ***AIDS*** 2003, 17: 2201–2208

25. Cho, H., Kim, H.-Y., Kang, J. Y., & Kim, T. S. How the capillary burst microvalve works. ***Journal of Colloid and Interface Science***, 2007,306(2), 379–85.

26. Butler, J. M. Forensic DNA typing: Biology, Technology, and Genetics of STR Markers, 2nd ed.; ***Elsevier Academic Press***: Burlington, MA, 2005.

27. Bhattacharya, S., Datta, a., Berg, J. M., & Gangopadhyay, S. Studies on surface wettability of poly(dimethyl) siloxane (PDMS) and glass under oxygen-plasma treatment and correlation with bond strength. ***Journal of Microelectromechanical Systems***, 2005, 14(3), 590–597.

28. J.B. Bao and D.J. Harrison, Measurements of flow in microfluidic networks with micrometer-sized flow restrictors, ***AIChE Journal***, 2006, 52, 75-85.

29. Harris, D. M. Staining of urinary leucocytes as an aid to the diagnosis of inflammation in the urinary tract. ***Journal of Clinical Pathology***, 1969, 22(4), 492–495.

30. Hanneman SK. "Design, analysis, and interpretation of method-comparison studies". ***AACN Advanced Critical Care*** 2008, 19 (2): 223–234.

31. Watts, B., et al., Fabrication and Performance of a Photonic-Microfluidic Integrated Device. Micromachines. 2012.

32. Bauer, S., et al, Adhesion of Marine Fouling Organisms on Hydrophilic and Amphiphilic Polysaccharides. ***Langmuir***. 2013.

33. Eskandari, A., Sangpour, P., Vasezi.,. Hydrophilic Cu2O Nanostructured Thin Films Prepared by Facile Spin Coating Method: Investigation of Surface Energy and Roughness. ***Materials Chemistry and Physics***. 2014.

34. David S. Boyle. ***Trends Biotechnol.*** 2012 Jan; 30(1): 45–54.

Chapter 4. The Pinwheel Assay Via a 'Pipet, Aggregate, and Blot' Approach

4.1 Overview

Reliable measurement of DNA concentration is essential for a broad range of applications in biology and molecular biology, and for many of these, quantifying the nucleic acid content is inextricably linked to obtaining optimal results. In its most simplistic form, quantitative analysis of nucleic acids can be accomplished by UV-Vis absorbance and, in more sophisticated format, by fluorometry. A recently reported new concept, the 'pinwheel assay', involves a label-free approach for quantifying DNA through aggregation of paramagnetic beads in a rotating magnetic field. Here, we describe a simplified version of that assay adapted for execution using only a pipet and filter paper. The *'pipette, aggregate, and blot'* (PAB) approach allows DNA to induce bead aggregation in a pipette tip through exposure to a magnetic field, followed by dispensing (blotting) onto filter paper. The filter paper immortalizes the extent of aggregation, and digital images of the immortalized bead conformation, acquired with either a document scanner or a cell phone camera, allows for DNA quantification using a noncomplex algorithm. Human genomic DNA samples extracted from blood are quantified with the PAB approach and the results utilized to define the volume of sample used in a PCR reaction that is sensitive to input mass of template DNA. Integrating the PAB assay with paper-based DNA extraction and detection modalities has the potential to yield 'DNA quant-on-paper' devices that may be useful for point-of-care testing.

4.2 Introduction

Breakthroughs in methods for genetic analysis have blazed the trail for the development of clinical diagnostic and forensic applications. Typical work flow for DNA analysis includes DNA preparation and quantification, amplification by polymerase chain reaction (PCR), and subsequent detection (with or without fragment separation). The success of amplification often depends on the quality of prepared DNA, specifically purity and concentration; thus, a quantification step often precedes amplification and, in some cases, is critical to acquiring reliable results.

In a standard laboratory setting, UV-Vis absorbance and fluorescence spectroscopy are commonly used to quantify DNA at concentrations from nanogram down to picograms per microliter prior to PCR, of which the performance seems to suffice for a variety of applications. Measuring UV adsorption at the wavelength of 260 nm is the most convenient and common technique to quantify DNA with concentration around 1−250 ng/μL. Another widely used technique is fluorescence spectroscopy, wherein fluorescent probes specifically bind to DNA through various mechanisms and generate fluorescent signal that are proportional to DNA mass. For example, the commercially available probe PicoGreen® binds to the minor groove of double−stranded DNA (dsDNA), and dsDNA can be detected down to 1 pg/μL. Although the limit of detection is improved using fluorescence spectroscopy, costly and sophisticated hardware is involved, and repetitive calibration is required due to the unstable optical properties of fluorescent labels.

With a view to point-of-care applications, paper-based microfluidic systems have been the focus of much attention due to their portability, cost-effectiveness and low power requirements. The majority of publications in this area have been focused on detecting analytes such as ions[1], organic molecules[2-3], proteins[3-4], and DNA sequences[5], optically or electrochemically at endpoint. Govindarajan et al. recently reported a lab-on-paper device for cell lysis and DNA extraction as the preparation step of genetic analysis at the point of care [6], which could be combined with microfluidic PCR systems [7-9] and paper-based detection methods for rapid sample-to-result tests. However, DNA quantification remains difficult in a microfluidic system because of the large footprint, complexity and cost associated with the conventional techniques, and a simple DNA quantification method that can be integrated into paper-based sample-to result tests will provide timely feedback to DNA isolation at the point of care, and assure sample quality for PCR and further analysis.

We have recently shown a new label-free modality for DNA quantification, the 'pinwheel assay', based on the aggregation of paramagnetic microbeads induced by DNA in a rotating magnetic field [10]. Simple image analysis on the aggregation eliminates the need of fluorescent labels and corresponding optics and enables integration of the pinwheel assay into microfluidic systems. In this report, we extend the assay to an even more portable and cost-effective approach, in which the aggregates are prepared in an 'image-ready' form via a 'Pipet, Aggregate and Blot' (PAB) approach on filter paper, and are transformed into quantitative digital information by a photo scanner or a cell phone camera. This report evaluates the analytical performance of the PAB assay and demonstrates an application of quantifying DNA templates for PCR and subsequent detection.

In addition, consistent with the concept of developing simple telemedicine using camera phones and paper-based microfluidic devices for developing regions[4,11], the PAB assay enables rapid quantification of nanogram-scale samples prior to downstream analysis with enhanced simplicity, portability and cost-effectiveness compared with conventional techniques. Combining with paper-based DNA extraction and detection modalities, the PAB assay could serve as a starting point towards more integrated lab-on-paper devices for point-of-care genetic analysis in resource-limited regions.

4.3 Materials and Experimental Methods

4.3.1 Materials

1 μm Dynabeads® MyOne™ SILANE was purchased from Life Technologies. 8 μm Magnesil paramagnetic beads were purchased from Promega. Lambda phage genomic DNA (48.5 kb long) was purchased from USB (Cleveland, OH). Human genomic DNA was purified from whole blood with DNA isolation kit purchased from QIAGEN. Whole blood samples were donated by consenting donors. Qualitative Grade 3 Filter Paper with 6 micrometer particle retention was purchased from Whatman®. Pipet tips (VWR Universal Fit Bevel Point Pipet Tip) were purchased from VWR. AmpFlSTR® COfiler® PCR Amplification Kit purchased from Applied Biosystems was used for STR analysis.

4.3.2 Reagent and Sample Preparation

200 μL of Dynalbeads® Myone™ Silane was washed 3 times with GdnHCl solution (8 M, 1× TE, adjusted to pH 6.1 with 100 mM MES) and then diluted 10 times with 6M GdnHCl solution. 30 μL of stock Magnesil beads was washed once with deionized, distilled water (Nanopure) followed by one wash with 8M GdnHCl solution and resuspended in 1 mL of GdnHCl solution to make the suspension. Human genomic DNA was purified from whole blood with QIAGEN DNA isolation kit following instructions from the manufacture. The DNA concentration of standard samples was determined with UV-Vis spectroscopy. DNA samples were diluted serially with 1× TE buffer (10 mM Tris base, 1 mM EDTA, pH 8.0) to appropriate concentrations, aliquoted, and stored at −20 °C until use.

4.3.3 DNA Quantification with The PAB assay

2 μL of magnetic beads and 1 μL of DNA sample were mixed in a pipet tip, and the mixture was exposed to a magnetic field around 1000 Gauss for 40 seconds to induce bead aggregation. The 3-μL droplet was dispensed onto filter paper, forming a wet area around 1 cm in diameter. After the area dried by evaporation at room temperature, the image of aggregates on the paper was acquired with EPSON Perfection V100 Photo Scanner or iPhone 3GS for data analysis.

4.3.4 Image Processing

Images of each dispensed area were cropped from the original photo in TIF format. The images were imported into Mathematica in HSB (hue-saturation-brightness) mode, and the saturation data was extracted for further analysis. An isodata algorithm written in

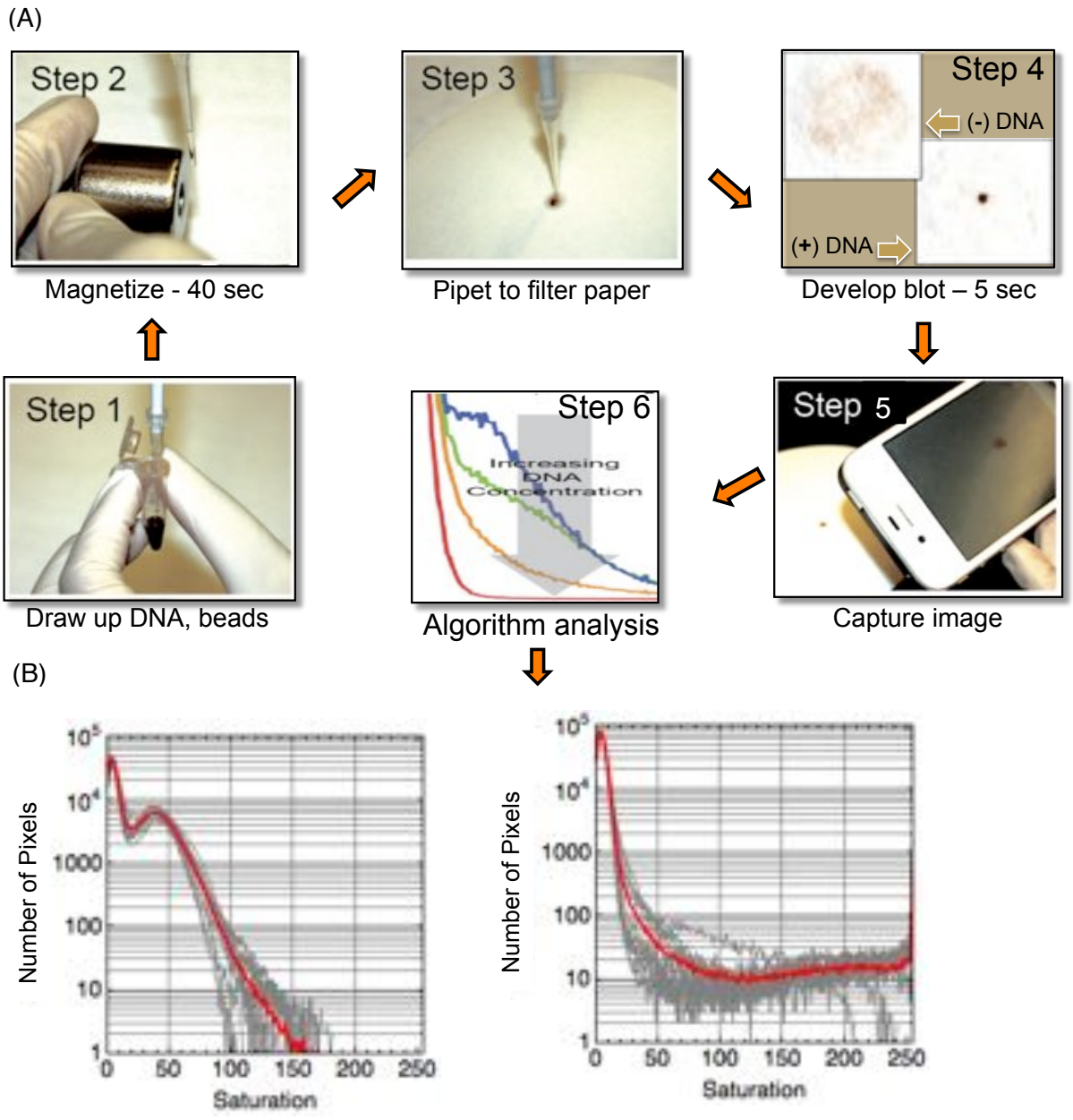

Figure. 4-1 *The pinwheel assay via the PAB approach. (A) Step by step experimental procedure. (B) Saturation histograms in HSB (hue–saturation–brightness) color space of the negative and positive controls. The red curve represents the average of the 14 replicates (gray curves)*

Mathematica10 was applied to the saturation data of negative controls (beads without DNA), and it defined a threshold for all the images, above which the pixels represent the beads and aggregates. The total number of these pixels in each image (i.e., dark area) was normalized to the negative controls, and correlated with DNA concentration.

4.3.5 STR Analysis

STR analysis was performed according to manufacture's instruction. Briefly, DNA samples were amplified using the AmpFlSTR COfiler kit reagents, and the PCR products were separated on ABI PRISM 310 Genetic Analyzer, which generates electropherograms for further interpretation.

4.3.6 Recover DNA After Quantification

1 µl *whole blood* was mixed with 1 µl of Magnesil® beads in pipet for 30 seconds, exposing an external magnet, the resulting solution was blotted on filter paper. The wetted area with beads was punched out and placed in a tube. 100 µl 80% Isopropanol Alcohol (IPA) was added to the tube, vortexed, and incubated for 15min (repeat 3 times). Elute with 50 µl 0.1xTE, incubate 30min at r.t. Remove any possible beads residue by a magnet, the supernatant was pipetted out and added to the PCR master mix.

4.3.7 Polymerase Chain Reaction (PCR) Amplification

The 0 base pair (bp) region human β-globin gene was chosen to be amplified as the target. The master mix consisted of 1 μL 20 μM forward and reverse primers, 1 μL 10 mM dNTP, 5 μL 10x PCR buffer, and 6 μL $MgCl_2$. Each sample consists of 13.5 μL master mix, 10 μL nuclease free water, 0.5 μL Fisher Taq polymerase, and 1 μL of human DNA template. Thermal cycling conditions were as follows, an initial hold at 95 °C for 5 min, 30 cycles of 92 °C for 30 sec, 60 °C for 30 sec, and 72 °C for 30 sec, followed by a final hold at 72 °C for 2 min. After the completion of PCR, the sample was removed from the tube and the product was separated and detected using an Agilent 2100 Bioanalyzer (Agilent Technologies, Inc., Santa Clara, CA, USA).

4.4 Results and Discussion

4.4.1 PAB Assay Development

The "pinwheel assay" has been shown as a simple, cost-effective, and accurate method for DNA quantification[12]. When considering applications that deal with real-world samples, we are developing two formats of the assay. The first is a shoebox-sized system that accommodates a multiplexed microwell device for parallel processing of multiple samples for DNA quantification in a high throughput manner[13]. This is under development and will be ideal as a central clinical lab or research-focused tool.

The elegance of the pinwheel concept is its simplicity, and the second format aims to exploit this with a focus on point-of-care testing. This involves applying the pinwheel

phenomenon in an orthogonal format using smaller, more portable, cost-effective hardware with a simple-to-execute methodology. In point-of-care testing, particularly with Global Health applications, cost-effectiveness and sensitivity must be balanced, but simplicity for an unskilled user is a must. The PAB approach to the pinwheel assay (**Figure 4-1**) utilizes the most simple, inexpensive, and readily available materials in research laboratories - a pipet, a magnet for aggregation, filter paper for immortalising the state of aggregation, and a cell phone as the modality for data acquisition, transmission and analysis.

As shown in **Figure 4-1A**, the PAB assay involves: (1) pipetting both a suspension of silica-coated magnetic beads in GuHCl and an aliquot (typically 1 μL) of DNA-containing sample, (2) promoting DNA-bead aggregation by exposure to a magnetic field, (3) dispensing the pipetted volume (blotting) onto filter paper, (4) acquire the image of blotted filter paper with a photo scanner or a cell phone camera, and (5) transferring the data from the scanner to a computer for quantitative processing. Using a cell phone camera (iPhone 3GS with 3 Megapixels) to acquire images also suffices for image capture and quantification. At the point of care, cell phones can be used to send data to a central laboratory and receive results through cellular network, or with the computing power of a smart phone, the data can be processed on site.

In the absence of DNA ('-' in **Figure 4-1A**), the beads remain in a dispersed state within pipet tip, and when dispensed (blotted) onto filter paper, they spread over a large area. In the presence of DNA ('+' in **Figure 4-1A**), DNA strands adsorb onto nearby silica beads driven by the chaotrope (8M GdnHCl); the applied magnetic field mobilizes the beads, enhancing DNA-bead interaction and, thus, promoting further aggregation. When blotted on the filter paper, the

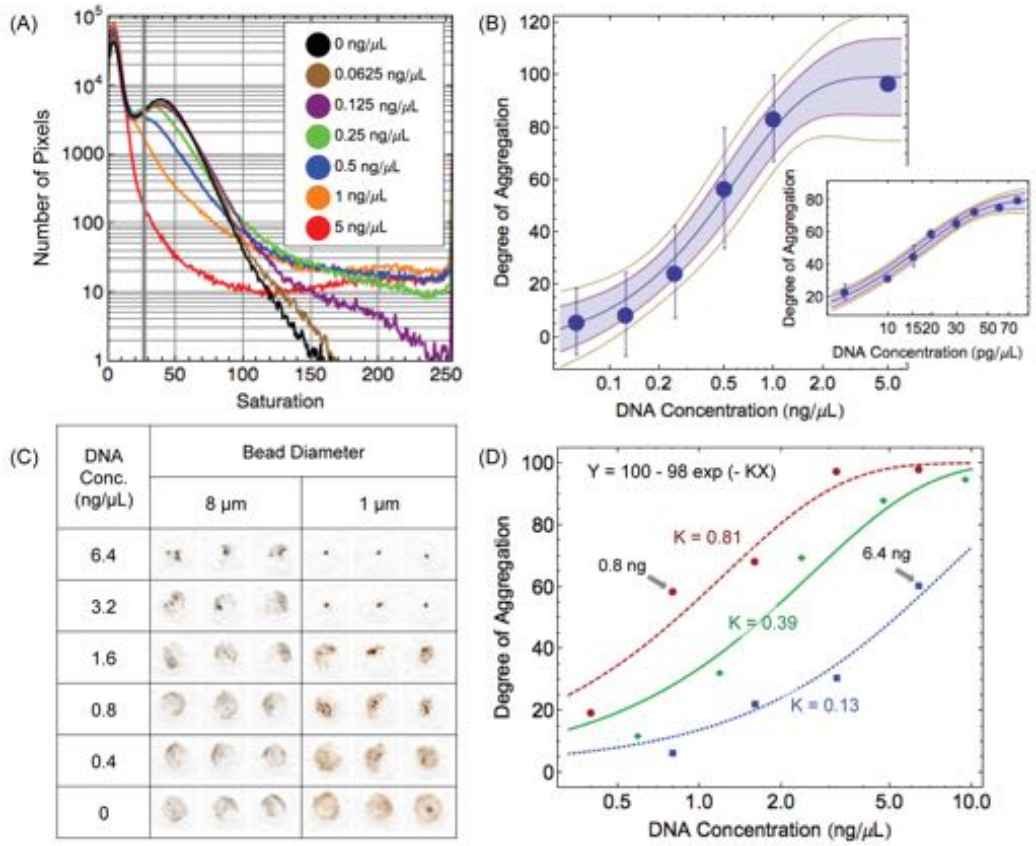

Figure. 4-2 *Algorithm and standard curve for DNA quantification. (A) The average histograms at saturation channel (n = 14) at various DNA concentrations illustrate dispersed beads converting to tight aggregates. The gray line represents the threshold that defines 'Degree of Aggregation'. (B) The degree of aggregation values were normalized with the negative control and correlated with DNA concentration. Error bars denote standard deviation (n = 14), with the 95% (purple lines) and 99% (golden lines) confidence intervals. The inset illustrates the standard curve of the previously reported pinwheel assay12 with the same DNA sample. (C) Adjusting the sensitivity by varying the size of beads. DNA strands are more effective to induce the aggregation of smaller beads. (D) The standard curves resulting from the use of either 1 mm (red) or 8 mm beads (blue). The green curve represents the standard curve resulting from a 1 : 1 mixture of the 1 mm and 8 mm beads. Each set of data points are fitted into an exponential model Y = 100 -98 exp(-2KX), in which K, as the only variable and the coefficient before DNA concentration, indicates the sensitivity.*

beads appear focused to a pinpoint. The images are imported into Mathematica in HSB (hue-

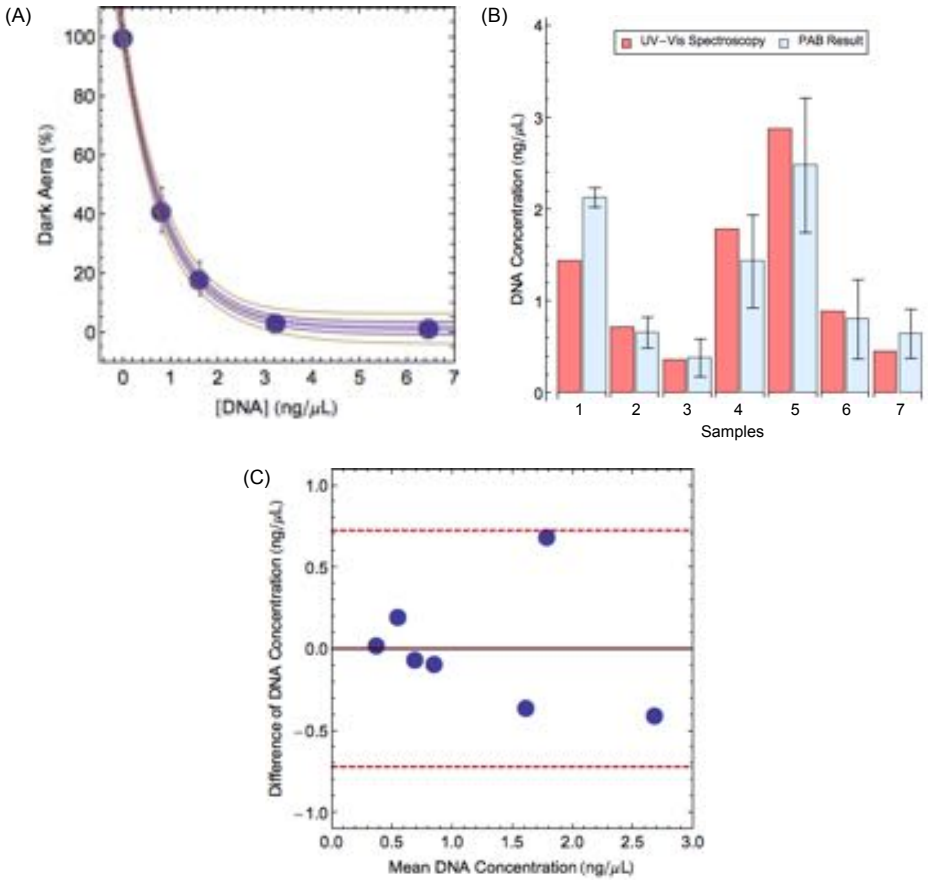

Figure. 4-3 *Quantification of human genomic DNA extracted from blood samples. (A) A standard curve was generated with serially diluted DNA samples. (B) The DNA concentrations of seven samples were measured with the PAB assay and compared with the results from UV-Vis spectroscopy. Error bars denote the standard deviation of four experiments. (C) The Bland–Altman plot reveals the agreement between the PAB assay and UV-Vis spectroscopy, with a difference band of ± 0.7 ng/ μl at 95% confidence (red dashed lines).*

saturation-brightness) mode. The hue data is not well defined for white color, and the change of brightness data appears less sensitive to bead aggregation than saturation, so the saturation data is selected to characterize the difference between images. Two peaks evolve in the saturation histogram of negative controls, corresponding to the white background (saturation = 0 - 20) and

light brown beads (saturation >20). In the histogram of positive controls, the white background peak remains while the other peak shift to saturation above 250, which represents the dark brown aggregates (**Figure 4-1B**). The change in the saturation histogram thus provides a simple means to quantify the extent of aggregation, which correlates with DNA concentration.

In order to extract quantitative information from the images, serially diluted DNA samples were assayed by the PAB method. As shown in **Figure 4-2A**, the saturation histograms for each sample was distinct, clearly illustrating the transition from dispersed beads to tight aggregates as DNA concentration was increased. In order to subtract the white background from each image, a threshold needed to be established to distinguish the pixels representing the dispersed beads or bead aggregates; this was achieved by applying the isodata algorithm reported previously to the negative controls[10]. In all images, regardless of differences in DNA concentration, the beads and aggregates can be quantitatively represented by the number of pixels with a saturation above the threshold - this is referred to as 'dark area'. As seen in Figure 2B, the total number of pixels (i.e., dark area) decreases (due to the loss of dispersed beads) as the aggregates evolve in the presence of DNA. The dark area values are normalized against the negative control, and correlated with DNA concentration, which fits well in an exponential model (**Figure 4-2B**). The sensitivity is not as high as previously reported with the pinwheel assay[10], primarily because the dispersed beads are not distributed on a solid support (filter paper) as evenly as they are in microwell, which compromises reproducibility slightly, and leads to means with a larger standard deviation. However, some sensitivity is sacrificed here for simplicity, low-tech, cost-effective measurement.

It is interesting that the limit of detection (LOD), sensitivity, and dynamic range of the PAB assay can be tuned by varying the bead size, since the same amount of DNA can bind to more beads with smaller diameter. As shown in **Figure 4-2C**, aggregation is visually detectable at 800 pg/μL DNA with the 1 μm beads, whereas the same extent of aggregation with the 8 μm beads requires almost an order of magnitude higher DNA concentration (6.4 ng/μL). A rough quantitative analysis indicates that the sensitivity increases by 8-fold with an 8-fold decrease in diameter. Not surprisingly, a 1:1 mixture of the two bead sizes resulted in a sensitivity that was an average of the two (**Figure 4-2D**). The effect of bead size on aggregation efficiency indicates that the LOD, sensitivity, and dynamic range can be tuned by adjusting the mean bead diameter, and more sensitive detection could be achieved with magnetic beads at nanometer scale. These are not commercially-available and are currently being synthesized.

Figure 4-3A illustrates the standard curve for the quantification of purified hgDNA with 1 μm beads with LOD around 250 pg/μL, based on which the DNA concentration of seven unknown samples was measured and correlated with the results from UV-Vis spectroscopy (**Figure 4-3B**). The Bland-Altman plot (**Figure 4-3C**) shows a moderate accuracy of the PAB assay (± 0.7 ng/μL difference at 95% confidence comparing to UV-Vis).

To demonstrate the utility of the PAB assay, we used it to drive decision-making on sample choice for amplification of short tandem repeats (STRs) in a commercial PCR amplification kit used for human identification (hID). The kit (COfiler®) contains the necessary primers to facilitate multiplex amplification of tetranucleotide repeat regions at seven STR loci in the human genome; the amplified products are separated and detected via capillary gel electrophoresis. This kit (and others for human ID) is sensitive to the amount of input DNA

template, specifically, the input mass of DNA added to the PCR reaction mix must fall between 0.5 and 2.5 ng. Amplification reactions with DNA template amounts below 0.5 ng are susceptible to loss of alleles and, sometimes, complete loci ('dropout'), while template masses

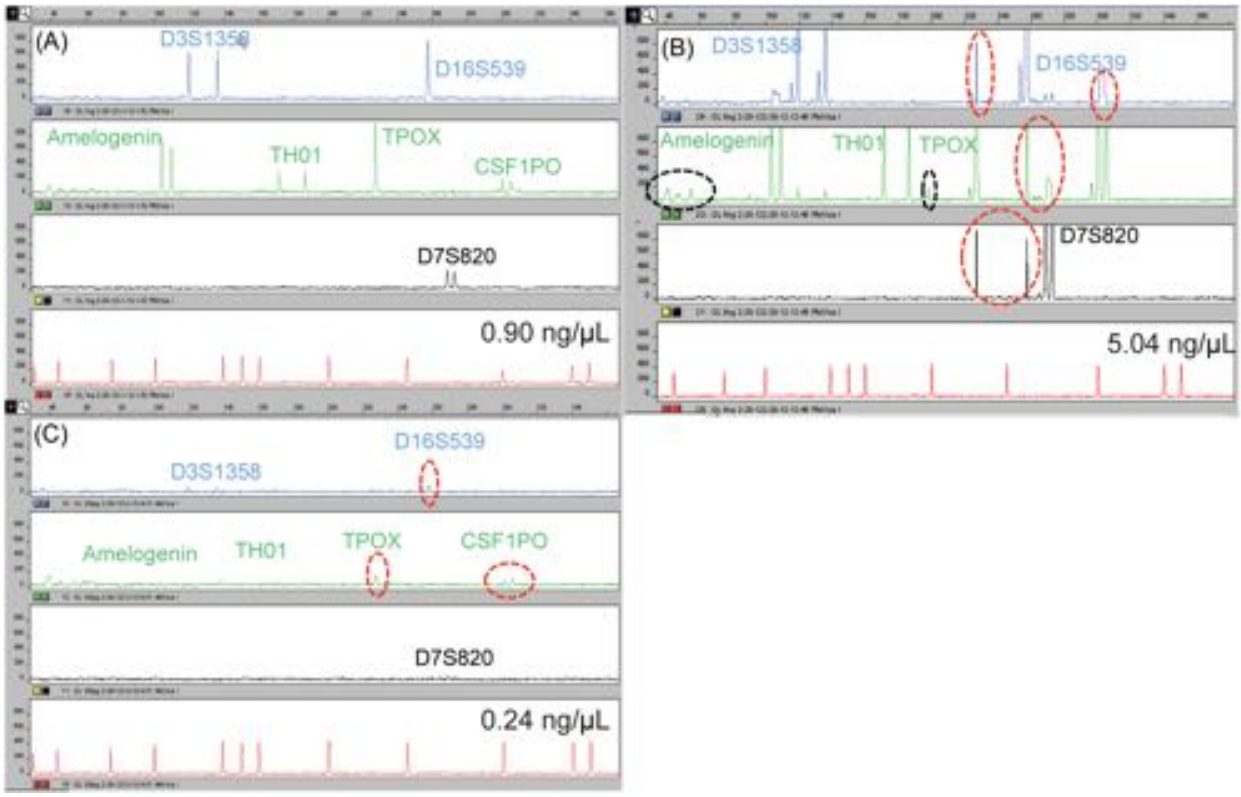

Figure. 4-4 *Results of STR amplification after DNA quantitation using the PAB assay. (A) Full STR profile (7 of 7 loci) obtained from the sample containing 0.90 ng/µl DNA. (B) Full STR profile (7 of 7 loci) obtained from the sample containing 5.04 ng/µl DNA, however, there are several additional peaks due to pull up (circled red) and non-specific amplification (circled black). (C) A partial STR profile (only 3 of 7 loci – red circles) obtained from the sample containing 0.24 ng /µl DNA, illustrating the loss of STR fragments when template DNA concentration is not within the optimal DNA range.*

above 2.5 ng can result in the amplification of non-specific products and/or a 'bleed' of signal into other colors, ('pull-up') generating extraneous peaks in the electropherogram. Both of these

scenarios hinder the ability to effectively use the profile for human ID of an individual. For

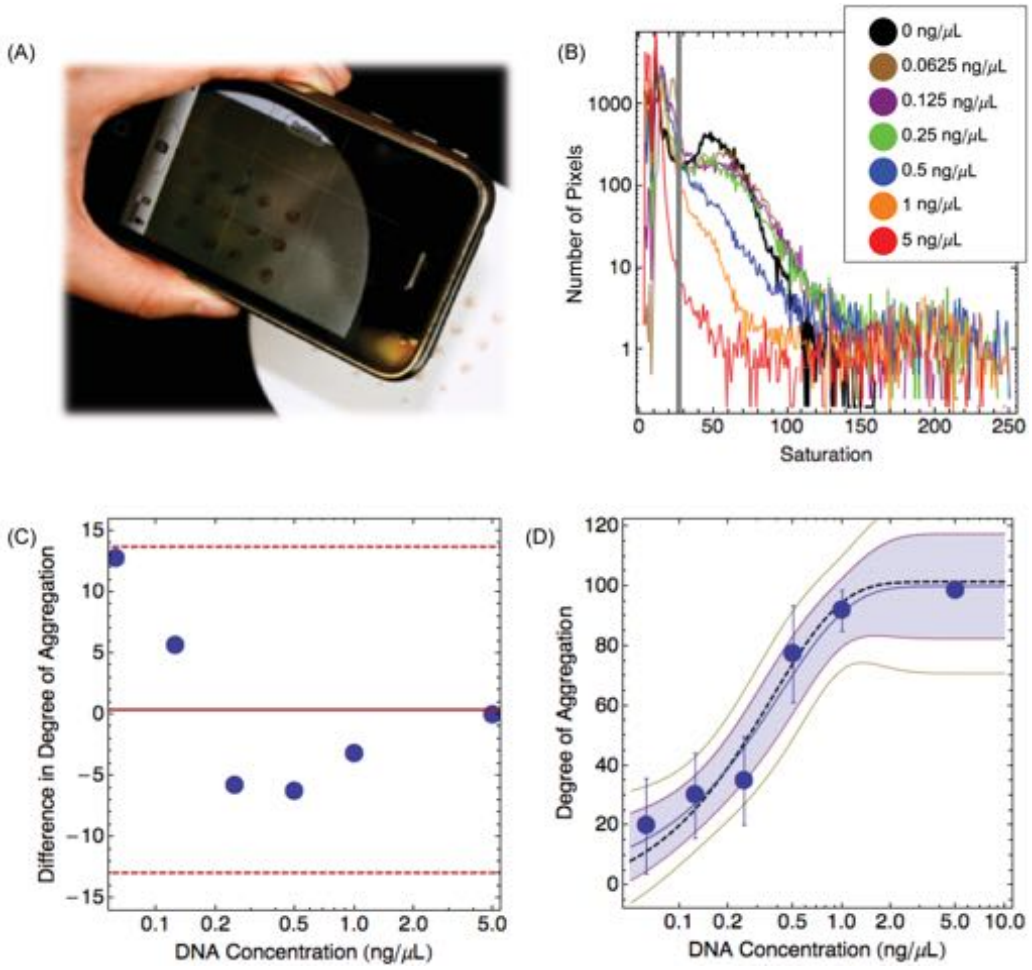

Figure. 4-5 *The PAB approach towards a portable assay for point-of-care applications. (A) The images of blotted beads on filter paper are acquired by a cell phone camera with 3 M pixels. (B) Saturation histogram illustrates the differences between the images at various DNA concentrations despite the noise generated from low image resolution. (C). The mean difference between the Degree of Aggregation values measured by the cell phone camera and scanner is shown, with 95% confidence band (red dashed lines). (D) A calibration curve is generated with the data points from cell phone camera. Error bars denote the standard deviation of four experiments. The black dashed line represents the calibration curve obtained with scanner as a comparison.*

these reasons, purified samples yielding high DNA concentrations must be diluted appropriately to fall inside the recommended template mass range.

DNA was purified from a whole blood sample using a commercial solid phase extraction kit (Qiagen). The purified DNA was diluted with TE buffer to provide a range of sample concentrations. The resultant concentration of DNA was determined by analysis of 1 μL of solution by the PAB method and the apparent DNA concentration was determined to be 5.04 ng/ μL. Based on this value, two dilutions of this sample were made; a 6X dilution yield a DNA concentration that was determined by PAB to be 0.9 ng/μL, while a further subsequent dilution (10X) yielded a DNA concentration of 0.24 ng/μL by the PAB method. These three samples spanned a range of concentrations that fall below, within and above the accepted range.

Each of these was used to input into the PCR mixture for amplification, the mass of DNA contained in a 1 μL aliquot. Results in **Figure 4-4A** show that only the sample with a putative DNA concentration of 0.90 ng/μL successfully yielded all 7 loci without interference from extraneous peaks. Excess template (5.04 ng/μL) resulted in fluorescence intensity of some peaks exceeding the dynamic range of detection, leading to inaccurate multicomponent analysis (**Figure 4-4B**), while low concentration sample (0.24 ng/μL) was inadequate for sufficient amplification, leading to allele and locus dropout (4 of 7 loci) (**Figure 4-4C**). To compare the DNA concentration values determined by PAB, UV absorbance was carried out on the original undiluted sample yielding values of 6.47 ng/μL compare to 5.04 ng/μL determined by PAB. The discrepancy is explained by Figure 2C, from which it is clear that the Dynabeads (1 μm) become saturated when the DNA concentration exceeds 3.2 ng/ μL, thus, hindering the accuracy. Although the "Pinwheel effect" is highly specific to DNA molecules, i.e. protein content does not

cause bead aggregation or interfere with the DNA adsorption onto silica[12], protein at relatively high concentrations (e.g. 3% BSA) increases the sample viscosity, and therefore, changes the blot pattern.

While we envision the PAB method as useful for rapid DNA quantification prior to genetic analysis in resource-limited areas, using it with macroscale DNA extraction via the Qiagen kit and conventional PCR-based STR analysis is not ideal (these are cumbersome and time-consuming) for cost-effective point-of-care testing. However, we believe that this demonstrates the potential utility of the PAB method as playing a role in genetic analysis. Work is underway towards a paper-based total analysis system.

Consistent with the concept of simplicity and portability, we tested a cell phone camera

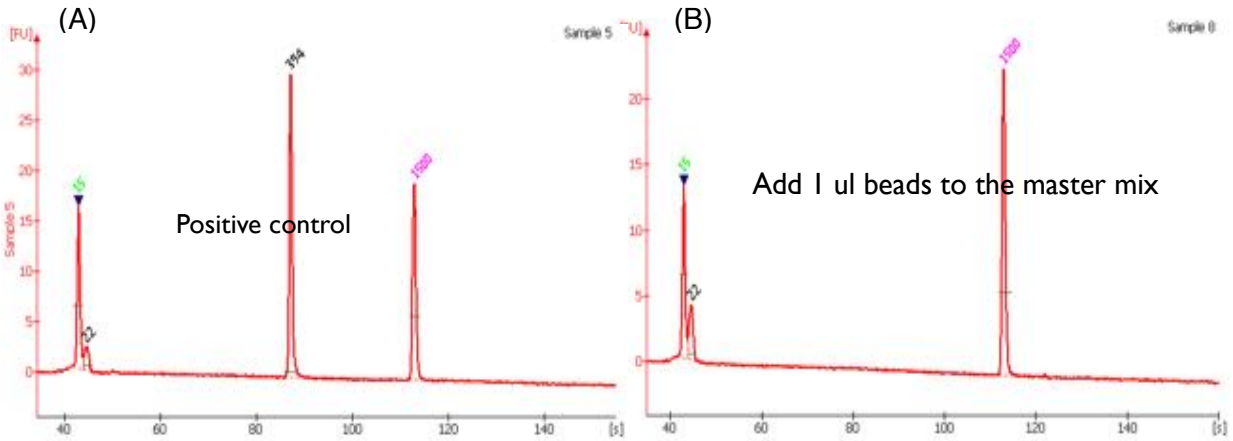

Figure 4-6. *Magensil® beads PCR test. (A) positive control (1 ng DNA). (B) The same DNA mass, 1 µl of the rinsed Magensil® beads was added to the PCR master mix. The Magensil® beads were washed thoroughly to eliminate any guanidinium chloride residue. n=3.*

as the detector (rather than a desktop photo scanner). The photo scanner generates digital images

with high resolution and consistent lighting condition, which may be challenging for cell phone camera under ambient light. The 3M-pixel camera on iPhone 3GS was used to acquire the images of aggregation on filter paper, resulting in a 18.7-fold decrease of the number of pixels per image. Although this change in digital resolution leads to failure of quantifying small aggregates represented by the noisy profile above 100 saturation (**Figure 4-5A**), the dark area values remain distinguishable at different DNA concentrations because the camera can still quantify the area of dispersed beads, which is the major contributor of dark area. The standard curve generated by the cell phone camera (**Figure 4-5B**) is comparable to the one from photo scanner (**Figure 4-2B**), denoting the feasibility of cell phone-based PAB assay. Considering the wide accessibility of cell phones worldwide, the use of cell phone camera enables a truly

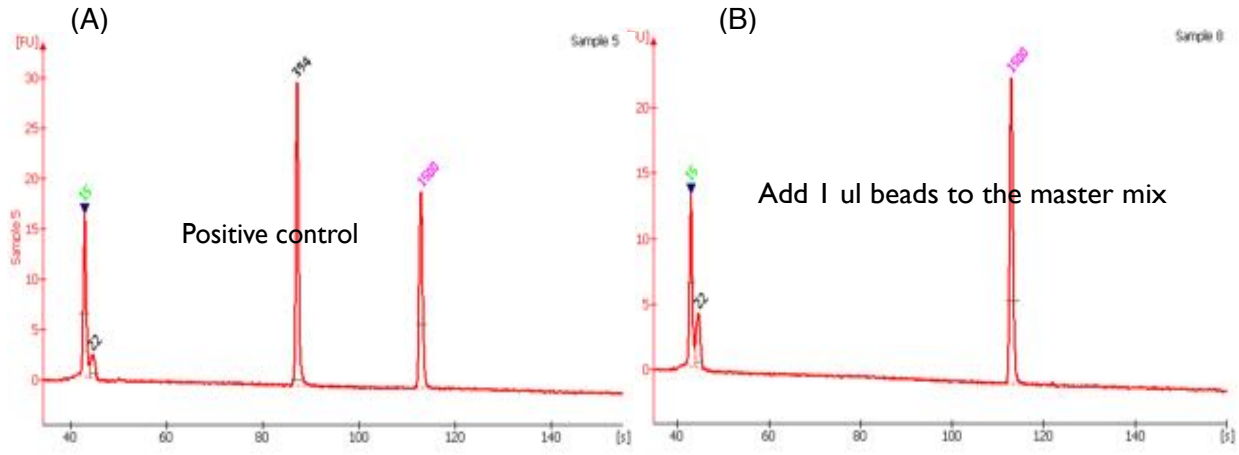

Figure 4-7. *Elute DNA from filter paper. (A) 1.5 ng DNA was was spotted on the filter paper directly, and the spotted area was punched out and added to the PCR master mix,, the PCR amplification result was negative. (B) 20 ng human genomic DNA (1 µl 20 ng/µl), the PCR amplification was successful.*

portable and cost-effective assay for the point of care.

It is important to note that similar approaches have been described in the literature, although not for DNA detection. Zhao et al. describe a colorimetric detection method using a paper-based device involving gold nanoparticle aggregation[2]. With their approach, aggregated oligo-adducted gold nanoparticles are disrupted by DNAse (or adenosine) in the sample. This augments the distance between the gold nanoparticles and, this causes a color change on paper that tracks with the DNAse activity. While the PAB assay is focused on DNA detection, it is noteworthy that it is not diffusion-based, and it exploits a magnetic field to induce bead aggregation. This shortens the reaction time by two orders of magnitude from hours to several minutes. Second, the PAB method employs a more sophisticated algorithm to interpret the images, thus providing a more quantitative analytical method.

4.4.2 Elute Polymerase Chain Reaction (PCR) Ready DNA After Quantitation

The idea is to extract and quantitate DNA via the PAB assay first, then recover the DNA from the filter paper for downstream applications such as STR profiling, sequencing, etc. Firstof all, we need to identify the PCR inhibitors involved in the PAB assay. Guanidinium chloride, used to bind DNA to the silica beads, is known to be a PCR inhibitor and can cause PCR failureeven at low concentrations [15]. To avoid these inhibitory effects, the guanidinium chloride could be washed off with 80% IPA, followed by IPA evaporation [16]. Cell debris, such as proteins and nucleases [17,18], are also known to be PCR inhibitors, given only 1 µl blood sample is used, the impact is negligible.

In order to examine whether the Magensil® beads are PCR inhibitors, a control experiment was designed. In the positive control, 1 ng of purified human genomic DNA was added to the master mix.The resulting PCR profile (**Figure 4-6 A)** shows a notable peak at 4 bp, indicating a successful amplification. In the other experiment, 1 µl of Magensil® beads were rinsed with DI water for 20 times, eliminating the guanidine chloride residue. The rinsed beads were then added to the same master mix, replacing 1 µl of nuclease free water to keep the same total volume as the positive control reaction. The resulting PCR profile (**Figure 4-6 B)** shows no peak, indicating the silica coated magnetic beads do inhibit PCR, and therefore need to be removed prior to the PCR amplification.

Another set of experiments was designed to evaluate the impact of filter paper's retention on DNA, i.e.,can we elute DNA from filter paper. In the first experiment, 1.5 ng purified human genomic DNA was blotted on the filter paper directly (no PAB assay), and the wetted area was punched out and added to the PCR master mix. The results (**Figure 4-7 A** (1 µl 1.5 ng/µl)) show no β-globin peak. When the DNA mass was increased to 20 ng, a small peak at 0 bp was seen, as shown in **Figure 4-7 B**. These results indicate that the filter paper retains DNA, and an external force is needed to help alleviate DNA from the fiber.

Based on the above mentioned information, an extraction protocol was developed. Briefly, the wetted area with aggregated beads was punched out and placed in a tube. 100 µl of 80% Isopropanol Alcohol (IPA) was added to the tube and vortexed for 10 seconds to help the DNA leave the fiber surface. Then, the solution was incubated for 15min at room temperature. This procedure was repeated 3 times. The DNA was eluted with 50 µl 0.1xTE, over a 30min incubation at room temperature. The bead residue was isolated by a magnet, and the supernatant

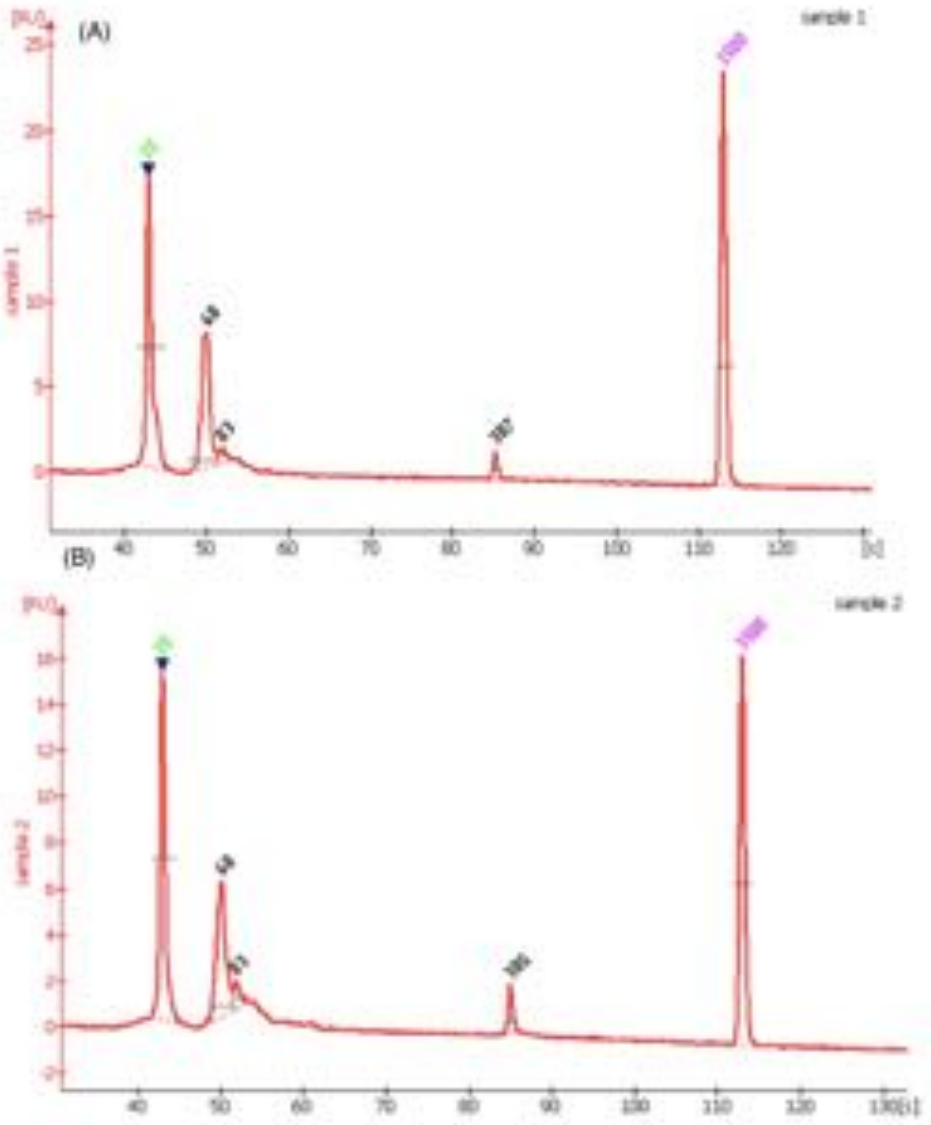

Figure 4-8. *PCR profile with different incubation condition (A) room temperature (B) 80˚C*

(16 µl remaining due to filter paper's absorption) was pipetted out and added to the PCR master mix. When the TE incubation step was carried out at an elevated temperature (80˚C), an increased peak was observed, as shown in **Figure 4-8.**

Figure 4-9 shows the PCR results from 2 blood samples, using the optimized protocol. A sample with WBC count of 6.7 cells/nl blood was first processed via the PAB assay. The original DNA mass was calculated based on the fact that per somatic cell contains 6.25 ng DNA. The

purified and quantitated DNA was eluted from the filter paper using the optimized protocol, followed by quantitation by UV-Vis nanodrop. The extraction yielded 6.6 ng DNA, with the recover rate of 15.8%, and PCR was successful (see **Figure 4-9A)**. The second sample processed had a WBC count of 2.8, yielded 4.1 ng DNA, and had a recover rate of 23.4%; however, the PCR was unsuccessful (see **Figure 4-9B)**. 6.6 ng pure DNA (sample 1) should give a much higher amplitude peak than that observed in figure 4-9A, and 2.8 ng DNA (sample 2) is more than enough for a PCR reaction. These results indicate that the DNA was not pure, and there are still PCR inhibitors.

This preliminary study recognizes the challenges of recovering DNA from the filter paper after the PAB assay. The current recover rate (~20%) is low and it could be attributed to 1) the starting DNA concentration is too high, the magnetic beads are saturated. Since we only punch out the central part with magnetic beads, the extra DNA not captured by the beads are missed. 2) The filter paper prevents DNA from eluting. Based on current efficiency and PCR results, it is unlikely that trace amount of DNA can be recovered for downstream PCR reaction. My labmate is working on skipping the quantitaion step, the idea is that we could saturate the beads and then recover the same amount of DNA each time and use it for PCR without the need for quantitation. Cellulose could be used to break down filter paper and facilitate DNA from eluting.

4.5 Concluding Remarks

The PAB assay quantifies DNA concentration in biosamples by inducing an aggregation of magnetic beads, and then immortalizing the ‘extent of aggregation’ by blotting onto filter

paper. While not as elegant as current approaches in 'paper microfluidics'[14], immortalizing the DNA-induced aggregation state on inexpensive filter paper, and then extracting quantitative information about DNA concentration from the image is, perhaps, even more rudimentary in nature. Given further development, this method has the potential to significantly lower the cost

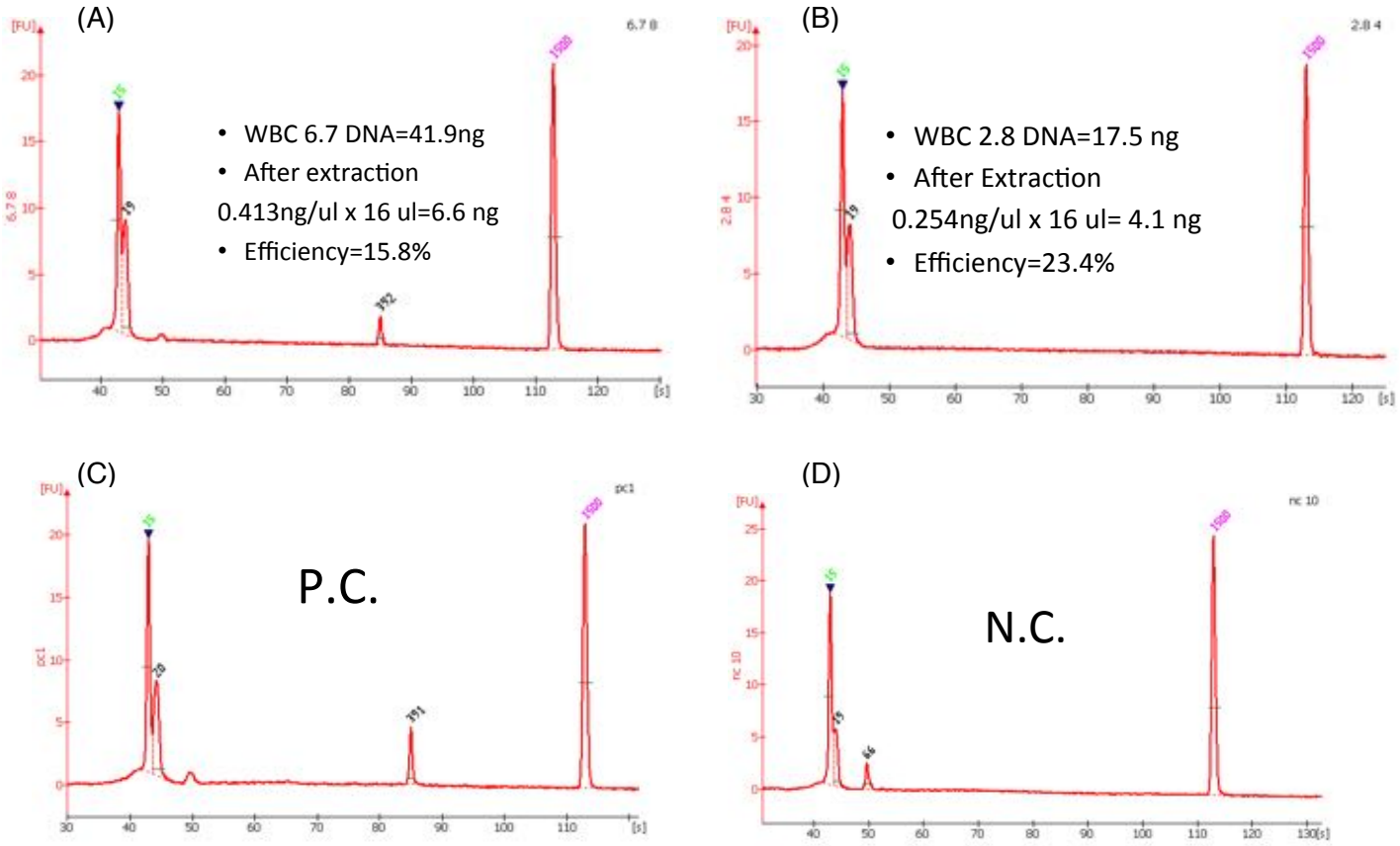

Figure 4-9 . *Optimized elution results. (A) A sample with WBC count of 6.7 cells/nl blood was processed by the PAB assay, and the purified and quantitated DNA was eluted from the filter paper, the eluted DNA was quantitated by UV-Vis nanodrop, the recovery yield was calculated to be 15.8%, PCR was successful. (B) A sample with WBC count of 2.8. the recovery yield was 23.4%, the PCR was unsuccessful. (C) Positive control, 1 ng pure DNA for PCR . (D) Negative control, no DNA.*

of DNA quantification by eliminating instrumentation and, in cases where fluors are employed, circumvents the cost associated with those reagents (and more sophisticated instrumentation).

In conclusion, we present a simple, portable, and label-free lab-on-paper assay for DNA quantification, which can be further combined with paper-based DNA extraction method and microfluidic PCR for sample-to-result genetic analysis at the point of care. Since the filter paper and magnetic beads can be readily functionalized, thoughtfully designed surface modification will bring great versatility to this approach, and quantitative assays for a variety of targets can be developed.

4.6 References

1. M. M. Mentele, J. Cunningham, K. Koehler, J. Volckens and C. S. Henry, Microfluidic paper-based analytical device for particulate metals. ***Anal Chem***, 2012.
2. J. Lankelma, Z. Nie, E. Carrilho and G. M. Whitesides, Paper-based analytical device for electrochemical flow-injection analysis of glucose in urine. ***Anal Chem***, 2012.
3. W. A. Zhao, M. M. Ali, S. D. Aguirre, M. A. Brook and Y. F. Li, A Mixed Stimuli-Responsive Magnetic and Gold Nanoparticle System for Rapid Purification, Enrichment, and Detection of Biomarkers. ***Anal Chem***, 2008, 80, 8431-8437.
4. A. W. Martinez, S. T. Phillips, E. Carrilho, S. W. Thomas, H. Sindi and G. M. Whitesides, ***Anal Chem***, 2008, 80, 3699-3707.
5. A. C. Araujo, Y. Song, J. Lundeberg, P. L. Stahl and H. Brumer, 3rd, ***Anal Chem***, 2012, 84, 3311-3317.

6. A. V. Govindarajan, S. Ramachandran, G. D. Vigil, P. Yager and K. F. Bohringer, ***Lab on a chip***, 2012, 12, 174-181.
7. P. J. Asiello and A. J. Baeumner, ***Lab on a chip***, 2011, 11, 1420-1430.
8. S. Park, Y. Zhang, S. Lin, T. H. Wang and S. Yang, ***Biotechnol Adv***, 2011, 29, 830-8.
9. Y. H. Zhang and P. Ozdemir, ***Anal Chim Acta***, 2009, 638, 115-125.
10. D. C. Leslie, J. Li, B. C. Strachan, M. R. Begley, D. Finkler, L. A. Bazydlo, N. S. Barker, D. M. Haverstick, M. Utz and J. P. Landers, ***Journal of the American Chemical Society***, 2012, 134, 5689-5696.
11. D. S. Lee, B. G. Jeon, C. Ihm, J. K. Park and M. Y. Jung, ***Lab on a chip***, 2011, 11, 120-126.
12. D. C. Leslie, J. Y. Li, B. C. Strachan, M. R. Begley, D. Finkler, L. A. L. Bazydlo, N. S. Barker, D. M. Haverstick, M. Utz and J. P. Landers, ***Journal of the American Chemical Society***, 2012, 134, 5689-5696.
13. J. Li and J. P. Landers, ***Proceedings of The 15th International Conference on Miniaturized Systems for Chemistry and Life Sciences***, 2011, 1956-1958.
14. Andres W. Martinez, Scott T. Phillips and George M. Whitesides. ***Anal Chem***,2010, 82,3-10.
15. Bessetti, J. ***Profiles in DNA*** 2007, 10, 9-10.
16. Reedy *et al.* Solid phase extraction of DNA from biological samples in a post-based, high surface area poly(methyl methacrylate) (PMMA) microdevice. ***Lab on a Chip***. 2011,11(9):1603-11

17. Coolbear, T., Eames, C. W., Casey, Y., Daniel, R. M. and Morgan, H. W. ***Journal of Applied Bacteriology*** 1991, *71*, 252-264.

18. Coolbear, T., Whittaker, J. M. and Daniel, R. M. ***Biochemical Journal*** 1992, *287*, 367-374.

Chapter 5: Preparation, Characterization of Fe_3O_4@SiO_2 Core−Shell Microspheres and Its Applications on Sensitive DNA Quantification

5.1 Overview

DNA and silica-coated magnetic particles entangle and form visible aggregates under chaotropic conditions with a rotating magnetic field, in a manner that enables quantification of DNA by image analysis. As a means of exploring the mechanism of this DNA quantitation assay, nanoscale SiO_2-coated Fe_3O_4 ($Fe3O_4$@SiO_2) particles are synthesized via a solvothermal method. Characterization of the particles define them to be ~200 nm in diameter with a large surface area (141.89 m2/g), possessing superparamagnetic properties and exhibiting high saturation magnetization (38 emu/g). The synthesized Fe_3O_4@SiO_2 nanoparticles are exploited in the DNA quantification assay and, as predicted, the nanoparticles provide better sensitivity than commercial microscale Dynabeads® for quantifying DNA, with a detection limit of 4 kilobase-pair fragments of human DNA. Their utility is proven using nanoparticle DNA quantification to guide efficient PCR amplification of short tandem repeat loci for human identification.

5.2 Introduction

The synthesis of functional nanoparticles has led to numerous technologies that can be applied to a wide spectrum of applications, including protein/cell separation and sorting, magnetic fluid hyperthermia (MFH), drug delivery, and magnetic resonance imaging (MRI) [1].

A number of methods have been described for synthesizing magnetic nanoparticles for biomedical application. Co-precipitation is the simplest technique and is the most common utilized to synthesize magnetic nanoparticles using metal salts[2-5]. With this approach, a large mass of magnetic nanoparticles can be synthesized simultaneously. In general, the Fe(III)/Fe(II) ratio is maintained at 2 in an alkaline solution, and consequently yields superparamagnetic iron oxide nanoparticles (SPIONs) below 20 nm in diameter. However, this method generally offers limited control over the size distribution of the particles and, as a result of the polydispersity, often requires a size screening process to obtain relatively uniform sized particles.

Microemulsion is another widely-used approach [6-8], and it produces very uniform particles (<10% variability). However, the magnetic nanoparticles produced with this method are only soluble in non-polar solvents, significantly restricting their biological application. Li's group recently developed a solvothermal reduction method to synthesize monodispersed magnetic particles with excellent water solubility and narrow size distribution[9]. The resultant 'magnetite' particles ranged from 80 nm to 410 nm, depending on the ratio of different reagents used in the synthesis.

DNA quantification is normally carried out by spectrophotometric analysis, fluorescence dye-assisted detection, or real time PCR. The use of UV spectroscopy to quantitate DNA is decades old [10] and measures the absorbance of light by the sample at 260 nm; it exploits Beer's law ($A=\varepsilon cl$), where ε is the molar absorption coefficient, c is the concentration, and l is the light path length. However, the presence of RNA, single stranded DNA (ssDNA), and impurities (e.g., proteins and phenols) may significantly affect the final reading and lead to a bias in DNA concentration estimates. Fluorescence-assisted assays [11] and real time PCR [12] have

been more recently developed, and offer a significant sensitivity enhancement, with increased laboratory efficiency due to the high-throughput format of the fluorometers. However, the drawback is that expensive reagents and sophisticated hardware are required.

We have recently reported the "pinwheel assay"[13], a novel DNA quantification method that exploits the ability of DNA to aggregate silica-coated magnetic particles in a magnetic field ; the extent of aggregation reflects the mass of DNA in the sample. A more portable and cost-effective paper-based approach was reported later, the 'Pipet, Aggregate and Blot (PAB)' approach [14]. While not extensively studied, it appears that DNA binds to silica beads in an entropically-driven process in a high concentration chaotrope environment, [15] however, we have not yet elucidated the mechanism underlying aggregation. We have observed that longer strands of DNA induce bead aggregation more effectively than shorter ones.[13] Our current hypothesis is that DNA strands adsorb on the silica surface initially, but exposure to a rotating magnetic field accelerates a 'winding' or 'entangling'of the DNA around the particles, much like DNA around histones [16]. Whether this is simply a 'mixing' issue is yet to be determined. We can rationalize this in terms of scaling. With each base pair in a double helical strand spanning 0.34 nm [19], a 100 Kb fragment has a length of 34 μm, an adequate length to entangle with 1μm beads. Consequently, particles with a smaller diameter would have the ability to entangle with shorter DNA fragment and result in better sensitivity.

Here, we report the synthesis of Fe_3O_4@SiO_2 nanoparticles with a sol-gel silica coating via solvothermal reduction. At ~200 nm (±74) compared with the ~1 μm particles used before, these nanoparticles are capable of detecting substantially shorter fragments of DNA. To the best

of our knowledge, this is the first report of magnetic nanoparticles being applied to DNA quantification.

5.3 Materials and Experimental Methods

5.3.1 Synthesis of Fe_3O_4 Particles

The magnetite core was synthesized through a solvothermal reaction [21]. Briefly, $FeCl_3.6H_2O$ (2.70 g, 0.01 mol) was dissolved in ethylene glycol (100 mL), and then sodium acetate (7.30 g, 0.09 mol) was added under vigorous stirring. The resulting yellow liquid was transferred to an aluminum autoclave with Teflon inner vessel, and the autoclave was heated to 200 °C. After 8-9 hours, the autoclave was taken out and cooled to room temperature; the resulting black solution was separated, washed with ethanol and water several times, and then

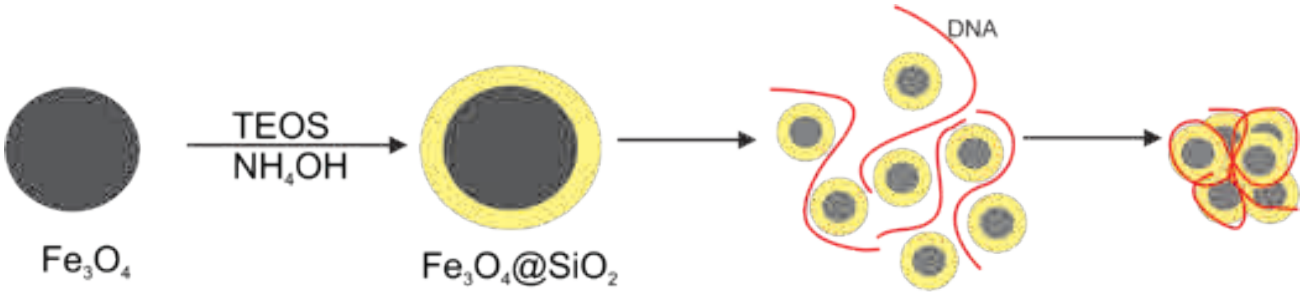

Figure 5-1. *The Fe_3O_4@SiO_2 nanoparticles are synthesized by a solvothermal reaction. Combining DNA strands and Fe_3O_4@SiO_2 nanoparticles form aggregate under rotating magnetic field in chaotropic environment, the aggregate size correlate closely with the DNA concentration, and DNA quantification is realized by simple image analysis.*

dried in vacuum oven at 60 °C for 8 hours.

5.3.2 Synthesis of Fe_3O_4@SiO_2 Particles

The magnetite was coated with SiO_2 by StÖber reaction [22]. Briefly, synthesized magnetite (0.10 g) was first treated with HCl (50 mL, 0.1 M) in sonicator for 10 min. The Fe_3O_4 particles were collected by magnets and washed with deionized water several times. The cleaned particles were then dispersed in a mixture of ethanol and deionized water totaling 100 mL (4:1 v/v). Concentrated ammonia solution (1.0 mL, 28 wt%) was added to the solution under vigorous stirring, followed by the addition of tetraethyl orthosilicate (TEOS; 0.03 g, 0.144 mmol). After 6 hours of stirring at room temperature, the Fe_3O_4@SiO_2 particles were separated and washed with

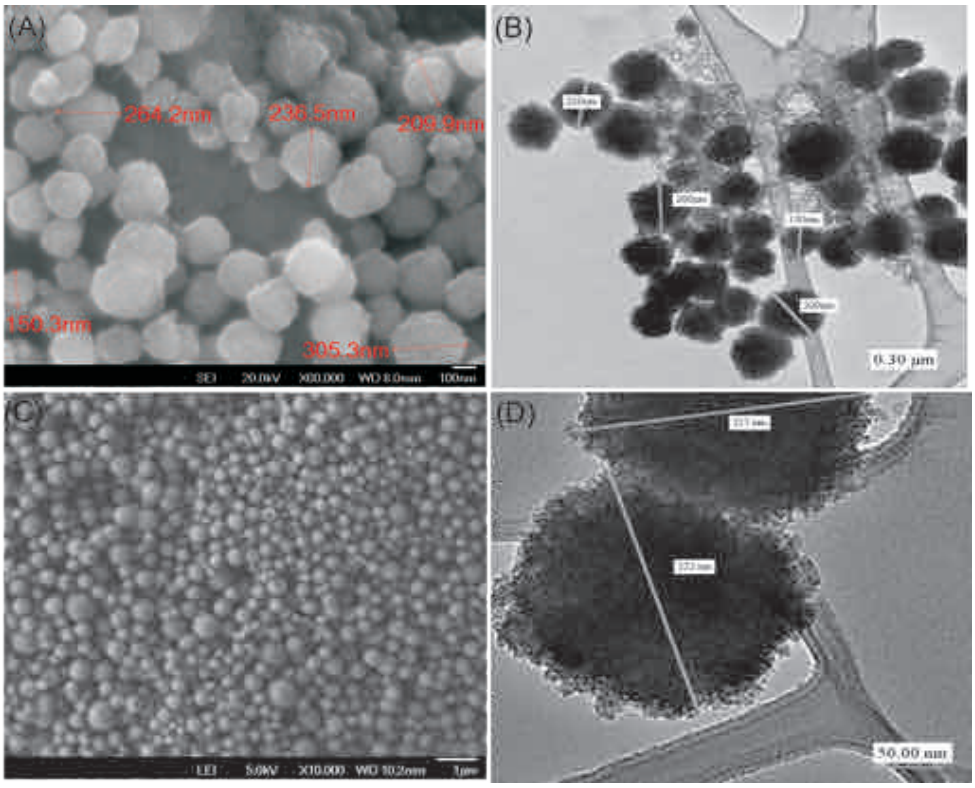

Figure 5-2. *Morphological characterization. (A) SEM image of sythesized Fe_3O_4 nanoparticles. (B) TEM image of synthesized Fe_3O_4 nanoparticles. (C) SEM image of Fe_3O_4@SiO_2. (D) TEM image of Fe_3O_4@SiO_2*

ethanol and deionized water, and dried in vacuum oven at 60 °C for 8 hours. The resulted powder was dissolved in deionized water at 8 mg/mL and ready to use.

5.3.3 Image Processing

Images of each dispensed area were cropped from the original photo in TIF format. The images were imported into Mathematica in HSB (hue-saturation-brightness) mode, and the saturation data was extracted for further analysis. An isodata algorithm written in Mathematica was applied to the saturation data of negative controls (beads without DNA), and it defined a threshold for all the images, above which the pixels represent the beads and aggregates. The total number of these pixels in each image (i.e., dark area) was normalized to the negative controls, and correlated with DNA concentration.

5.3.4 STR Analysis

STR analysis was performed according to manufacturer's instruction. Briefly, DNA samples were amplified using the AmpFlSTR COfiler kit reagents, and the PCR products were separated on ABI PRISM 310 Genetic Analyzer, which generates electropherograms for further interpretation. 1 μm Dynabeads® MyOne™ SILANE was bought from Life Technologies, they have an optimized silica-like surface chemistry and a high specific surface area. Buccal swabs were collected from anonymous, healthy volunteers by using an Institutional Review Board (IRB) approved collection method. Swabs were obtained by vigorously rubbing inside both cheeks with a sterile cotton swab for 30 s each. All experiments were performed in compliance

with IRB #12548 as approved by the University of Virginia Health System, with informed consent obtained from all volunteers.

5.4 Results and Discussion

5.4.1 Structural and Morphological Characterization

In order to characterize the synthesized magnetite and Fe_3O_4@SiO_2 nanoparticles, scanning electron microscope (SEM) and transmission electron microscope (TEM) images were obtained. Images from both microscopic approaches are given for both Fe_3O_4 (**Figure 5-2A** SEM, **Figure 5-2B**-TEM) and Fe_3O_4@SiO_2 (**Figure 5-2 C**-SEM, **Figure 5-2D**-TEM). The silica-coated magnetite nanoparticles were monodisperse and spherical in shape, with an average

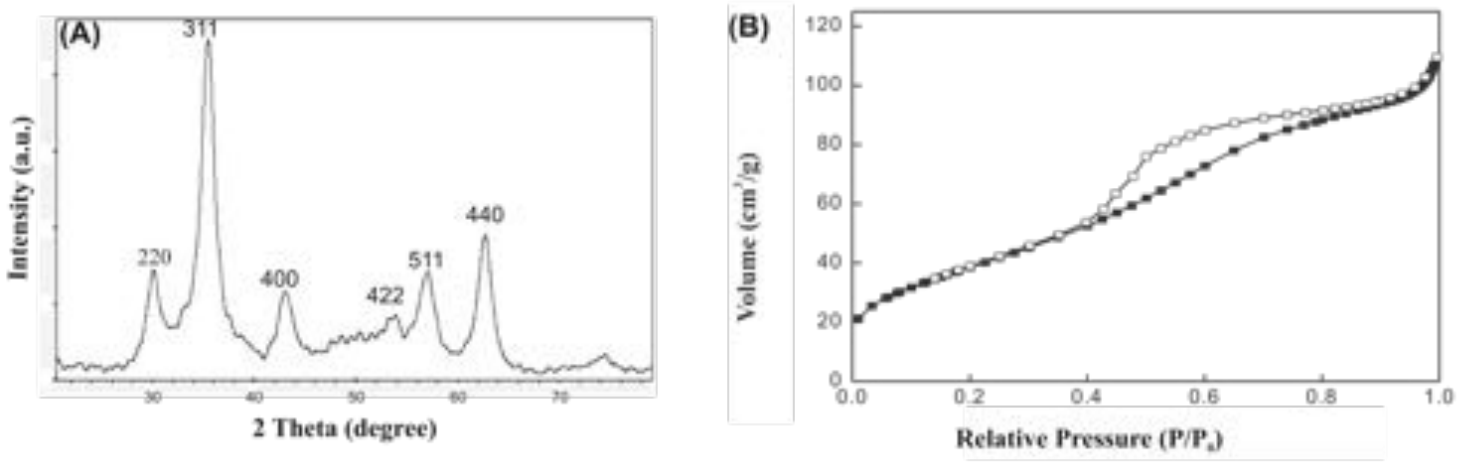

Figure 5-3. *(A) XRD pattern of Fe_3O_4@SiO_2. (B) N_2 sorption isotherms and pore size distribution (inset) of Fe_3O_4@SiO_2*

diameter of 200±74 nm, while dynamic light scattering results indicated a size of 149±17.5 nm. The silica shell was determined to be ~10 nm (**Figure 5-2D**).

Figure 5-3A shows the XRD patterns of Fe_3O_4@SiO_2 (X' pert powder X-ray diffractometer). The diffraction peaks can be indexed as a face-centered cubic Fe_3O_4 phase (JCPDS card 19-629), the presence of Si in energy-dispersive X-ray (EDX) spectrum (Figure 5-4), and the absence of Si in XRD indicates the presence of SiO2 in an amorphous phase. The specific surface area was measured by nitrogen sorption and analyzed according to the Brunauer-Emmett-Teller (BET) theory [17] (**Figure 5-3B**); the nanoparticles exhibited a typical type IV isotherm and H4 hysteresis loop, indicating the presence of mesopores. The mesopore size of the particles was analyzed via the Barrett-Joyner-Halenda (BJH) adsorption pore distribution model (**Figure 5-5**). The Fe_3O_4@SiO_2 microspheres have a specific surface area of 142 m^2/g.

The magnetic properties of the nanoparticles were measured from 50 K to 300 K with a vibrating sample magnetometer (Quantum Design VersaLab). The M-H hysteresis loop at 300 K indicates the superparamagnetic property of the Fe_3O_4@SiO_2 nanoparticles (**Figure 5-6A**). The saturation magnetization at 300 K was 38 emu/g. Figure 5-6B shows the zero-field-cooled and field-cooled (ZFC/FC) curves of the synthesized Fe_3O_4@SiO_2 nanoparticles measured at temperatures between 50 and 275 K with an applied field of 100 Oe. As the temperature rises from 50 to 275 K, the ZFC magnetization increases, and then decreases after reaching a maximum at 118 K, which corresponds to the blocking temperature (TB)[18]. Magnetic nanoparticles are known to exhibit superparamagnetism beyond the blocking temperature, which supports the fact that the Fe_3O_4@SiO_2 nanoparticles display a superparamagnetic behavior at room temperature. Moreover, the Fe_3O_4@SiO_2 nanoparticles disperse well in water aided by

vortexing or sonication (**Figure 5-6C**); within 30 seconds of the application of an external

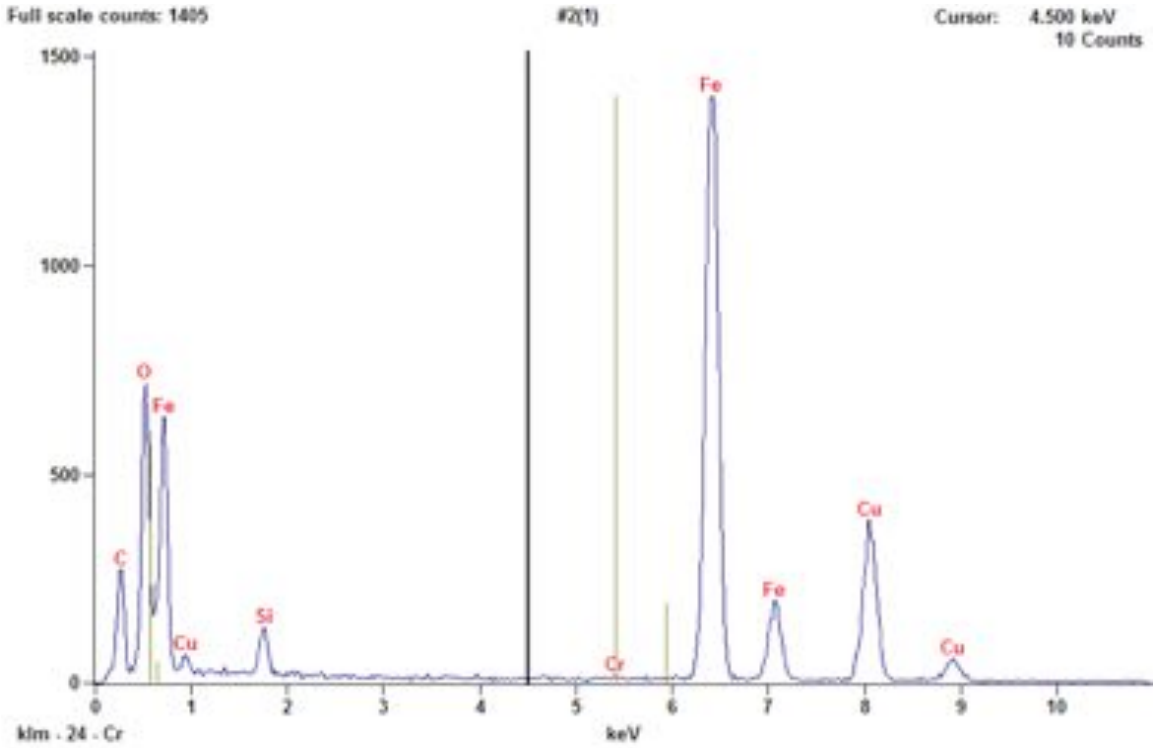

Element Line	Net Counts	Int. Cps/nA	K-Factor	Weight %	Weight % Error	Atom %	Atom % Error
C K	1925	---	12.510	34.29	+/- 0.89	60.11	+/- 1.56
O K	4325	---	2.604	16.04	+/- 0.52	21.11	+/- 0.69
Si K	1118	---	1.000	1.59	+/- 0.07	1.19	+/- 0.06
Si L	0	---	---	---	---	---	---
Cr K	79	---	1.013	0.11	+/- 0.03	0.05	+/- 0.01
Cr L	1376	---	---	---	---	---	---
Fe K	23751	---	1.070	36.20	+/- 0.35	13.65	+/- 0.13
Fe L	6768	---	---	---	---	---	---
Cu K	6606	---	1.251	11.76	+/- 0.26	3.90	+/- 0.08
Cu L	354	---	---	---	---	---	---
Total				100.00		100.00	

Figure 5-4. *EDX data of the Fe_3O_4@SiO_2 nanoparticles, the elements Cu, Cr and C are from the grid.*

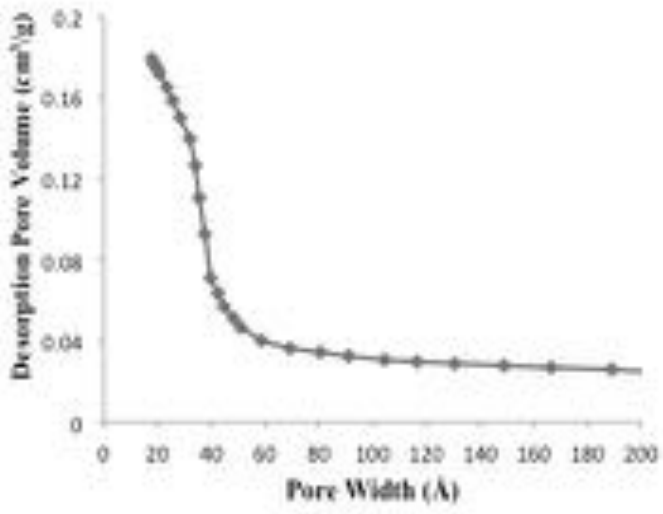

Figure 5-5. *The mesopore size distribution of the particles analyzed via the Barrett-Joyner-Halenda (BJH) adsorption pore distribution model.*

magnet, the nanoparticles rapidly collect at the magnet, but are readily redispersed after the magnet is removed aided by gentle shaking.

5.4.2 Quantification of DNA Using Nanoparticle Blotting on Filter Paper

We have recently reported the 'pipette, aggregate, and blot' (PAB) approach as a new label-free 'lab-on-paper' assay for DNA quantification based on the magnet-induced aggregation of silica-coated microbeads. The PAB assay protocol includes 1 μL of of magnetic particles [either the synthesised nanoparticles or the commercial Dynabeads® (the control experiment; preparation method described elsewhere [14])] in 6M guanidinium hydrochloride solution and 1 μL of DNA sample. The aggregates are formed in the pipet tip after serially pipetting of the beads (in GdnHCl) and the DNA sample, then exposed for 40 seconds to a rotating magnet. Finally, the contents of the pipette tip are dispensed (blotted) on filter paper. The attractiveness of this approach is its simplicity, utilizing common laboratory hardware (a pipette, a magnet) and simple materials (guanidine, filter paper), the PAB assay offers an uncomplicated and cost-

effective alternative for DNA quantification. The aggregation on filter paper is visually striking, and allows for a simple qualitative (yes or no) analysis. Where more quantitative results are desired, a standard, inexpensive document scanner was used to capture the image of the focal spots, which could be analyzed (immediately or at some later time) by a non-complex algorithm that generated a value for the pixels associated with the aggregated area. One of the interesting characteristics of the PAB result is that, unlike the 'pinwheel' aggregation result obtained in solution and stable only as long as the magnetic field is applied[13], the filter paper provides an intact, immobilised representation of the DNA from that sample. This is tantamount to the semiquantitative slot blot result originally used in forensic DNA analysis[23], that could be stored for record. The thorough study of the stability of the image has not be carried out, but at a minimum, the image is stable for 6 months at room temperature. As a result, we not only have the captured image of the blot, we actually have the immobilised and storable form of the sample

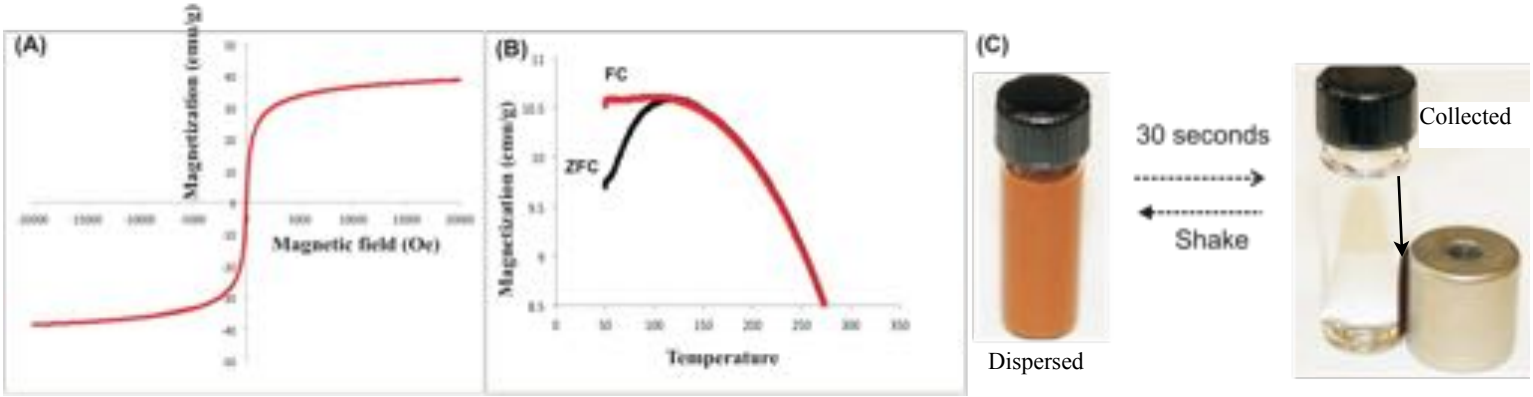

Figure 5-6. *Magnetic properties of Fe_3O_4@SiO_2 (A) Room-temperature (300 K) magnetic hysteresis loops of Fe_3O_4@SiO_2 (B) ZFC-FC curve of Fe_3O_4@SiO_2 indicating a blocking temperature of 118 K (C) Magnetic separation−redispersion process*

DNA; efforts are currently underway to define how the DNA could be extracted for PCR at a later time. With further development, a cell phone could be used as the modality for data acquisition, transmission and analysis.

The goal here is to extend the capabilities of the PAB DNA quantitation approach but using synthesized magnetic nanoparticles to create a nanoPAB assay. The nanoparticles are 5-fold smaller in diameter and, therefore, should be more sensitive if the proposed 'pinwheel' mechanism is legitimate, i.e., DNA strands bind to silica-coated particles and are entwined when

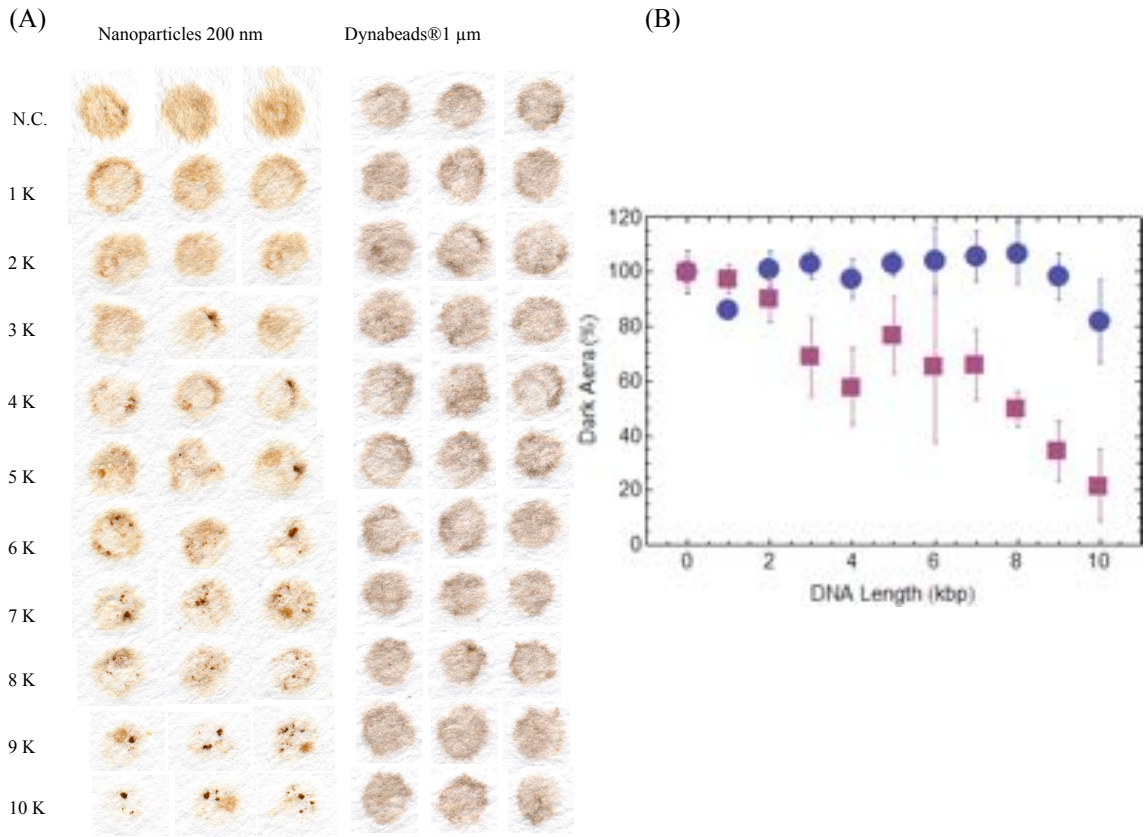

Figure 5-7*. Comparison of synthesized Fe_3O_4@SiO_2 nanoparticles and Dynabeads® in quantification of DNA. (A) Original data (B) Information extracted by the algorithm. Nanoparticles show a decreasing trend in Dark Area% upon increasing DNA length, while Dynabeads® does not respond up to 10kb. Dark Area defines the pixels that make up the brown area. Dark Area% is normalized by negative control (N.C.), which contains no DNA.*

the rotating magnetic field is applied. To test this, a series of purified DNA fragments (ranging in size from 1-10 Kilobase (Kb)) were exposed individually to both the commercial micron-scale beads (Dynabeads®)(PAB) and the newly synthesized magnetic nanoparticles (nanoPAB) under the appropriate chemical conditions. Figure 5-7A indicates that the reproducible visual detection limit with nanoPAB was 4Kb, with more extensive aggregation seen with longer DNA strands. In contrast, no reproducible aggregation could be observed with any length of DNA up to 10Kb using PAB and the commercial 1 μm beads. **Figure 5-7B** illustrates the quantitative information extracted from **Figure 5-7A** using an in-house algorithm, with the extent of aggregation represented as % Dark Area (%DA; low %DA = extensive aggregation). Knowing that the length of 1 base pair in helical DNA is 0.34 nm[19] and the detection size limit for aggregation with a 200 nm nanoparticle was 4Kb, the minimum DNA length to induce aggregation is

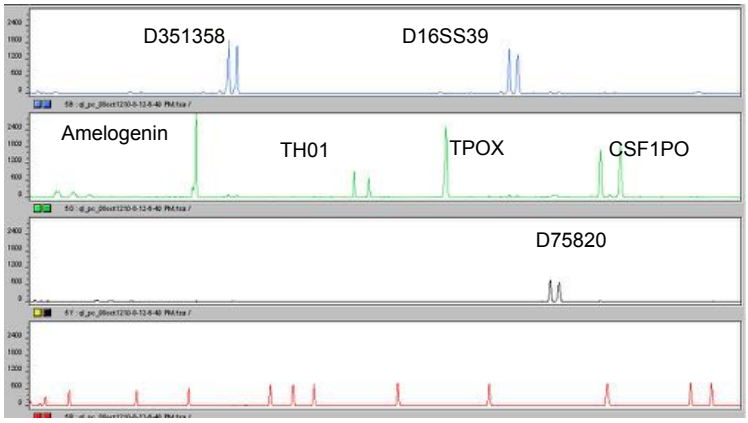

Figure 5-8. *1.0 ng of Control DNA 9947A amplified with the COfiler® Kit and analyzed on the capillary electrophoresis with 4-color detection.*

calculated to be ~1360 nm, ~7 times the diameter of the particle. Based on this data, the speculative detection limit for the commercial 1 μm beads would be 20 Kb.

Silica surface is embedded with hydroxy groups and ethereal linkages, and generally considered as negatively charged, prone to adsorption of electron deficient species. It has been shown that cationic and nonionic surfactants adsorb on silica surface involving hydrogen bonding [29], however, the phosphate groups at DNA backbone is also considered as negatively charged, it was speculated that the guanidinium chloride provides shield between DNA and silica, overall, (i) shielded intermolecular electrostatic forces, (ii) dehydration of the DNA and silica surface and (iii) intermolecular hydrogen bond formation in the DNA silica contact layer are the major contributing driving force for adsorption [30].

5.4.3 Guiding Template Load in Short Tandem Repeat (STR) Amplification

Depending on the sequences targeted for amplification by PCR and the number of amplicons involved, PCR amplification can be finicky, and the amplification efficiency adversely affected if the 'optimal' template mass is not provided. For this reason, some PCR amplifications are preceded by DNA quantification following purification of the DNA from the sample; the method of choice for this is often qPCR. One such example of this is the amplification of seven DNA sequences in the human genome using a commercial kit (AmpFl STR® COfiler®), that has been used in human identification. These include one gender marker (Amelogenin) and six tetra-nucleotide repeat sequences (D3S1358, TPOX, CSF1PO, D7S820, D16S5, and TH01). As described previously[14], if template DNA mass falls outside of the optimal input mass of 0.5 - 2.5 ng, the efficiency of the amplification is adversely affected and this is visible in the subsequent DNA profile generated by capillary electrophoresis with multicolor fluorescent detection. Figure 5-8 shows an ideal DNA profile generated by PCR with

input of 1.0 ng of control DNA 9947A provided in the kit, and analyzed by capillary electrophoresis with 4-color detection. All of the expected loci fragments were generated by PCR with a peak height threshold and peak balance that is comparable to that used in forensic

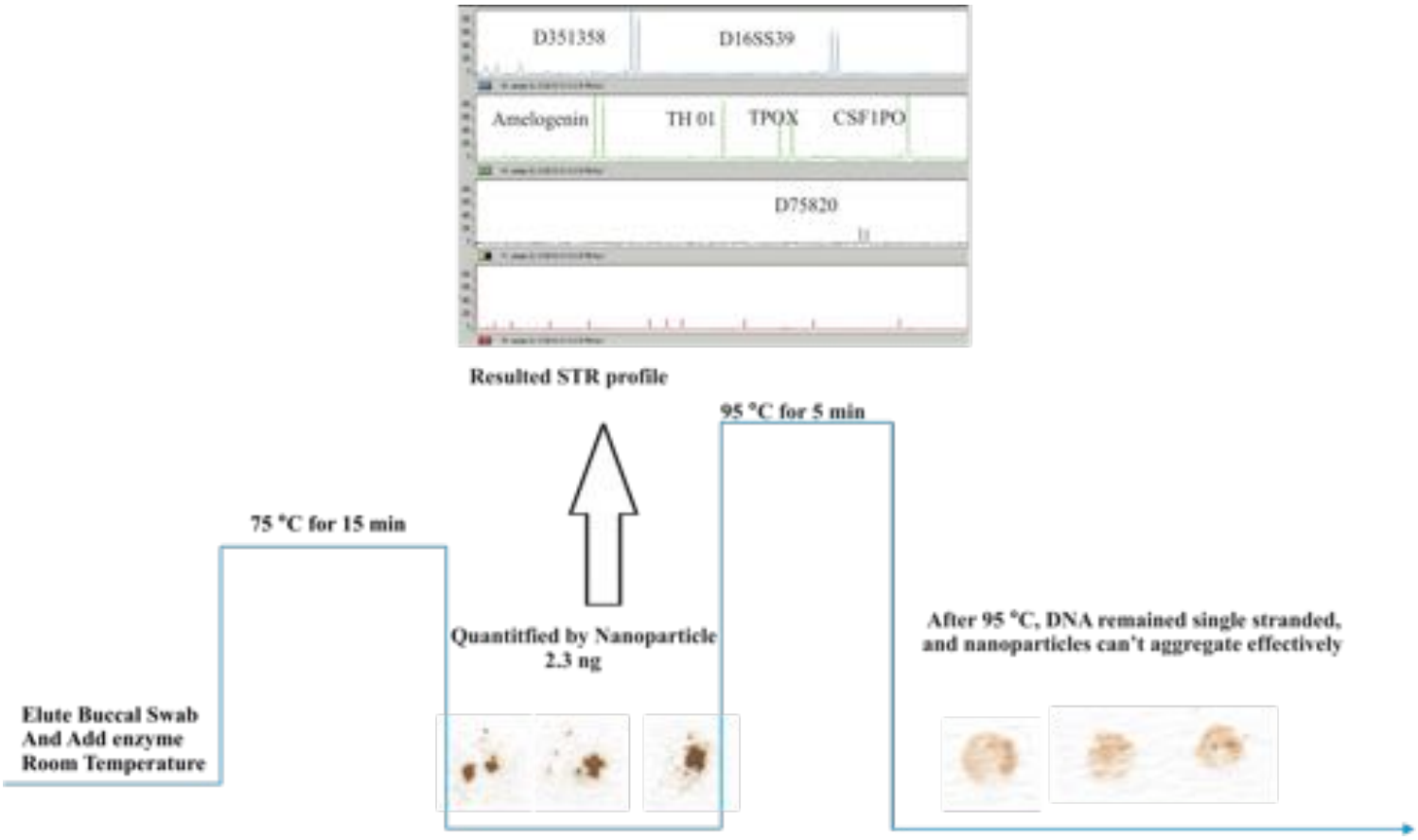

Figure 5-9*. The flow chart of the Zygem extraction-nanoparticle quantification-STR procedure. DNA quantification was carried out before 95˚C, so that DNA remain double stranded.*

laboratories. To test whether nanoparticle DNA quantitation could guide DNA template mass added to a PCR mixture for amplification, the commercial kit was used in conjunction with the rapid quantification of DNA extracted from buccal swabs, the metric used to define success was the presence of all loci peaks, and peaks with acceptable peak height.

The DNA utilized for these experiments was not obtained through standard solid phase extraction[24], but from buccal swab cells using an enzymatic DNA extraction system (prepGEM™ Saliva). This is a commercial liquid-based DNA preparation method that exploits the protein-degrading activity of an extremophile proteinase from an Antarctic Bacillus sp. EA1.

The enzyme activity induces lysis of cells and degrades proteins (including nucleases) while leaving the nucleic acids intact. This yields PCR-ready DNA in <25 minutes, providing an efficient and effective method for DNA extraction. Since the enzyme-extracted DNA is still associated with all of the cellular remains (although degraded), it cannot be quantified by UV spectroscopy due to high protein content, leaving qPCR — reagent intensive and costly instrumentation — as the method of choice for quantitation. Having defined that protein content does not interfere with DNA adsorption to the silica or cause bead aggregation,[13] the nanoPAB assay is ideal for quantitating enzyme-treated samples.

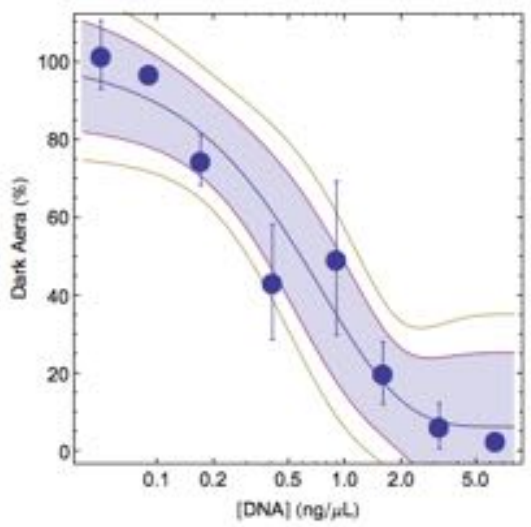

Figure 5-10. *Standard curve. The degree of aggregation values were correlated with DNA concentration obtained from PicoGreen® fluorescence quantitation. Error bars denote standard deviation (n=3), with the 95% (purple lines) and 99% (golden lines) confidence intervals.*

Prior to testing the ability of the nanoPAB assay to quantify DNA in buccal swabs from different sources, we needed to assure the integrity of the DNA resulting from the 'enzyme extraction process'. It has been established that the enzyme-extracted DNA is PCR ready.[25] However, one must be cognizant of the fact that

PCR can be effective even with relatively degraded DNA.[26] The effectiveness of bead aggregation with 'enzyme-extracted' DNA had not been shown and, given that there is a size-dependence on aggregation, this needs to be explored. Of particular concern were the elevated temperatures for enzyme activation (75 ºC) and enzyme denaturation (95 ºC) (unlike conventional solid phase extraction which is carried out at room temperature), where either heat-induced cleavage[27] or incomplete renaturation of the DNA could affect aggregation. In summary, aggregation was effective after the 75 ºC step but not the 95 ºC step. Heat-induced cleavage of the DNA at 95 ºC is possible,[27] but it is unlikely that it could be so extensive as to induce the result. It is more likely that the fact that the DNA does not completely return to a

Table 5-1. *nano*PAB quantitation of 5 DNA samples, predicted and observed results.

Sample	Observed Pattern	Quantified result (ng/µl)	Expected Result	Observed Result From Figure 6 (loci involved)
A		0.38	Peak drop out	D16SS39, TH01, and D75820 dropped out
B	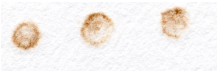	0.46	Peak drop out	D16SS39, TH01,and D75820 dropped out
C		0.84	Full profile	Full profile
D		2.34	Full profile	Full profile
E		>6	Peak pull up	Amelogenin pulled up

fully-natured state (double stranded). This has been suggested by the manufacturer and reported in the literature[25]. Either way, the results indicate that the DNA yielded from the process

cannot induce nanoparticle aggregation after the 95 ºC step. It is known that normal DNA manipulations such as pipetting or mixing can shear or nick DNA [28], for all the experiments in this chapter, extracted DNA sample were manipulated with the same vortexing duration and pipetting steps, therefore the influence of DNA manipulation on the detection limit can be ruled out. As a result, DNA quantification was always performed after the 75ºC step prior to the enzyme deactivation step (**Figure 5-9**).

Table 5-1 shows the quantitation results with enzyme-extracted DNA from the buccal swabs from five different individuals, using the nanoPAB method. **Figure 5-10** shows the standard curve from which the quantitation results were obtained. For each sample, the table shows triplicate nanoPAB pattern, these results could be used as a visual guidance (akin to

litmus-saturated paper for rapid visual estimation of pH) to provide semi-quantitative

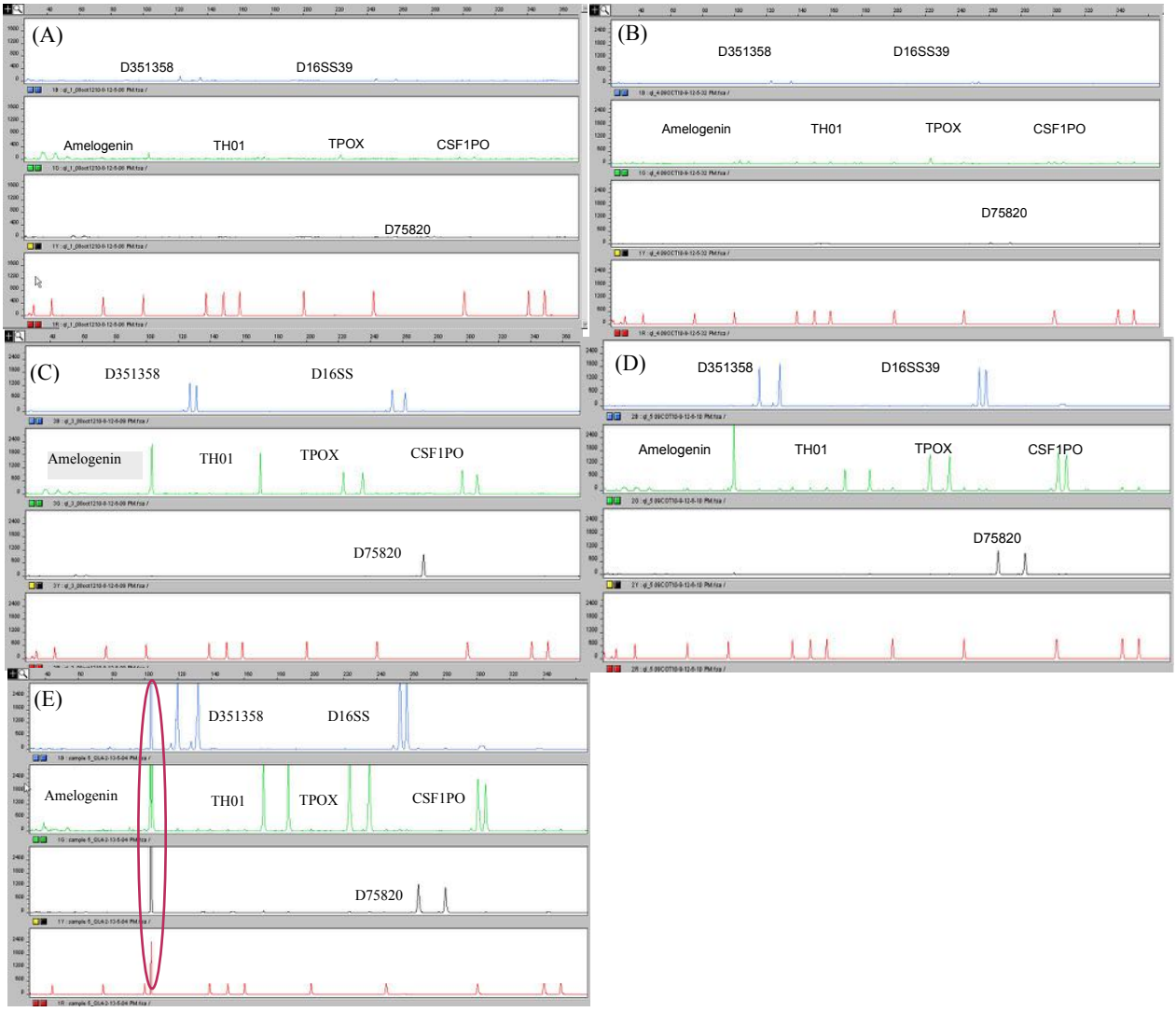

Figure 5-11*. Electropherogram of the five samples in Table 1. Sample A and B contain insufficient DNA and lead to incomplete STR profile. C and D contain the right amount of DNA and resulted in full STR profiles. Sample E comprises too much DNA and saturated the detector, causing peak pull up (circled).*

information. With the help of an algorithm, quantitative results were generated and used to predict STR results when 1 µl of the extracted DNA was loaded. Sample E's DNA content is

beyond the dynamic range of nanoparticles, i.e., nanoparticles are saturated, therefore it's semi-quantitative. The electrophoretic STR profiles resulting from these samples are given in **Figure 5-11**, as predicted in table 1, three of the five samples failed to provide acceptable profiles. With a template load of less than 0.5 ng, a loss of one of the alleles (one of a pair of loci peaks) or complete loss of peaks at the locus are seen; this is referred to as 'peak dropout' (**Figure 5-11A and 5-11B**). On the other hand, template masses above 2.5 ng can lead to the amplification of non-specific products and/or a 'bleed' of fluorescence signal into other colors; this is referred to as 'peak pull up', and generates redundant peaks that interfere with effective interpretation of the data (**Figure 5-11E**). An optimal DNA mass of 0.5-2.5 ng ensures successful amplifications (**Figure 5-11C and 5-11D**). A reliable estimate of the sample DNA concentration prior to the PCR step is critical to ensure the quality of the result data and enhancing accurate interpretation.

5.5 Concluding Remarks

In conclusion, we have synthesized superparamagnetic Fe_3O_4@SiO_2 nanoparticles, that exhibit high magnetization, large surface area and narrow monodispersity. The synthesized nanoparticles were applied to quantify DNA via a nanoparticle-DNA aggregation process, enhanced sensitivity was seen in compare with Dynabeads®. prepGEM™ prepared DNA was quantified and the results were applied to guide short tandem repeat amplification successfully. Nanoparticles could advance the development of the 'pinwheel assay' with enhanced sensitivity, as well as shed light on the mechanism that causes the aggregation.

5.6 References

1. a) Penn, S. G.; He, L.; Natan, M. Curr. Opin. Chem. Biol. 2003, 7, 609-615. b) Pankhurst, Q. A.; Connolly, J.; Jones, S. K.; Dobson, J. ***J. Phys.D: Appl. Phys***. 2003, 36, R167-R181. c) Willner, I.; Katz, E. ***Angew. Chem., Int. Ed***. 2003, 42, 4576 - 4588. d) Xu, C.; Xu, K.; Gu, H.; Zhong, X.; Guo, Z.; Zheng, R.; Zhang, X.; Xu, B. ***J. Am. Chem. Soc***. 2004, 126, 32-33. e) Perez, J. M.; O'Loughin, T.; Simeone, F. J.; Weissleder, R.; Josephson, L. ***J. Am. Chem. Soc***. 2002, 124, 2856-2857. f) ***Chem. Rev.*** 2008, 108, 2064–2110. g) ***Chem Soc Rev***. 2009, 38(9), 2532–2542. h) ***J Nanopart Res*** (2011) 13:4411–4430. i) ***Biomaterials***, 2005, 26,95–4021. j) Gupta, A. K., & Gupta, M. x ***Biomaterials,*** 2014, 26(18), 95–4021.
2. Chourpa, I., Douziech-Eyrolles, L., Ngaboni-Okassa, L., Fouquenet, J.-F., Cohen-Jonathan, S., Souce, M., Marchais, H. ***Analyst***, 2005, 130(10), 15–1403.
3. Ruiz, A., Salas, G., Calero, M., Hernández, Y., Villanueva, A., Herranz, F., Veintemillas-Verdaguer, S., et al. 2013. ***Acta Biomaterialia***, 9(5), 6421–6430.
4. Yu, X., Tong, S., Ge, M., Zuo, J., Cao, C., & Song, W. 2013. ***Journal of Materials Chemistry A,*** 1(3), 959–965.
5. Suh, S. K., Yuet, K., Hwang, D. K., Bong, K. W., Doyle, P. S., & Hatton, T. A. ***J Am Chem Soc***, 2012, 134(17), 7337–7343.
6. A. Drmota, M. Drofenik, J. Koselj and A. Žnidaršič. Microemulsion Method for Synthesis of Magnetic Oxide Nanoparticles DOI: 10.5772/36154 ISBN 978-953-51-0247-2, Published: 2012, March 16.

7. Okoli, C., Sanchez-Dominguez, M., Boutonnet, M., Järås, S., Civera, C., Solans, C., & Kuttuva, G. R. ***Langmuir***, 2012, 28(22), 8479–8485.

8. Lee, J., Lee, Y., Youn, J. K., Na, H. Bin, Yu, T., Kim, H., Lee, S.-M., et al. ***Small,*** 2008, 4(1), 143–152.

9. a) Deng, H., Li, X., Peng, Q., Wang, X., Chen, J. and Li, Y. ***Angew. Chem. Int. Ed***., 2005, 44, 2782–2785. b) Cheng, C., Wen, Y., Xu, X., & Gu, H. ***Journal of Materials Chemistry***, 2009, 19(46), 8782–8788. c) Ge, J., Hu, Y., Biasini, M., Beyermann, Ward P. and Yin, Y. ***Angew. Chem***. ***Int. Ed***., 2007, 46, 4342–4345. d) Si, S., Li, C., Wang, X., Yu, D., Peng, Q., & Li, Y. Crystal Growth & Design, 2005, 5(2), 1–3. e) X. Wang, J. Zhuang, Q. Peng and Y. D. Li, ***Nature***, 2005, 437, 121-124. f) Jia, X., Chen, D., Jiao, X., & Zhai, S, ***Chemical Communications***, 2009, 0(8), 968–970. g) Wang, J., Yao, M., Xu, G., Cui, P., & Zhao, J, ***Materials Chemistry and Physics***, 2009, 113(1), 6–9.

10. Beaven GH, Holiday ER, Johnson EA: In The Nucleic Acids. Volume 1. Edited by Chargaff and Davidson JN. Academic Press, New York; 1955

11. Ahn SJ, Costa J, Emanuel JR, ***Nucleic Acids Res***, 1996, 24(13), 2623–2625.

12. Sanchez JL, Storch GA, ***J Clin Microbiol,*** 2002, 40, 2381-2386.

13.Leslie, D. C., Li, J., Strachan, B. C., Begley, M. R., Finkler, D., Bazydlo, L. A., Landers, J. P, ***J Am Chem Soc***, 2012, 134(12), 5689–5696.

14. Li, J., Liu, Q., Alsamarri, H., Lounsbury, J. A., Haversitick, D. M., & Landers, J. P, ***Lab Chip***, 2013, 13(5), 955–961.

15. Melzak, K. A., Sherwood, C. S., Turner, R. F. B., & Haynes, C. A, ***J Colloid Interface Sci***, 1996, 181(2), 635–644.

16. Richmond, R. K., Sargent, D. F., Richmond, T. J., Luger, K., & Ma, A. W, ***Nature.*** 1997, 389, 251-260.

17. Brunauer, S., Emmett, P. H., & Teller, E, ***J Am Chem Soc***, 1938, 60(2), 309–319.

18. Dodson, M. H., and E. McClelland-Brown, ***J. Geophys. Res.***, 1980, 85(B5), 2625–2637.

19. Rivetti, C., & Codeluppi, S, ***Ultramicroscopy,*** 2001, 87(1-2), 55–66.

20. Masters, J. R., Thomson, J. a, Daly-Burns, B., Reid, Y. a, Dirks, W. G., Packer, P., Debenham, P. G., ***Proc. Natl. Acad. Sci***, 2001, 98(14) 8012-8017.

21. Liu, J., Sun, Z., Deng, Y., Zou, Y., Li, C., Guo, X., Xiong, L., et al., ***Angewandte Chemie*** (International ed. in English), 2009, 48(32), 5875–9.

22. Deng, Y., Qi, D., Deng, C., Zhang, X., & Zhao, D., ***J Am Chem Soc***, 2008, 130(1), 28–29.

23. Andersen, J. Methods in molecular biology (Clifton, N.J.), 1998, 98(3), 33–38.

24. a)Wolfe, K. A., Breadmore, M. C., Ferrance, J. P., Power, M. E., Conroy, J. F., Norris, P. M., & Landers, J. P., ***ELECTROPHORESIS***, 2002, 23(5), 727–733. b) Breadmore, M. C., Wolfe, K. A., Arcibal, I. G., Leung, W. K., Dickson, D., Giordano, B. C., Landers, J. P, ***Analytical Chemistry***, 2003, 75(8), 1880–1886.

25. a) Lounsbury, J. a, Coult, N., Miranian, D. C., Cronk, S. M., Haverstick, D. M., Kinnon, P., Landers, J. P., ***Forensic science international. Genetics***, 2012, 6(5), 607–615. b) Quick start guide – DNA extraction using prepGEMTM saliva, Available at: http:// www.zygem.com/images/pdf/prepGEM_Saliva_WQSG.pdf

26. Edward M. Golenberg, Ann Bickel and Paul Weihs. ***Nucl. Acids Res.*** 1996, 24 (24), 5026-5033.

27. a) Ginoza, W., and Zimm, B. Proc. Natl. Acad. Sci. 1961, 41, 6-652 b) Lindahl, T., & Nyberg, B. ***Biochemistry***, 1974, 13(16), 3405–3410.

28. Protection of megabase DNA from shearing. ***Nucl. Acids Res.*** (1995) 23 (19): 3999-4000

29. Parida, S. K., Dash, S., Patel, S., & Mishra, B. K. (2006). Adsorption of organic molecules on silica surface. ***Advances in Colloid and Interface Science***, 121(1-3), 77–110.

30. Melzak, K. A., Sherwood, C. S., Turner, R. F. B., & Haynes, C. A. (1996). Driving forces for DNA adsorption to silica in perchlorate solutions. ***J Colloid Interface Sci***, 181(2), 635–644.

Chapter 6 Summary and Future Directions

6.1 Summary

The "pinwheel assay", a novel, cost-effective, and simple DNA quantitation assay, has found a variety of applications in the clinical and forensic world. The work presented in this dissertation described efforts towards the development of point-of-care devices for clinical and forensic application.

In Chapter 2, we extended the pinwheel assay from nucleic acid quantification to cell counting. Cell counting using the pinwheel assay relies on quantitation of the DNA content incells and that each cell contains a certain amount of DNA. A specific subtype of cells, - CD4+ T cells, was studied because of it's importance in HIV prognosis and progression analysis. Coupled with immunomagnetic separation, the pinwheel assay results showed excellent correlation with the flow cytometry (R^2 =0.997), which indicates the pinwheel assay could serve as a portable and cost-effective alternative to conventional technologies for point-of-care applications.

Chapter 3 is the continuation of Chapter 2, where each step (cell isolation, lysing, metering, DNA quantitation) was manually performed in tubes. In chapter 3, an integrated microfluidic system was developed. In this device, the PDMS surface was treated with air plasma to create a super-hydrophilic surface, and geometrical capillary valving was utilized for volumetric measurement. The correlation with the flow cytometry, was still good (R^2=0.98). Although still a prototype, this device is one step closer to a real world point-of-care device.

In Chapter 4, we presented a simple, portable, and label-free paper fluidic assay for fast DNA quantification, which presented many advantages: 1) Optical quantification of DNA in minutes, 2) Minimal, inexpensive instrumentation – no lasers, no fluorescence, 3) Automated quantification with custom made algorithms, and 4) Footprint reduction feasible for handheld device. Moreover, this assay can be further integrated with paper-based DNA extraction methods and microfluidic PCR for sample-to-result genetic analysis at the point -of-care.

In Chapter 5, we touched on the mechanism of the "pinwheel assay". Superparamagnetic Fe_3O_4@SiO_2 nanoparticles were synthesized via the solvothermal method.The nanoparticles exhibit high magnetization, large surface area and narrow monodispersity. The synthesized nanoparticles were applied to quantitate degraded human genomic DNA via the pinwheel assay and the nanoPAB assay was successfully applied to guide the STR analysis.

6.2 Future Directions

6.2.1 A Commercialized CD4+ T-cells Counting Device

As mentioned at the end of **Chapter 3**, in order to introduce the CD4 counting device to the market, we need to be able to pre-package the device and ship it as is. Therefore, the plasma treatment needs to be eliminated. The solution lies in finding a super hydrophilic coating that works on PDMS. The preliminary trial using the Lotus Leaf Hydrophil® was not successful. However, it's worthwhile to examine other commercially available coating products where an ideal coating would be able to maintain hydrophilicity over time.

Figure 6-1 presents a proposed device that integrates a cell phone for image capture and algorithm analysis, an android app that processes dark area has been developed. The pedestal

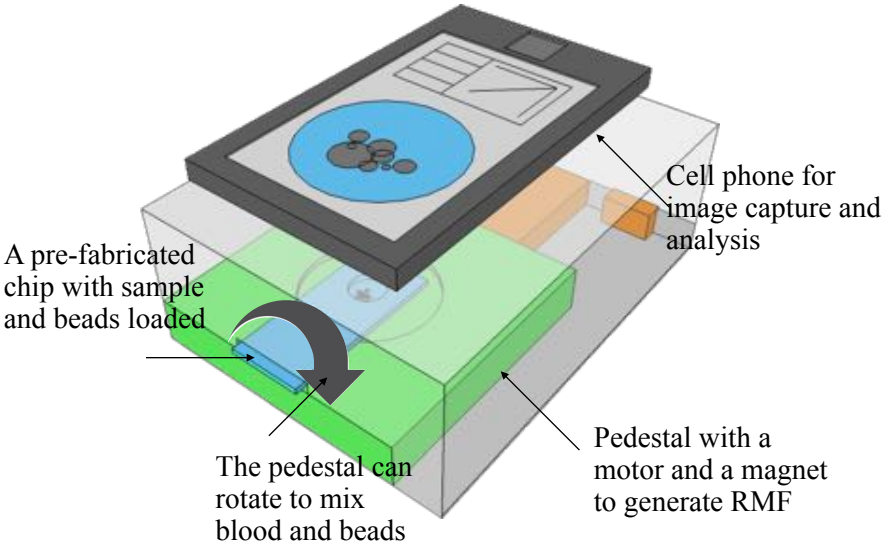

***Figure 6-1**. Design of the point of care CD4+ T-cells counting shoebox.*

contains two different motors, where one is used to generate the RMF in the quantitation step and the other is used to rotate the chip to mix the blood samples and antibody coated beads in the cell isolation step.

6.2.2 Compact Disc-like Centrifugal Microfluidic Platforms for CD4+ T-Cells Counting

A centrifugal polyester-toner disc was recently developed in our lab [1]. The device is made of 5 layers of transparencies, where layers 1,3,5 are bare and layers 2 and 4 are transparencies with toner printed on both sides. These 5 layers are assembled by lamination. This device has the advantages of rapid processing, easy automation, as well as low cost and simple fabrication. Toner patches were printed on the transparency and used as hydrophobic valves [2], allowing metering to be defined by the overflow method. Volumetric measurement and the pinwheel assay have already been successfully integrated on this type of microfluidic platform, meaning CD4+ T-cells counting can be achieved by simply adding one more domain to the device.

The preliminary design is shown in **Figure 6-2.** Each chip can process 5 samples simultaneously. Fluidic processing steps such as mixing of sample and beads, or metering of sample fluids, can be automated simply by implementing different spin profiles. The CD4+ T-cells isolation, mixing and volumetric measurements are driven by centrifugal and capillary forces on the disc. The CD4+ T-cells isolation procedure needs to be optimized on the device, as detailed in **Chapter 3**, according to the dynamic range of the pinwheel assay. The isolation chamber is deigned to be ~100 µl which is challenging due to the dimension limitations of the polyester-toner chip. We can reduce the blood input from 10 µl to 1-2 µl, thus reducing the

chamber volume to 10-20 µl or another dilution step could be added to dilute the cell lysate ~10x so that the final DNA concentration falls within the pinwheel assay dynamic range.

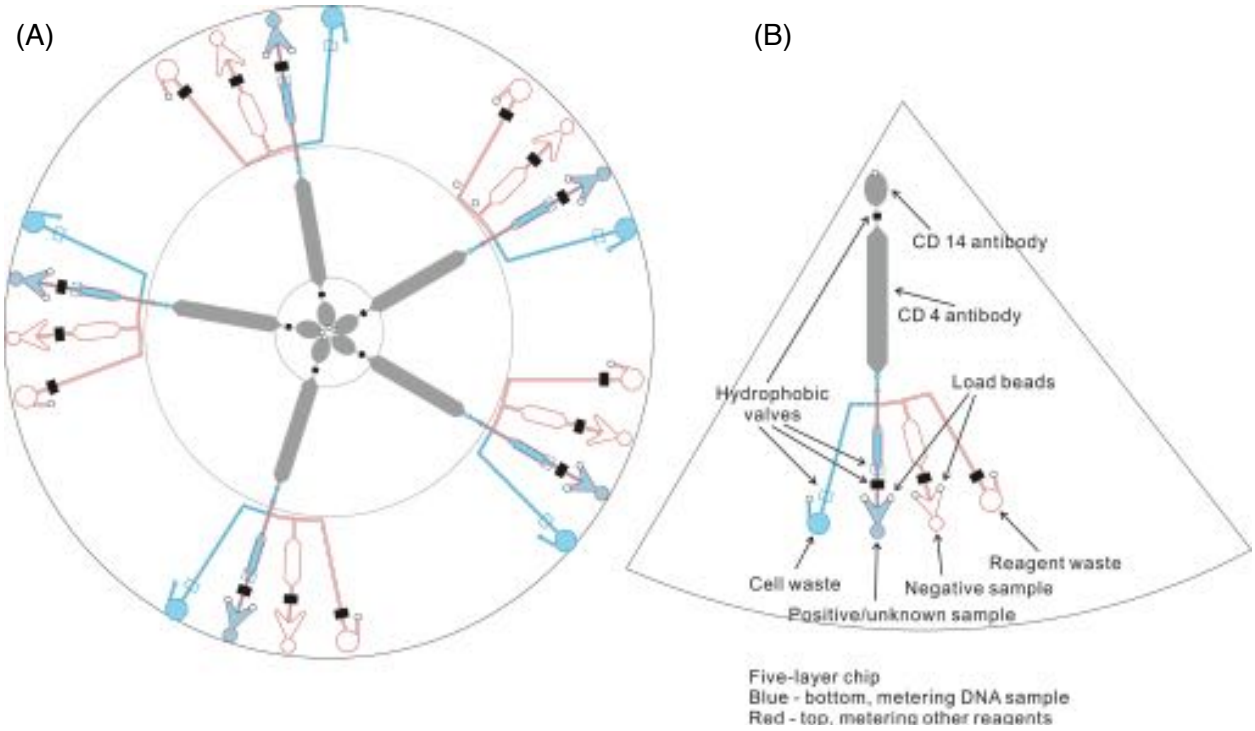

Figure 6-2. *Design of the CD4+ T-cells counting disk. (A) One disc can process up to 5 samples simultaneously. (B) Each sample domain comprises a CD14 monocytes depletion chamber, a CD4 chamber, the metering/mixing domain, and the pinwheel domain.*

6.2.3 Integrate CD4% and HIV Viral Load Measurements

Besides the absolute CD4 count, several other factors, such as the CD4% (the percentage of white blood cells that are CD4 T-cells), and HIV viral load (the amount of HIV in 1 µl blood), can also be monitored over time to observe trends. For example, children under the age of 12 are

monitored solely by their CD4% because they are born with very high CD4 counts. The HIV viral load test can also be useful in diagnosing babies born from HIV positive mothers.

CD4% is sometimes a more stable indication of whether there has been a change in the immune system. Any drop in the CD4 count when the percentage hasn't changed indicates the drop is not clinically significant. In general, 1) a CD4% of 12-15% is about the same as a count of less than 200 cells/µl, the threshold for AIDS, 2) a CD4% of 29% is about the same as a count of greater than 500 cells/µl, the threshold for ART (there is a wider range for higher values), 3) an HIV-negative person has a CD4 percentage of about 40% [3].

A high viral load in the blood implies the immune system is not strong enough to fight the virus [4], the viral load test directly provides information on the patient's health status and how well ART is working. When the viral load is less than 40 copies/µl blood, the virus is claimed "undetectable" [4]. The HIV viral load is measured 1) right after diagnosis, which gives a reference for future tests (baseline measurement), 2) every two to eight weeks at the start of ART or with a change in treatment, to evaluate how well the medication is working, 3) Every three to six months or as the doctor directs if the treatment is effective.

The device could be functionally upgraded to allow CD4 percentage and possibly HIV viral load measurements to be analyzed simultaneously on the same instrument. To get the CD4%, we can add a WBC count domain on the device. When the blood samples are introduced, half of the sample will go to the WBC domain for overall lymphocytes counting, and the CD4% can be calculated as the ratio of the CD4 count over the WBC count.

The viral load will be more challenging to integrate on the device. Viral load is tested from plasma, therefore a separation step is required, however, separation of plasma from whole

blood has already been achieved on the polyester toner centrifugal device in our lab [5]. Specific kits such as TRIZOL, LS reagent (Invitrogen, Karlsruhe, Germany), QIAamp Viral RNA kit (Qiagen) and High Pure Viral RNA Kit (Boehringer Mannheim) are available to extract HIV RNA from plasma [6], followed by one of three different types of tests, 1) Reverse-transcriptase polymerase chain reaction (RT-PCR) test, 2) Branched DNA (bDNA) test, 3) Nucleic acid sequence-based amplification (NASBA) test. Each of these tests reports the results differently. RT-PCR allows the determination of viral serum concentration over a wide scale, by using the Reverse Transcriptase (RT) enzyme to convert viral RNA into complementary DNA (cDNA). The cDNA then undergoes replication and quantitative detection. There are four commercially available RT−PCR based viral load assays: 1) Amplicor HIV−1 Monitor v1.5 (Roche Molecular Systems), 2) COBAS AmpliPrep/ COBAS TaqMan v2.0 (Roche Molecular Systems), 3) RealTime HIV−1 (Abbott), and 4) VERSANT HIV−1 RNA 1.0 assay (kPCR) [7]. RT-PCR has never been performed on the polyester toner device and normal PCR amplification on the same devices have seen challenges, including low efficiency and poor reproducibility. Sophisticated engineering and biochemistry studies are required to integrate the viral load test on the device. Although challenging, the device would be powerful if it offers the possibility to perform a complete monitoring program (CD4 T-cell count, CD4% and viral load) .

6.3 References

1. Ouyang, Y., Li, J., & Landers, J. P. Integration of Pinwheel Assay on a Cd-Like Microchip for Dna Quantitation, (October), 2013,1613–1615.
2. Ouyang, Yiwen *et al.* Rapid patterning of 'tunable' hydrophobic valves on disposable microchips by laser printer lithography. ***Lab Chip***. 2013;13(9):1762-71.
3. Yu, L. M., Easterbrook, P. J., & Marshall, T. Relationship between CD4 count and CD4% in HIV-infected people. ***International Journal of Epidemiology***, 1997, 26(6), 1367–1372.
4. Adults, H.--infected. (n.d.). Guidelines for the use of antiretroviral agents in HIV-infected adults and adolescents. ***HIV Clinical Trials***, 2001. 2(3), 227–306.
5. Brandon L Thompson *et al.* Protein and Hematocrit Quantitation from Whole Blood on Polyester-Toner Laser-Printed Microfluidic Discs with Cell Phone Image Analysis. ***PITTCON proceedings***. 2015, March 11th,1800-7.
6. Fransen K *et al.* Isolation of HIV-1 RNA from plasma: evaluation of seven different methods for extraction. ***J Virol Methods***.1998 Dec;76(1-2):153-7.
7. Viral, F. Technical Brief on HIV Viral Load Technologies, 2010, June, 1–44.